Image Analysis for the Assessment of Pathologies in Retinal Tissue

BY

FATIMAH MOHAMMAD
B.C.S International Islamic University, Islamabad Pakistan, 2004
M.S. C.S International Islamic University, Islamabad Pakistan, 2006

THESIS

Submitted in partial fulfillment of the requirements
for the degree of Doctor of Philosophy in Electrical and Computer Engineering
in the Graduate College of the
University of Illinois at Chicago, 2013

Chicago, Illinois

Defense Committee:

Rashid Ansari, Chair and Advisor
Jezekiel Ben-Arie
Ashfaq Khokhar
Milos Zefran
Mahnaz Shahidi, Department of Ophthalmology and Visual Sciences, UIC

To my best buddy, Inam Ahmed Shaikh, who effortlessly makes me smile each day.

To my mother Halima Mohammad. This silly little dedication can never repay you for all that you have done and still do for me. You are the best.

ACKNOWLEDGMENTS

When I first joined the PhD program at the University of Illinois at Chicago back in 2007, I could not fathom what it would feel like to successfully defend my thesis so many years later. I have been so lucky to be accepted into such a prestigious university as UIC. I have many fond memories of my time here and especially with the friends I made when I was living in SSR. It was such an adventure moving from Pakistan to the beautiful city of Chicago, and I know that no matter where I am my heart will always have a special place for the Windy City. So it is with a sense of bittersweet accomplishment that I sit today to type up my Acknowledgements and add the final touches to my thesis just hours before my final submission.

I think all PhD graduate students go through the same highs and lows when they are working on their research. But having a good advisor is probably the only thing that can actually make you come out stronger when you feel you have hit a wall and you don't know which direction to turn.

I have been extremely fortunate with my advisors, Dr. Rashid Ansari, my primary advisor, and Dr. Mahnaz Shahidi, my secondary advisor. Dr. Rashid Ansari is one of the nicest professors I know. Every time I would leave his office after a lengthy meeting I would think to myself, "I hope I can be as good an advisor as he is one day." His thoroughness and attention to detail always inspired me. From our talks and discussions I learned many things other than about my research that I will remember for years to come. With him I never felt that I was "just another student," because he always treated me more like a daughter. Nothing I write

here can come close to expressing the gratitude I have for the time and effort he expended on me the last six years. He is extremely kind and considerate, and he does what it takes to make his students come out shining on top no matter how far behind they were when they started. I would say to all students who are lucky enough to have him as their advisor that they could not be in better hands.

I would like to thank Dr. Mahnaz Shahidi, who was always there to keep me on my toes. If not for her keeping me on track I would probably be stuck in a dead-end idea. She is professional, yet she is also very understanding and she knew how to keep me motivated by telling me exactly what I needed to hear to stay focused and to not lose sight of what my aims were. I enjoyed being a member of the Applied Physics lab, I made many friends with whom I hope to continue to keep in touch with.

I would like to thank my committee members, Dr. Jezekiel Ben-Arie, Dr. Ashfaq Khokhar, and Dr. Milos Zefran for taking the time to review my thesis and for providing invaluable feedback.

I would like to thank my dear friend Habiba, who was always there to answer my frantic emails or phone calls about the challenges I was running into with my research. Being a PhD graduate of UIC herself, she is probably the only one who could truly understand my feelings of despair. In her usual calm way she would always give me good advice on how to pull through the difficulties and luckily things always worked out better than I expected. Knowing that we both were in the same boat really helped get us through the tough times together!

ACKNOWLEDGMENTS (Continued)

I would like to thank Faiza, Naheed, and Sana, my best friends with whom I probably shared the best times of my life before coming to UIC. They were my sounding boards for whatever ideas I had, they were my best and worst critics, and they were always there to make me laugh through whatever crisis I felt I was going through, be it personal or professional.

I would like to thank my brothers and sisters who always motivated and supported me during my time at UIC. Specifically, I would like to thank my brother Saeed. He may not remember it, but six years ago he encouraged me to apply for a PhD in the US and without his help I could not have made it through the application processes, let alone reach defense day.

I would like to thank my dear husband, Inam, who was always there to make me laugh. His calmness, kindness, and tolerance helped me to finish my thesis in great spirits. Along with the many tiring hours I spent in front of my computer typing up my thesis, I had many fun hours in front of the same computer watching countless episodes of Star Trek with him. He has contributed as much to this thesis as I have just by being by my side.

Finally, I would like to thank my mother, who always encouraged me to to work hard, to be independent, and to look for happiness within myself. I wish I listened to you more often, Mom!

F.M.

TABLE OF CONTENTS

TABLE OF CONTENTS (Continued)

CHAPTER **PAGE**

LIST OF TABLES

LIST OF FIGURES

LIST OF FIGURES (Continued)

LIST OF FIGURES (Continued)

FIGURE **PAGE**

LIST OF ABBREVIATIONS

AMD	Age-related macular degeneration
DR	Diabetic retinopathy
DC	Direct current
AO	Adaptive optics
OCT	Optical coherence tomography
OCT	Spectral-domain optical coherence tomography
FD	Fourier descriptors
DFT	Discrete Fourier transform
DSFT	Discrete space Fourier transform
1D	One-dimensional
ISOS	Inner-segment/outer-segment
RPE	Retinal pigment epithelium
NFL	Nerve fiber layer
IPL	Inner plexiform layer
OPL	Outer plexiform layer
INL	Inner nuclear layer
ONL	Outer nuclear layer

LIST OF ABBREVIATIONS (Continued)

2D	Two-dimensional
3D	Three-dimensional
CAF	Content-adaptive filtering
L-CAF	Local content-adaptive filtering
CCD	Charged coupled device
MEMS	Micro-electromechanical system
DM	Deformable mirror
SRF	Sub-retinal fluid
VEGF	Vascular endothelial growth factor
CNV	Choroidal neovascularization
CST	Central subfield thickness
VA	Visual acuity
SLO	Scanning laser ophthalmoscope
ROI	Region of interest
IR	Infrared
PED	Pigment epithelium detachment
MR	Magnetic resonance
UIC	University of Illinois at Chicago

SUMMARY

Photoreceptor cell degeneration due to disease may lead to loss of visual acuity. With the recent availability of adaptive optics (AO) and spectral domain optical coherence tomography (SD-OCT) imaging systems, it is now possible to image the retina at the cellular level. Many of the challenges involved with retinal image analysis are due to the low contrast and system noise observable in the images. Photoreceptor cell regularity and the integrity of the photoreceptor segment junction layer are studied as the photoreceptor cells play a fundamental role in human vision. The goal of this research is to develop automated methods which can provide qualitative and quantitative metrics that aim to describe the state of healthy or diseased retinas. We present a novel framework which can potentially link the observations made in AO retinal images with those made in SD-OCT en face retinal images. In our preliminary work, we focus on photoreceptor cell regularity estimation by the quantification of cells in AO retinal images of the human eye. The issues addressed include low contrast images as well as varying cellular packing arrangement within a single image. We initially developed a content-adaptive filtering method which analyzes image frequency content in the spatial domain using intensity profiles of the image to identify photoreceptor cells. To account for false positive detection due to noise, we describe an image model in the frequency domain using a windowed, two-dimensional (2D) lattice of pulses which represent the cells and characterize the frequency content as decaying frequency domain pulses on the reciprocal lattice. This model uses a small-extent, block-based, 2D Discrete Fourier transform (DFT) to obtain the parameters of

an adaptive, circularly-symmetric band-pass filter that is applied to the image to extract the underlying cellular structure and remove high and low frequency contamination. Our automated results of cell detection compared well with manual results on computer-generated test and retinal images. There is a strong association between the integrity of the ISOS layer and the photoreceptor health. We therefore developed a method for pathology segmentation in fluorescein angiograms as test images, and en face retinal images of the ISOS layer of patients with age-related macular degeneration and diabetic retinopathy. We develop a level-set method based on the classical Chan-Vese model and exploit *a priori* knowledge of the shape and intensity distribution, allowing the use of projection profiles to detect the presence of pathologies. Our method provides improved speed and reliability in the segmentation which may fail in classical algorithms with an incorrect choice of initial contour.

It was of interest to analyze all retinal cell layers in an en face manner, to investigate if pathologies in an overlying retinal layer could cause artifacts or shadows to appear on the ISOS layer. In this case, the pathology that appears to be on the ISOS layer would be due to optical factors. If however the pathology on the ISOS layer is unrelated to overlying pathology, it would be indicative of neural dysfunction. We develop a level-set method that incorporates shape priors, defined by Fourier descriptors, to guide the evolution of the curve towards objects matching a target shape. We apply our method to en face images representing seven layers of the retina. The level-set function is defined such that it evolves across the layers and adapts to the pathologies present in the image. In order to determine the origin of pathology, we measure the co-localization across overlapping layers. We show how our method overcomes the

common problems encountered by other proposed level-set models by comparing our method to a well-known distance-regularized method which does not use shape priors. The comparison clearly shows how use of our method is more effective due to the incorporation of Fourier-based shape priors.

CHAPTER 1

INTRODUCTION

1.1 Overview and motivation

Photoreceptor cells are light-sensitive cells which convert light energy into electrical signals. These electrical signals are interpreted by the brain enabling us to "see." Various retinal diseases, such as age-related macular degeneration (AMD) and diabetic retinopathy (DR), cause photoreceptor cell degeneration in the retina and may lead to severe loss of visual acuity. The photoreceptor cells are located on the inner segment outer segment (ISOS) junction layer. Disruption of this layer is an important predictor of visual acuity in patients with diseased eyes. Death of the photoreceptor cells leads to the death of the ISOS layer in the retina, resulting in vision loss [5, 10–15].

The goal of this research is to develop automated methods which can provide qualitative and quantitative metrics that aim to describe the state of healthy or diseased retinas. The motivation behind our work is that common and widespread retinal diseases are the principal causes of blindness. Tools need to be developed which provide accurate results of large data-sets in a timely manner [16, 17].

1.2 Summary of contributions

Automated photoreceptor cell density estimation in high-resolution retinal images generated by adaptive optics (AO) imaging systems is important due to its potential for screening and

diagnosis of diseases that affect human vision. A drawback in recently reported photoreceptor cell density estimation methods is that these methods require user input of cell structure parameters [4, 5, 18–22]. This dissertation introduces a method that overcomes this shortcoming by using content-adaptive filtering (CAF)[23]. In this method, the image frequency content is initially analyzed using intensity profiles in the spatial domain to design a customized filter with a passband. This filter is applied locally in blocks to emphasize cell structures suitable for subsequent processing. As retinal cells are circular in nature and have no preferred orientation, the McClellan transform is ideal to design the circularly symmetric bandpass filter. The automated filter design eliminates the need for manual determination of cell structure parameters, such as cell spacing. Following the preprocessing step, the image is binarized and the cell density is estimated from the binarized image. Photoreceptor cell estimates using this automated procedure are found to be comparable to manual estimates (gold standard). The new method when applied to test images as well as to actual retinal images with variable cell spacing shows overall improved performance when compared with previously reported methods requiring user-supplied input.

A potential drawback of measuring photoreceptor density in the spatial domain is that the intensity profiles can be greatly affected by the presence of noise. Peaks in the profile, which may be representative of noise, may be incorrectly identified as cells. In order to overcome this possible limitation, we analyze the cone mosaic in the frequency domain. We describe an image model using a windowed two-dimensional (2-D) lattice of pulses which represents the cells and characterizes the frequency content as decaying frequency domain pulses on the reciprocal

lattice [24]. Based on this, we propose a novel method for detection of cone photoreceptor cells by analyzing the discrete-space Fourier transform (DSFT) of AO retinal images. This method uses a small-extent, block-based, 2D Discrete Fourier transform (DFT) to determine cell frequency content in order to obtain the parameters for an adaptive, circularly symmetric band-pass filter that is applied to the image. The filter extracts the underlying cellular structure and removes high-frequency noise as well as very low frequency contamination manifested as slow intensity variations in the image. We test the robustness of our method by applying it to images corrupted by noise as well as to images which have been artificially manipulated so that cell structure appears different. Subsequent detection yields an automated cell estimate that compares well with actual and manual estimates on test and retinal images and demonstrates the accuracy of the method.

Retinal degeneration due to disease ultimately results in the death of the photoreceptors and leads to the death of the inner and outer segment layers in the retina [5, 11–15]. It is therefore desirable to develop automated segmentation techniques to identify lesions in retinal images in order to reduce the inter-observer variability as well as the manual segmentation effort and time. We investigate the segmentation of pathologies in fluorescein angiograms and en face retinal images in patients with AMD and DR by building upon the level-set method based on the classical Chan-Vese model [25]. Image acquisition is performed during different patient visits to observe the changes in pathology over time as a result of treatment. We explore an improved method for pathology segmentation in retinal images which automatically isolates the pathology for contour placement as opposed to manually specifying the location of the

initial contour randomly. This is accomplished by exploiting *a priori* knowledge of the shape and intensity distribution of the pathology which allows the use of projection profiles to detect the presence of lesions characterized by abrupt intensity differences with surrounding areas in retinal images. The method is shown to provide improved reliability in the segmentation which may fail in classical algorithms with a random choice of the initial contour. As the initial contour encloses the region of interest on the first iteration, a segmentation result is obtained with reduced number of iterations and the speed of convergence is improved. The results of this study indicate a strong relationship between the integrity of the ISOS junction layer and visual acuity. Pathologic regions observed in the ISOS en face image indicate areas of cell death, which appear as dark patches in AO retinal images.

We extend our research by including in our analysis the en face images of seven layers of the retina. A wealth of information is available upon examining the cell layers in conjunction with one another and by observing how the pathologies flow from one layer to the next. Analysis of the ISOS layer individually is insufficient to conclude the origins of the disease and the extent to which the disease has progressed. By including multiple layers in our study, we are able to provide insight as to how abnormalities in the upper layer of the retina are represented in the ISOS layer. The level-set approach is used for a preliminary analysis and this approach proves useful when segmenting pathologies across multiple layers. We develop a level-set model that uses Fourier descriptor based shape priors to specify a target shape. During the application of our method, the final level-set function obtained for a given image is used as the initial level-set function for the image in the subsequent layer. In this way, the segmentation appears to

flow across the images and the problem of specifying an initial contour is seamlessly handled, as pathologies tend to be grouped in the same region. Use of Fourier descriptors allows for the definition of target shapes which are invariant to rotation, scale, and translation. Metrics, such as the area of the pathologies and their centroids, are obtained and are used to determine whether the pathologies visible on the ISOS layer are neural or optical in nature. Neural pathologies occur directly on the ISOS layer and indicate photoreceptor disruption. Areas in the retina where the integrity of the ISOS layer has been compromised would appear as black patches on the corresponding AO image, indicating regions of photoreceptor cell death. In the case of optical pathologies, abnormalities appear in the inner retinal layers, and cause optical effects such as shadowing on the ISOS layer. Given the proper treatment, these abnormalities in the inner retinal layers can be removed, thus restoring the high reflectivity and integrity of the ISOS layer. By understanding how disease affects the layers of the retina, correlations can be constructed between the integrity of the ISOS layer and photoreceptor density, as studies have shown that a loss of the photoreceptor mosaic in the AO images are comparable with the area of the ISOS disturbance in OCT images [26].

1.3 Organization of dissertation content

This dissertation is divided into 7 chapters. In chapter 2, background information on the retina and retinal imaging systems including previous work done is given. In Chapter 3, we discuss the photoreceptor cell density estimation methods in adaptive optics images. Chapter 4 outlines our work on frequency domain analysis of the cone mosaic in AO images. Chapter 5 discusses our work on a level-set model for segmenting pathologies in en face retinal images.

In Chapter 6 we share some discoveries made by measuring features of pathologies in patients with neo-vascular AMD. We close with a discussion and conclusions in Chapter 7.

CHAPTER 2

BACKGROUND ON RETINAL IMAGING SYSTEMS AND IMAGE ANALYSIS TECHNIQUES

2.1 The human retina

The retina is the light sensitive tissue of the eye and it is made up of stacks of several neuron layers, which scatter light weakly. The function of the retina is to convert the light incident on it into electrical signals which are consequently transmitted to the brain. Approximately 80% of sensory information in humans is considered to be of retinal origin. This is a small indication of the importance of retinal function in human interactions with the outside world. There are up to ten layers of the retina, and each layer is highly complex and specialized in order to meet the requirements of the different regions of the retina [3, 22, 27]. Figure 2.1 shows the arrangement of nine layers of the retina.

The general histological organization of the eye consists of the following major layers: retinal pigment epithelium (RPE), inner-segment/ outer-segment (ISOS) junction layer, external limiting membrane (ELM), outer nuclear layer (ONL), outer plexiform layer (OPL), inner nuclear layer (INL), inner plexiform layer (IPL), and nerve fiber layer (NFL). In each eye, the retinal pigment epithelium (RPE) layer contains about 3.5 million RPE cells, which create a barrier between the outer retina and its blood supply. This barrier helps to control the extracellular environment and maintain the function of the outer retina. It also helps in reducing

backscattering of light which enters the eye. The ISOS layer, also known as the photoreceptor layer, contains the rod and cone cells which are tightly packed together into a single layer of photoreceptor cells. These cells consist of an inner segment (mitochondria) and an outer segment (photopigment). The outer nuclear layer (ONL) contains the nuclei of the photoreceptor cells. In the outer plexiform layer (OPL), important initial processing steps occur in the retina: photoreceptor cells of the ONL form connections with cells of the inner nuclear layer (INL) such that signals can be transmitted across layers. The INL is home to the nuclei of multiple types of cells. The inner plexiform layer (IPL) is the second retinal processing layer that consists of connections amongst several different types of cells. The nerve fiber layer (NFL) consists of expansions of fibers of the optic nerve, which transmits visual information from the retina to the brain [3, 28].

The sensors of the visual system are the rod and cone photoreceptor cells [3]. A typical cone photoreceptor cell appears in an image with high intensity in the center and this intensity gradually reduces as the distance from the center of the cell increases, much like a point-spread function. The human cones are packed most tightly in the foveal center, with the number of cones in a healthy retina averaging 4.6 million, and the packing density rapidly decreases with increasing eccentricity of the eye [29, 30].

The ISOS junction is one of the layers of the retina which specifically represents photoreceptor cell integrity. Degenerative and systemic diseases, such as age-related macular degeneration (AMD) and diabetes can alter the cellular structure of the retina, thereby causing altered visual function [31, 32]. Several studies have shown that given a diverse set of retinal pathologic

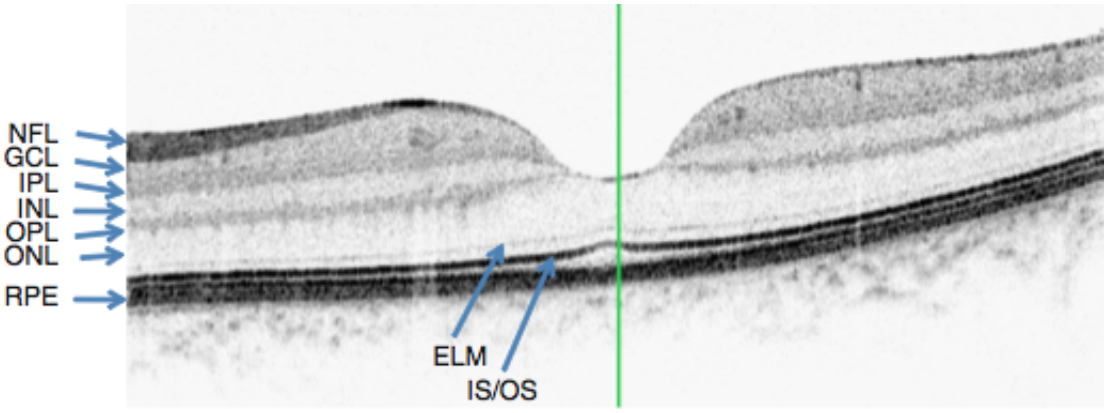

Figure 2.1. Structural detail of retinal layers [3].

conditions, a disturbance of the photoreceptor cells correlates with poor visual outcome. The wellness of the ISOS layer has therefore been identified as a fundamental component in influencing visual acuity in eyes. Dystrophy of this layer has been observed in eyes with conditions such as retinal detachment, macular hole, and AMD [10, 31]. The high resolution imaging provided by advances in adaptive optics (AO) technology allows for direct observation of individual cone photoreceptors as well as for the visualization and description of retinal substructures in the living human retina [21, 33–39]. The integrity of the photoreceptor layer can also be evaluated by examining the ISOS junction using spectral domain optical coherence tomography (SD-OCT) [10].

2.2 Adaptive optics for retinal imaging

The human eye functions primarily as a lens and contains many optical defects, regardless of whether it is a healthy eye or not. These imperfections stem primarily from the blurring

caused by aberrations in the retina and limit the resolution at which the retina can be imaged, thus making direct observation of individual cells on the retina infeasible. With the help of adaptive optics (AO) however, the aberrations can be compensated for in real-time and thus lead to appreciably sharper images [7, 27, 40–47]. The high resolution provided by advances in AO technology enables us to clearly obtain the structure and distribution of the retina at the cellular level. It allows for direct observation of individual cone photoreceptors in the living human retina which, along with other cellular structures, can be imaged due to their high reflectance and contrast [21, 48–52]. In healthy eyes, the photoreceptors reflect incident light from the ISOS junction and bright spots in the AO image represent a dominant reflection from an individual photoreceptor cell [53]. The two main components to an AO system are: a) a wave-front sensor for shape detection of the wave-front of the optical system of the eye and b) a correcting component that compensates for the wave-front aberrations. The aberrations can be corrected for once the wave-front has been measured, thereby providing superior resolution and contrast in retinal imaging. Correction is most commonly done by a deformable mirror which consists of a flexible reflective layer which is supported by an array of actuators that deform the mirror to the necessary shape in order to correct the wave-front aberration [54–57]. Figure 2.2 shows an example of the photoreceptor cone mosaic before correction (left), and after correction (right).

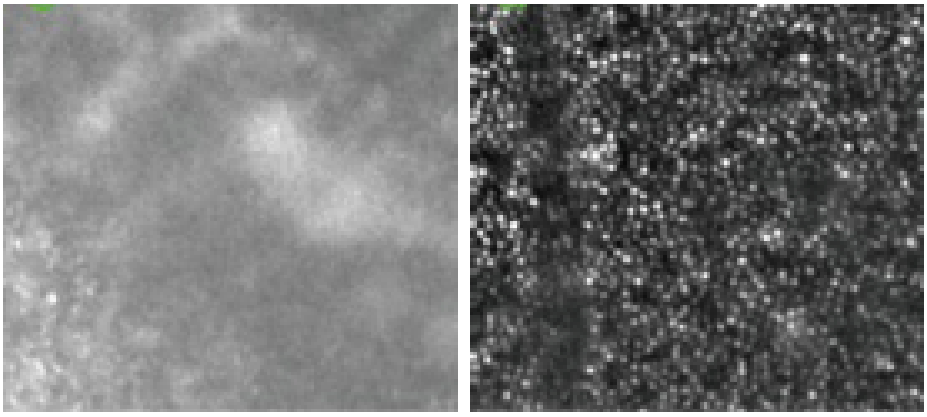

Figure 2.2. Photoreceptor images without AO correction (left) and with AO correction (right).

2.3 Spectral domain optical coherence tomography (SD-OCT) for en face retinal imaging

Optical coherence tomography (OCT) is a promising optical imaging technique that has many applications in biomedical research as well as in clinical medicine. OCT aides in the diagnosis and follow up of diseases as it can provide detailed images of retinal diseases such as diabetic retinopathy (DR), glaucoma, and AMD. In particular, the junction of the ISOS layer of the photoreceptors has been visualized on SD-OCT B-scans [33, 58–61]. Three-dimensional (3-D) OCT retinal images are composed of a series of cross-sectional scans (B-scan) from top to bottom (in the z-x plane, as shown in Figure 2.3)of the scanning region on the retina. Each B-scan consists of certain number of high-resolution one-dimensional (1-D) scans known as A-scans [34]. 3D-OCT data sets are large and they require the analysis of numerous cross-sectional images to identify delicate structural changes. Visualization methods which rapidly

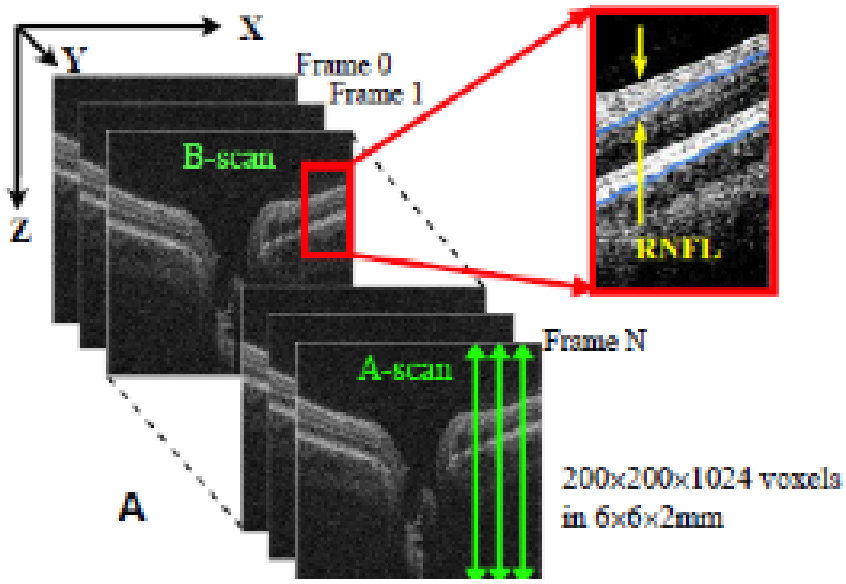

Figure 2.3. Generation of en face images from 2D B-scans.

identify ISOS junction pathologies are needed [62]. It is helpful to display 3D-OCT data in an en face manner. En face retinal imaging is an emerging imaging technique derived from SD-OCT. En face images are frontal scans generated from SD-OCT scans and produce layer-by-layer views of the retina. The en face fundus image, which is generated by axial summation of 3D OCT data, can be correlated with fundus photography and fluorescein angiography (FA). This technique selectively displays specific depth ranges in the retina, thus enhancing the contrast of retinal structure alterations [16, 63].

The ISOS en face images generated from normal subjects show clear visualization of the retinal structures. In patients with AMD the en face images display non-uniform texture, signifying topographic changes in the ISOS layer [33]. Using the powerful imaging capabilities

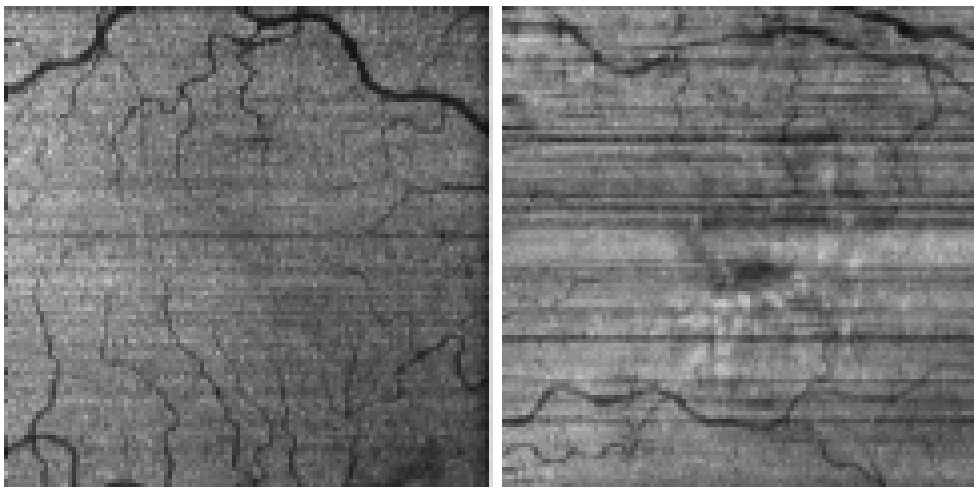

Figure 2.4. ISOS en face images of healthy eye (left) and diseased eye (right).

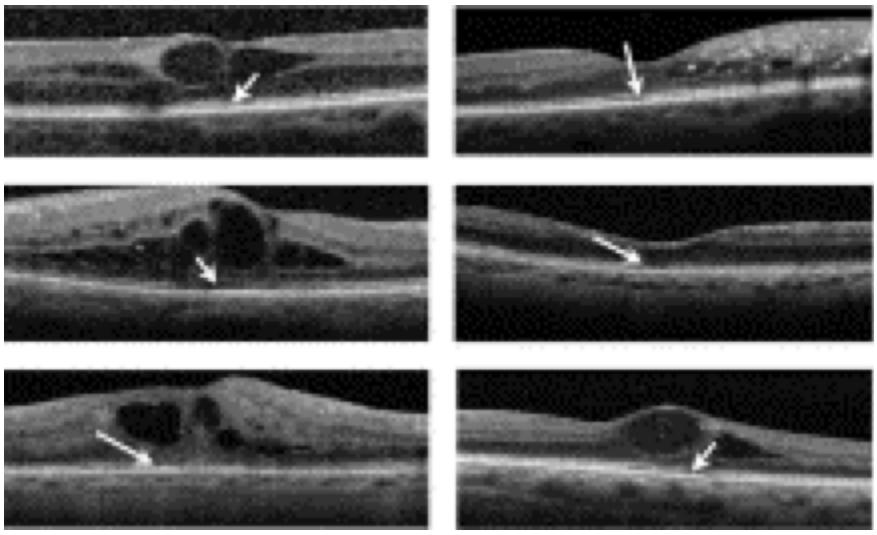

Figure 2.5. Six spectral-domain optical coherence tomography images through the fovea showing photoreceptor inner segment/outer segment (ISOS) junction layer disruption in patients with diabetic macular edema. The arrowheads correspond to ISOS junction.

of AO and SD-OCT, retinal cell layers and substructure visualization has been greatly improved and can therefore be used for detection and monitoring of a variety of retinal diseases [33, 64]. Figure 2.4 and Figure 2.5 show en face and B-scan images of patients with AMD and DR, respectively.

2.4 Previous work done on retinal image analysis

Automated counting and analysis of photoreceptor cells in high-resolution retinal images generated by an AO imaging system is important due to its potential in screening and diagnosis of diseases that affect human vision. Certain diseases cause the death of photoreceptor cells. Thus, the accurate and automatic quantification of these irregularities is important as it can aid in the detection, diagnosis, and follow-up of early cone dystrophy [22, 53]. A great deal of research has been done on different cell counting methods, and most of the methods are based on the specific properties of the cell to be counted. A drawback in recently reported photoreceptor cell counting methods is that they require user input of cell structure parameters. We review the work done by some principal groups on cell density estimation.

2.4.1 Photoreceptor regularity determination

In the method developed by Li et al [18], the images are first preprocessed using unsharp masking to remove low frequency spatial variations while retaining higher frequencies that represent the cells. After noise removal, the images are binarized to extract the cells. Morphological dilation is applied to the binarized image by applying a mask with the window size equal to the minimum cell spacing. The minimum spacing between cells is a parameter which must be manually estimated.

Chui et al [6] used a routine similar to the one described in [18]. As the photoreceptor cone mosaic includes a wide range of cone spacings, they included in their algorithm a filter that uses three different filter sets; one for large, medium, and small cone spacings. The human operator chooses the filter sets for the particular region in the retinal image which is being analyzed. In [4] the authors used an automated cone photoreceptor counting algorithm which first corrects for a non-uniform image background. Their methodology included morphological operators and a centroiding algorithm for the initial approximation of cone locations. The estimated cone locations are then filtered to provide a final cell count. The filter parameter is determined according to the eccentricity and requires some manual input. Results for their method are shown in Figure 2.6.

Xue et al [5] developed a histogram-based method for quantifying the density of cone photoreceptor cells. In their method, a difference image is obtained by first processing the original image with a Gaussian low-pass filter and subtracting the smoothed image from the original. Cells are detected by raster scanning the difference image and searching for pixels with intensities in a specified range. The spacing between cells is manually determined and used as input to the algorithm. Each time a pixel with intensity in the specified range is found, a region with dimensions equal to the predetermined spacing is marked to represent a detected cell. The steps of their algorithm are shown in Figure 2.7.

In [21] the authors estimate the density of cone cells by using an adaptive sampling window where the window size is adjusted to contain a fixed number of cones. Loquin et al [22] develop an algorithm based on a recursive construction of connected components which are thresholded

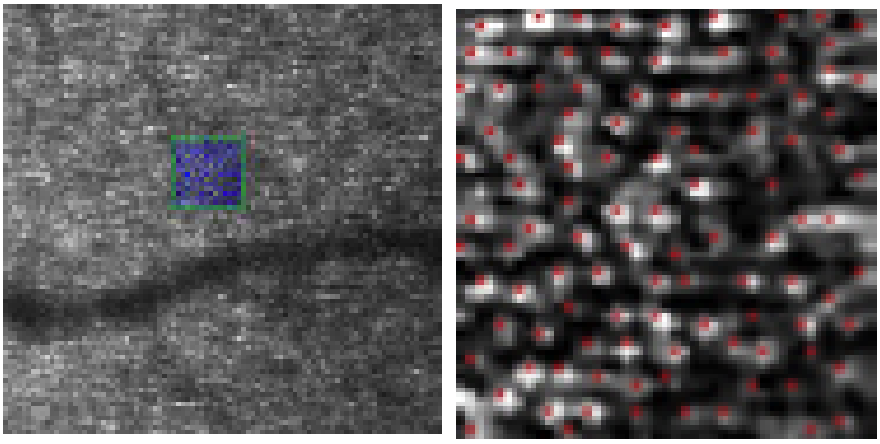

Figure 2.6. Photoreceptor density estimation by Mujat et al [4].

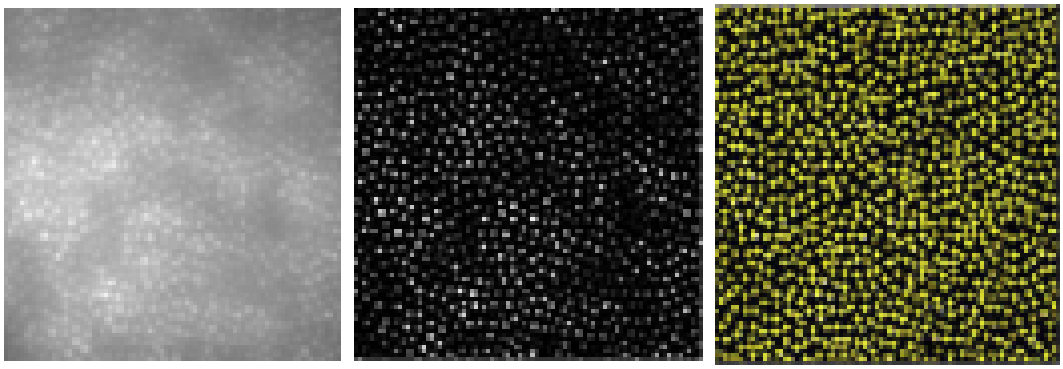

Figure 2.7. Photoreceptor density estimation by Xue et al [5].

when the seeds of the recursions are the regional maxima of the image. The outcome of the algorithm is a labeling of the AO image which is then used to segment the image with a marker-controlled watershed algorithm. As the images may vary according to acquisition conditions or the presence of disease, the authors included an interactive technique to tune certain parameters. The physician is therefore the judge of the best trade-off between cones which are correctly and incorrectly detected. Although the afore-mentioned methods provide results which are close to the expected results, nearly all of them require some user intervention to input cell-specific parameters. Difficulties in automation stem from variability in cell-spacing across a single image. Other challenges arise during imaging acquisition due to system noise as well as due to motion blur when the patient blinks or moves his or her eye. We have developed photoreceptor cell density estimation methods for both the spatial domain and the frequency domain [23, 24]. In our method, we use a circularly symmetric band-pass filter in which the parameters are automatically determined and in which the cellular structure is visualized clearly, thus facilitating cell density quantification and eliminating the need for user-intervention.

2.5 Level-set segmentation and analysis of images

The purpose of image segmentation is to partition an image into meaningful areas. There exists a great deal of literature on image segmentation algorithms using level-sets. The popularity of level-set methods as a general framework for image segmentation has been growing [65–74]. As the level-set evolution depends on forces computed from local image data, a common drawback of existing level-set algorithms is that the final result is highly dependent on contour initialization. In addition, since partial deferential equations are solved to promulgate

the initial contour towards the boundary of an object, they can be computationally expensive [66, 67].

Cremers et al [75] propose a novel approach based on a level set formulation of the Mumford-Shah functional [76] with shape priors. They include a labeling function to indicate image regions where it is favorable to enforce the shape prior. By doing so, various objects can be segmented and familiar shapes can be differentiated from non-familiar ones.

Chan et al [68] build upon the work of Cremers et al [75] by allowing translation, scaling and rotation of prior shapes, thereby overcoming the problem of unknown locations, poses, and sizes of objects.

Since the Chan-Vese model [2] may not work well on some shapes, Huang et al [69] use a manually defined shape model to perform segmentation. The Chan-Vese model [2] is applied to obtain an initial segmentation, after which shape models are defined using the results from initial segmentation. Once the initial shape is modeled, they estimate the location and the size of the segmented shape region to dynamically adjust the shape model and incorporate the model into the Chan Vese energy minimizing function [2, 69] .

Liu et al [70] propose a level-set method to segment the prostate in magnetic resonance imaging (MRI) images for the analysis of prostate cancer. They develop an unsupervised method based on level-set with shape priors to segment the prostate from multispectral MR images that do not require training. As MR images are prone to noise and as the prostate anatomy is complex, the authors must deal with noisy images in which boundaries are not clearly defined. Therefore they assume that the prostate shape is elliptical and they find an

ellipse which fits the prostate region to initiate the level-set and constrain the level-set evolution. The prostate boundary is then found by applying the level-set method with shape priors [70].

In many level-set models, shape and image energies have been proposed that include weighting factors to balance the importance of the energies in the segmentation process. More often than not, the weights must be empirically tuned to find the best fit. In order to overcome this problem, Chen et al [71] base the energy on regional intensity distributions and show that the image and shape energy are approximately the same magnitude, therefore ruling out the use of tuned weighting factors. They apply their technique to challenging pelvis CT scans with appreciable results.

The recognition of aircrafts in high resolution satellite images has many useful applications. However due to the complexity of the foreground and background, pixel-based methods for recognition usually do not work. In order to overcome these complications, Liu et al [77] integrate shape priors into the segmentation process using a coarse to fine approach for segmentation of aircrafts. In the coarse stage, the pose of the aircraft is estimated using template matching. In the fine stage a parametric shape model is derived using methods to reduce the problem dimensions whilst retaining a good sample space description. A combination of region information and shape priors is used to segment the aircraft using a level-set method and the parameter results from the segmentation are employed to recognize the aircraft.

Although Chan and Vese [2] suggest using multiple initial conditions, doing so is not always feasible and often increases the computational complexity of the problem. Yingjie et al [72] therefore introduce a method to determine an appropriate initial contour that can speed up

the evolution of curves and lead to appreciable segmentation results when applied to medical images.

As medical images tend to be prone to noise and have objects with weak edges, Yang et al [73] formulate a new speed function for the conventional level-set method by incorporating statistical region information into the fundamental level-set model to improve the robustness of the segmentation of such corrupted medical images. Their method has advantages over classical level-set algorithms in the case of images with weak or fuzzy edges.

When segmenting moving objects from a sequence of images, one must use the appropriate segmentation methods which can deal with motion and shape deformations. Fundana et al [74] found that the placation of active contours for image sequence segmentation gives promising results. They therefore propose a level set method which minimizes an energy functional that contains the standard Chan-Vese [2] functional as well as an interaction term which uses the segmentation results of the previous frame to be used as a shape prior for the current frame. They apply their method to real and synthetic image sequences with promising results.

In the analysis of microscopy images, one of the major challenges is the segmentation of thousands of densely packed cells which have varying sizes and orientations and which often overlap. Large variations in intensity across the image acquired during the acquisition process complicate the problem further. Gelas et al [31] address these complications by incorporating a spatial intensity model of cell nucleus into the Chan-Vese model [2] to aid cell segmentation from microscopy datasets. The intensity distribution of cell nuclei is modeled as a Gaussian distribution with constant intensity background. The method when applied to a variety of

microscopic data yields experimental results which validate the effectiveness of the proposed method .

Traditional level-set and active contour models often do not give promising results when segmenting livers from MR images as a result of the noise and low gradient response of the liver boundary. The leakage and over-segmentation problems are overcome by Cheng et al [78] by using a novel level set based variational approach which incorporates shape prior knowledge into the Chan-Vese model [2] to be used for liver segmentation from MR images. Statistical methods are used to acquire the shape priors and the training process allows prior shape to be placed independently of the position of the region of interest.

In [67], the authors proposed a multi- resolution approach that uses wavelets. They improve the convergence speed by using a coarse resolution for curve initialization as the coarse resolution contains strong edges for the object to be segmented. In [79] the authors add to the Chan-Vese model [2] a restriction item that is a non-linear heat equation with balanced diffusion rate to eliminate the re-initialization procedure. In [80] the authors present a new level-set method which combines the average values of global regions and local boundary information to detect lung nodules in CT images. In [81] the authors extend the Chan-Vese level-set [2] for ultrasound image segmentation. Their method introduces a wavelet multi-resolution analysis to create an edge representing mask to spot edge information in the image. In [82] the authors propose methods which do not require solutions of partial deferential equations and are therefore fast. The method uses region information to guide the evolution of initial curves.

In most of these methods, specifically the methods which use the Chan-Vese model [2] as a foundation, the placement of the initial contour can have a significant effect on the segmentation outcome. In some applications, the introduction of shape priors can facilitate the segmentation outcome as those objects which match a target shape are segmented. There are many methods by which shape can be introduced. We include in our literature survey those models which incorporate Fourier descriptors as part of the level-set segmentation process as we have found Fourier descriptors to be an effective way to compactly represent boundary information. Yang et al [83] propose a novel curve matching energy function to measure shape similarity between a target and test object. They use elliptic Fourier shape descriptors to represent the contour of human shapes, which are to be recognized from a sports dataset, and this contour is used as a shape prior to guide the curve evolution. A training data-set of contours is used as a template to determine the category of an unknown image based on matching. Prisacariu et al [84] present a method for finding nonlinear shape manifolds and use them as shape priors in level set based segmentation and tracking. They also represent shapes with elliptic Fourier descriptors and a latent space is learned by building the elliptic Fourier descriptors for the set of training contours and finding their low dimensional manifold. Charmi et al [85, 86] use Fourier-based shape alignment to incorporate geometric shape prior into snakes as well as into region-based active contours. Prior knowledge is obtained by using a reference shape which is used to define a new energy term obtained through a Fourier-based shape alignment.

Our work has a flavor that is similar in nature to the work done by Charmi et al [86]. In our work we use the Fourier coefficients of a polygonal curve obtained from actual pathologies

visible in the en face retinal images to represent shape priors which guide the curve evolution process. We compute an averaged pathology image from a number of actual pathology images by averaging the Fourier transforms of the images. A polygonal curve is obtained from this averaged image and is used as the target shape during the segmentation process. We use a subset of the Fourier descriptors which provides several benefits. It reduces the amount of computation required as the full set of coefficients are not being used. In addition, it automatically introduces some degree of smoothness during the segmentation process as the lower order coefficients contain basic structural information and the higher order coefficients that correspond to finer detail. The novelty of Charmi's method [86] method lies on the definition of a Fourier-based alignment energy function defined by curvature to measure the shape similarity between a target curve and an evolving curve. We focus our study on the description of shape priors using Fourier descriptors to simulate pathologies occurring in the human retina. The shape signatures are derived using the centroid distance function. We obtain and observe the segmentation of pathologies visible in en face images generated for seven layers of the retina and attempt to analyze the progression or recession of disease as the pathologies take shape and grow or shrink across the layers.

CHAPTER 3

PHOTORECEPTOR CELL REGULARITY ANALYSIS IN ADAPTIVE OPTICS RETINAL IMAGES

3.1 Introduction

Imaging of the retinal tissue of the eye is necessary for the diagnosis and treatment monitoring of many retinal diseases. However, aberrations in the optics of the human eye impose limits on the resolution at which the retina can be imaged. Adaptive optics (AO) provides retinal imaging at cellular levels and allows the visualization of the cone photoreceptor cell mosaic in human eyes. Measurement of photoreceptor cell density has the potential to play an important role in screening and diagnosis, as well as in the understanding of the retinal disease pathophysiology. Therefore, the automated analysis of photoreceptor cells in AO retinal images is needed to provide quantitative information on cell density under normal and diseased conditions since manual counting of cells is infeasible when a large number of images have to be processed [5, 6, 18]. A drawback in recently reported photoreceptor cell counting methods is that they require user input of cell structure parameters. We develop a method that overcomes this shortcoming by using content-adaptive filtering (CAF). In this method, image frequency content is initially analyzed to design a customized filter with a passband to emphasize cell structures suitable for subsequent processing. The McClellan transform [1] is used to design a bandpass filter with a circularly symmetric frequency response since retinal cells are circular in

nature and have no preferred orientation. The automated filter design eliminates the need for manual determination of cell structure parameters, such as inter-cell spacing. Following the pre-processing step, cell density estimation is performed on the binarized filtered image by finding regional points of high intensity. Photoreceptor cell estimates using this automated procedure were found to be comparable to manual counts (gold standard). The proposed method when applied to computer-generated test images as well as to retinal images showed overall improved performance when compared with previously reported methods requiring user-supplied input.

3.2 Spatial domain analysis of cone mosaic in AO retinal images

We have developed a spatial domain, content-adaptive filtering (CAF) method that uses band-pass filtering to uncover cellular structure whilst removing very high noise and very low frequency variations [23]. The CAF cell count estimation method consists of two major steps: (i) design of a customized bandpass filter using the McClellan transformation [1] which is used for image preprocessing and (ii) threshold-based image binarization and cell density estimation. We will first outline the image acquisition process.

3.3 Image acquisition

Retinal images were acquired in a visually normal subject using a bench-top adaptive optics retinal imaging system consisting of 3 main components: wavefront sensing, wavefront error correction, and retinal imaging. For wavefront sensing, a spatially filtered collimated 780 nm laser diode entered the eye and was focused onto the retina by the optics of the eye. Light reflected from the retina created an aberrated wavefront at the pupil plane. The wavefront was sampled with a lenslet array positioned at a plane conjugate with the pupil of the eye. The

lenslet consisted of a 65x65 array of lenses, each with a focal length of 24 mm and a diameter of 400 μm. The resulting image (640x480 pixels, 8-bit) comprised a two-dimensional (2D) array of spots and was acquired at 30 Hz by a charge-coupled device (CCD) camera. For wavefront error correction, a micro-electromechanical system (MEMS) deformable mirror (DM) was placed at a plane conjugate with the pupil of the eye. The DM was 4.9x4.9 mm^2 and consisted of a 12x12 array of elements with 0.45 mm spacing and a stroke of 6 μm. During AO correction, closed loop control of the DM minimized the wavefront error in 20 iterations with a gain of 0.2. For retinal imaging, a flash lamp illuminated the retina and a second CCD camera acquired a retinal image (1600x1200 pixels, 8-bit) after AO correction [87]. The use of AO resulted in improvement in the resolution and contrast of retinal images, allowing visualization of the photoreceptor cell mosaic. A central portion of the retinal image was cropped and contrast enhanced by stretching intensity values between 0 and 255. The images were analyzed using the CAF algorithm and the methods proposed by [5] and [6], which will hereafter be referred to as the histogram and threshold methods, respectively. The counting methods were applied to a retinal image from a human subject. Images with 5 different cell spacings were generated by scaling the original retinal image 1 to 2 times in increments of 0.25.

3.4 Cell density estimation using content-adaptive filtering (CAF)

The CAF cell density estimation method consists of two major steps: (i) design of a customized bandpass filter using the McClellan transformation [1] and preprocessing the image with this filter and (ii) threshold-based image binarization and cell count estimation. In this

section we describe these two steps and provide a brief description of the histogram and threshold methods used for comparison with the CAF method.

3.4.1 Bandpass filter design using the McClellan transform [1]

The cell information content of interest is mainly confined to a bandpass frequency region. A circularly symmetric 2D bandpass filter is designed in the CAF method to selectively pass only frequencies corresponding to the cell information content in the image. The parameters of the filter are chosen such that enough bandpass information is retained to capture cells of different shapes and sizes. The effects of slow-varying illumination are filtered with a lower stop-band and the high frequency noise corresponding to insignificant cell content or noise is removed with an upper stop band. The cut-off frequencies are chosen by an automated procedure for assessing the frequency content using horizontal and vertical image intensity profiles. The 2D circularly symmetric filter is conveniently designed by applying the McClellan transformation to a one- dimensional (1D) prototype filter [1] .

For several years, optimization algorithms have been developed to solve design problems related to finite-duration impulse response (FIR) digital filters. FIR digital filters have certain properties which make them popular for digital signal applications. Parks and McClellan developed a lowpass approximation of the desired response on two disjoint intervals; the passband and the stopband [1]. This approximation uses the Remez exchange algorithm and Chebyshev approximation theory to design filters with an optimal fit between the desired and actual frequency responses.

Consider a 1D filter with impulse response $g[n]$ and duration N. The frequency response $G(e^{j\omega})$ of the 1D filter can be written in the form

$$G(e^{j\omega}) = \sum_{n=0}^{M} b(n)\cos(n\omega). \tag{3.1}$$

where $M = \frac{N-1}{2}, b(0) = g(M)$, and $b(n) = 2g(M-n), n = 1, 2, ..., M$. A 2D digital filter with an impulse response $h(k,p), k = 0, 1, ..., N_1 - 1; p = 0, 1, ..., N_2 - 1$ has a frequency response defined by the 2D Fourier transform:

$$H(e^{j\omega_1}, e^{j\omega_2}) = \sum_{k=0}^{N_1-1}\sum_{p=0}^{N_2-1} h(k,p)e^{-j(k\omega_1+p\omega_2)}. \tag{3.2}$$

If the impulse response is symmetric:

$$\begin{aligned} h(N_1 - m - 1, p) &= h(m,p), m = 0, 1, ..., n_1 = \frac{N_1 - 1}{2} \\ h(k, N_2 - m - 1) &= h(k,m), m = 0, 1, ..., n_2 = \frac{N_2 - 1}{2}. \end{aligned} \tag{3.3}$$

then the frequency response can be written as

$$H(e^{j\omega_1}, e^{j\omega_2}) = e[^{-}j(n_1\omega_1 + n_2\omega_2)]\hat{H}(\omega_1, \omega_2). \tag{3.4}$$

where

$$\hat{H}(\omega_1, \omega_2) = \sum_{k=0}^{n_1}\sum_{p=0}^{n_2} a(k,p)\cos(k\omega_1)\cos(p\omega_2).$$

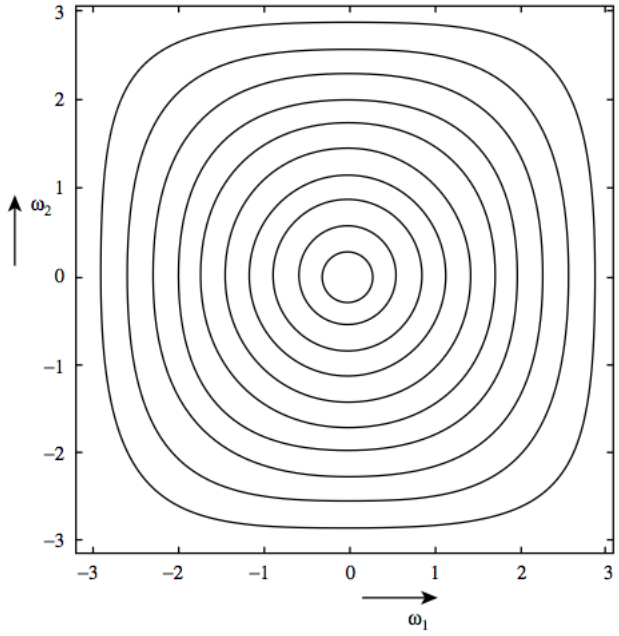

Figure 3.1. Contour plot of the McClellan transformation [1],
$F(\omega_1, \omega_2) = 0.5\cos(\omega_1) + 0.5\cos(\omega_2) + 0.5\cos(\omega_1)\cos(\omega_2) - 0.5$.

The frequency response $\hat{H}(\omega_1, \omega_2)$ is obtained from the 1D response $G(e^{j\omega})$ by applying the McClellan transformation for frequency mapping given by $\cos\omega = A\cos\omega_1 + B\cos\omega_2 + C\cos\omega_1\cos\omega_2 + D$. As ω varies, a series of contours which describe the 2D frequency response is generated (Figure 3.1). If the choice of variables A, B, C, and D are each chosen to be 0.5, then the transformation will map a low pass 1D filter to a low-pass circularly symmetric 2D filter. In the case of retinal cells, it has been observed that the photoreceptor cells have no preferred orientation; therefore it is desirable to process the images using such a circularly symmetric bandpass filter.

3.4.2 Filter parameter selection

Horizontal and vertical 1D profiles of the image are extracted from the central row and column of the image. The profiles in both directions are observed to have the same rate of change and are combined into a single 1D profile. An example of an AO retinal image showing the photoreceptor cell mosaic and the 1D signal derived from the image is shown in Figure 3.2, respectively. The frequency variations in these profiles are analyzed and used as a basis to designate the location of the lower and upper stop and bandpasses for the filter. The original profiles are slightly smoothed to remove very high frequency variations using an averaging filter. The locations of the peaks are found by determining whether there is a deep valley on either side of a point. If a deep valley is located on both the left and right side of a point, this point will be categorized as a peak. In this way, prominent peaks in the profile can be found. The distance between peaks is an estimate of the frequency occurrence of the cells. A large gap between prominent peaks indicates a low rate of change in frequency values and this translates to a lower occurrence of cells.

3.4.3 Filter response obtained with the McClellan transformation [1]

The occurrence of peaks obtained using the intensity signals are utilized as input to the McClellan transformation [1]. In our simulations, the lower and upper cut-offs are defined by the average of the upper and lower 50% of the cell spacings respectively. Other definitions can be applied, such as selecting the average of the upper or lower 10% of the estimated cell spacings. The McClellan transformation [1] is then utilized to obtain a 2D filter from the 1D prototype filter. One- and two-dimensional views of the filter are shown in Figure 3.3. The results of

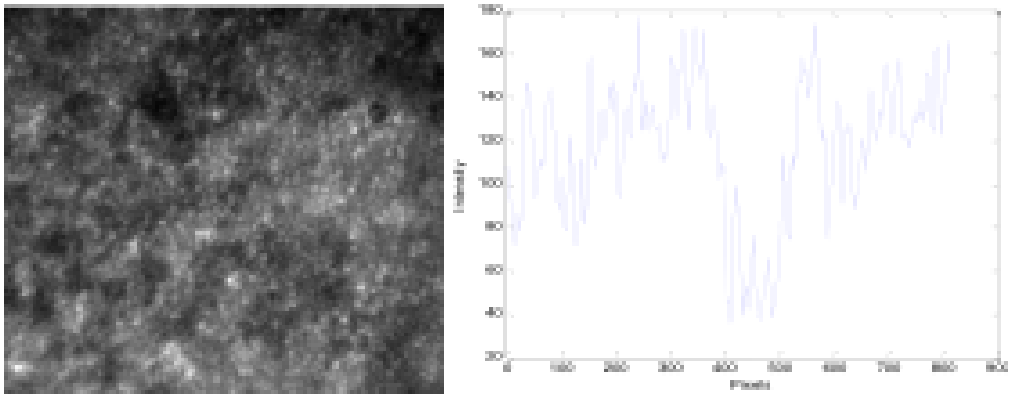

Figure 3.2. Original retinal adaptive optics image showing photoreceptor cells (left). Combined 1D horizontal and vertical intensity profile (right).

applying the 2D filter to the retinal image shown in the left-hand-side of Figure 3.4 can be seen in the right-hand-side figure of Figure 3.4. It is clearly observable that the filtered image has much higher contrast than the original. Cellular structures are more visible and the boundaries between cells are emphasized. To estimate the number of cells, the filtered image is thresholded to separate high intensity pixels corresponding to photoreceptor cells from low intensity regions corresponding to the background by applying a function which finds the regional maximums i.e. image pixels surrounded by pixels of lower intensity value. Morphological operations are applied to the thresholded image to remove spurious pixels. The number of unique objects in the thresholded image is reported as the cell count.

3.5 Results of photoreceptor cell counting in the spatial domain

The proposed methods are applied to a retinal image from a human subject. Images with 5 different cell spacing are generated by scaling the original retinal image 1 to 2 times by

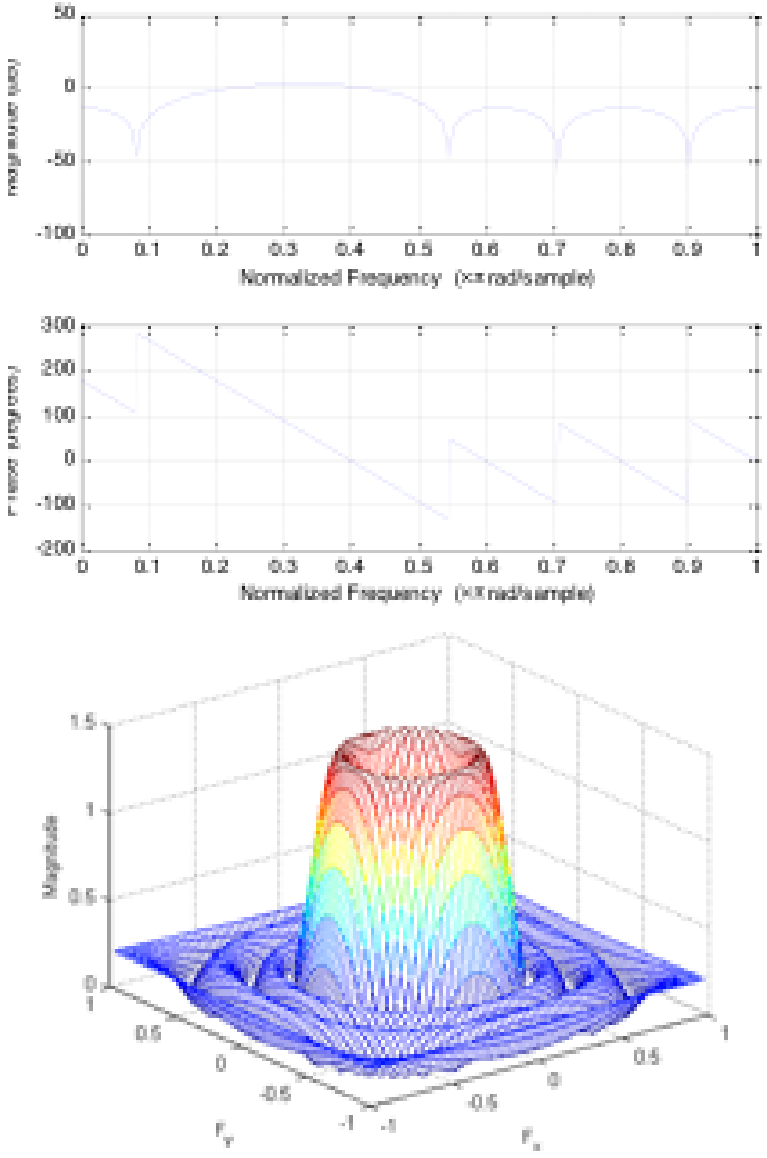

Figure 3.3. Top: 1D view of filter Bottom: 2D view of filter.

increments of 0.25. Cell count estimates obtained on a 122x122 image with CAF, histogram [5], and threshold [6] methods are plotted against manual counts as shown in Figure 3.5 (left) . The data points from the CAF, histogram [5], and threshold [6] methods were plotted as a function of manual counts. With all methods, a high correlation between the automated and manual counts was found (r = 0.99). The slopes of the best fit line were 1.02, 1.04, and 0.89 for data obtained by CAF, histogram [5], and threshold [6] methods, respectively. The y-intercepts of the best fit line were 13, 18, and 30 counts for data obtained by CAF, histogram [5] and threshold [6] methods, respectively. Data obtained by the CAF method is closest to the unity line. The CAF method provides accurate count estimates of photoreceptor cells comparable to manual counts.

Comparison of cell count estimates as a function of cell spacing obtained using CAF, histogram [5], and threshold [6] methods are shown in the left-hand-side figure of Figure 3.5. A similar trend of decreasing cell counts with increasing cell spacing was found with all 3 methods, as expected. A comparison of cell counting for a region of interest by manual counting, CAF, histogram [5], and threshold [6] methods is shown in the right-hand-side figure of Figure 3.6. Based on comparisons with manual count results, the optimum cell spacing for histogram [5] and threshold [6] methods were 7 and 2 pixels, respectively. Depending on the human operator, spacing determination can vary. A difference of only 1 pixel will result in 9% - 17% and 35% - 38% error in cell counts for the histogram [5] and threshold [6] methods, respectively. Figure 3.7 show the three different methods when applied to the entire retinal image. The distribution of detected cells is more uniform in the CAF and histogram [5] methods whereas a nonuniform

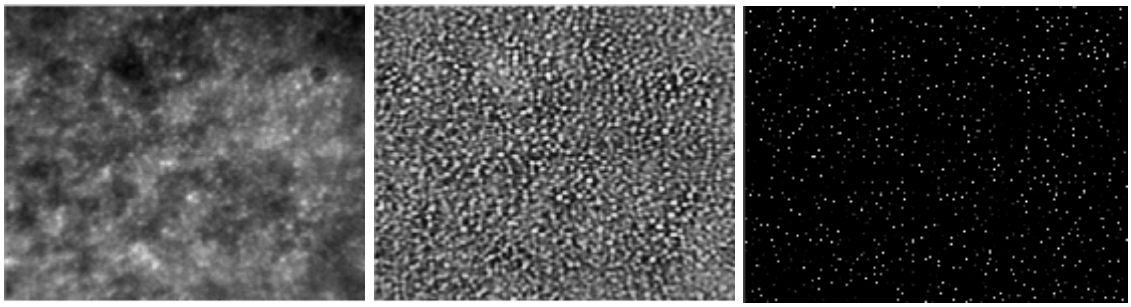

Figure 3.4. Left: Original AO image. Center: Filtered image using the McClellan transformation [1]. Right: Thresholded image.

distribution of detected cells (seen as areas of unusually high congestion) is observed using the method proposed by [6]. This can be due to the effect of selecting a cell spacing which is not optimum in the areas showing irregular distributions.

3.6 Conclusion and discussion

Cell counting and density estimation provide valuable information in many different scientific and medical environments. The CAF method provides accurate estimates of the number of photoreceptor cells, comparable to manual counts, and either comparable or improved performance relative to that obtained with the histogram [5] and the threshold methods [6]. However, both of these previously reported methods have the drawback of requiring information regarding cell spacing which must be manually adjusted for each image to provide accurate measurements. Application of the designed filter results in an image that enables a more accurate cell count and density.

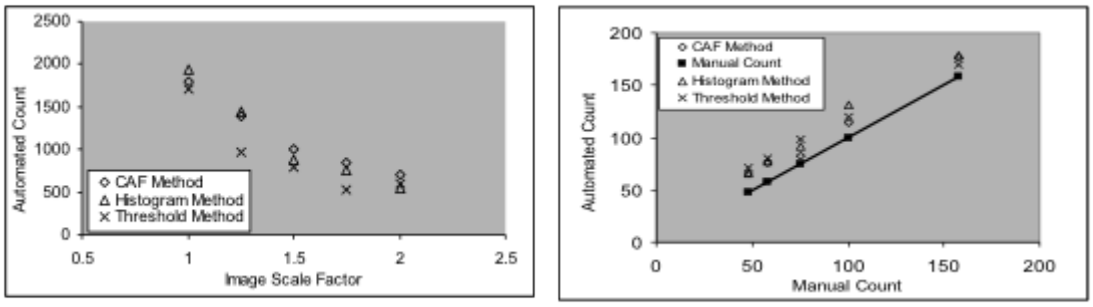

Figure 3.5. Left: Cell count estimates obtained in images with variable cell spacing. Right: Comparison of automated and manual counts for CAF, histogram [5], and threshold [6] methods.

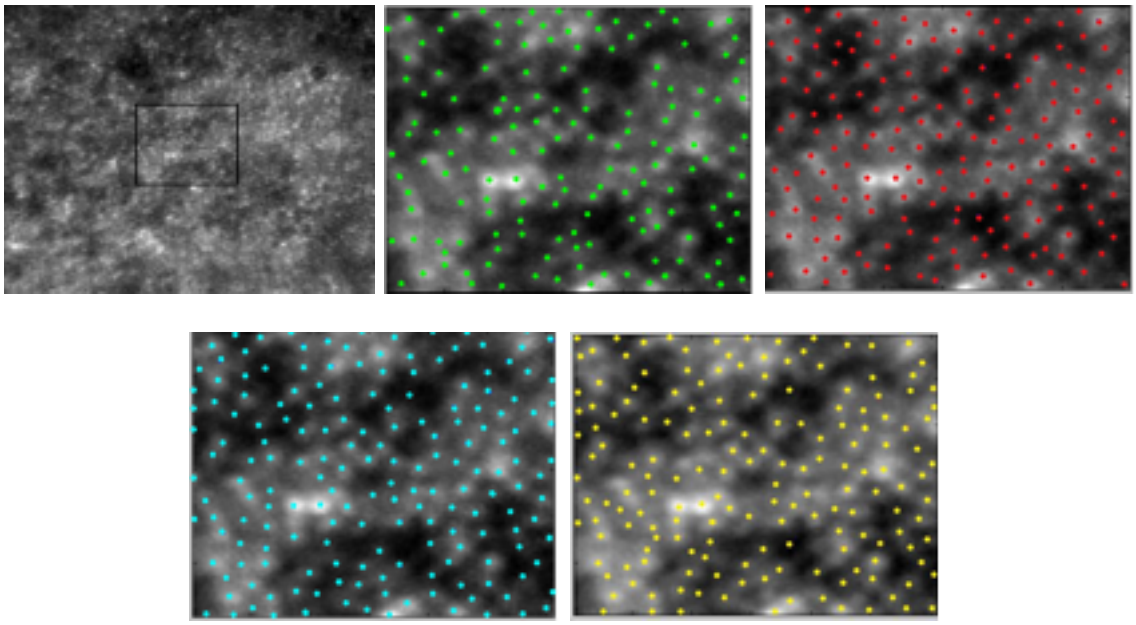

Figure 3.6. Top left: Original image with the region of interest indicated by a rectangular box. Top center: Marked cells counted manually. Top right: marked cells counted by CAF. Bottom left: marked cells counted by method in [5]. Bottom right: marked cells counted by method in [6].

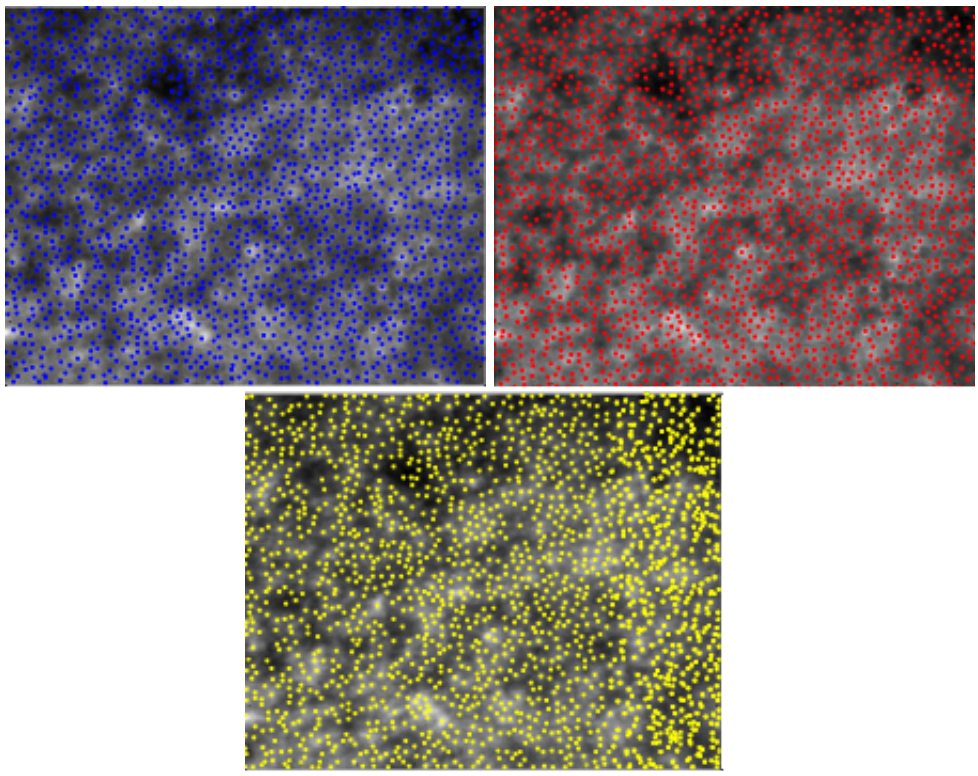

Figure 3.7. Distribution of cells counted by: CAF method (left); Histogram method [5](right); Threshold method [6] (bottom).

CHAPTER 4

FREQUENCY DOMAIN ANALYSIS OF CONE MOSAIC IN ADAPTIVE OPTICS RETINAL IMAGES

4.1 Introduction

A potential drawback of measuring photoreceptor density in the spatial domain is that the intensity profiles can be greatly affected by the presence of noise. Noisy peaks in the profile may be incorrectly identified as cells. In order to overcome this possible limitation, we analyze the cone mosaic in the frequency domain. The method we propose is significantly different from our previous work in that we describe an image model using a windowed two-dimensional (2D) lattice of pulses representing the cells and characterize the frequency content as decaying frequency domain pulses on the reciprocal lattice. Based on this we propose a frequency-based, local content-adaptive filtering (L-CAF) method that analyzes the image in the frequency domain and adaptively filters the image at local regions. As the frequency information is largely confined to a band-pass region, cell spacing information is determined from the discrete-space Fourier transform (DSFT) of the image. The DSFT of the image serves to determine the parameters for the design of a one-dimensional prototype of the Parks and McClellan band-pass, finite-impulse response filter [1].

Since the filter parameters are automatically calculated locally, it is therefore adaptable to different frequencies which are indicative of various cell spacings in the image. The theoretical

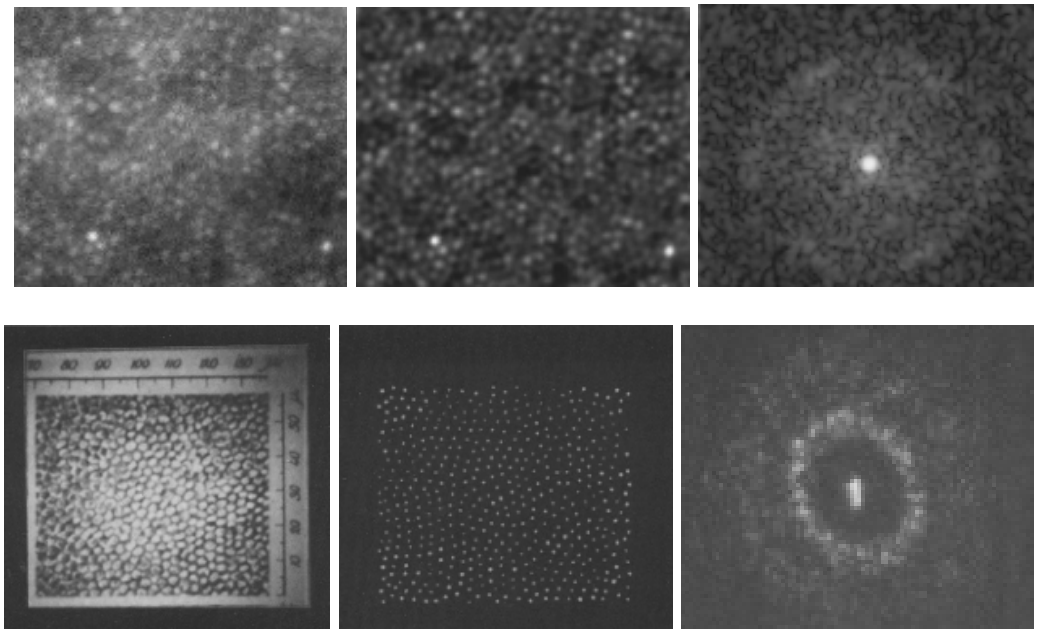

Figure 4.1. Ring-like structure observable in power spectrum of photoreceptor images. Top row: AO image showing photoreceptor mosaic before filtering (left). Photoreceptor mosaic after filtering (center). Power spectrum of cone mosaic (right) [7]. Bottom row: Patch of foveal cones seen end on (left). Sample points created by poking pinholes in centers of cells visible in foveal patch (center). Power spectrum of simulated receptor sampling array (right) [8].

framework we develop is aligned with the work done in [7] and explains the ring-like Fourier domain energy distribution observed in [7, 8]. In [7], the authors design a Butterworth filter to pass frequencies that were 0.1 to 1.2 times the sampling frequency of cones. These frequencies are chosen upon analysis of the power spectrum of the image. The top row of Figure 4.1 shows an adaptive optics (AO) image of the cone mosaic before and after filtering as well as the power spectrum of the cone mosaic. In [8], the authors obtain a foveal patch, as seen in the left-hand-side figure in the bottom row of Figure 4.1. The locations of the centers of the cells visible in the patch are used to create a simulated receptor sampling array and the power spectrum of this array was taken (Figure 4.1 center and right, respectively). The power spectrum images for both [7, 8] clearly show the circular ring-like structure. In our work, we give a theoretical analysis which explains the appearance of the ring. The performance of the proposed method is evaluated in a computer-generated test image with a known cell count and in an AO human retinal image with simulated variable cell densities with a manually determined cell count.

4.2 Continuous-space image analysis

Let R and Z denote the sets of real numbers and integers respectively. We will first consider an idealized retinal image that is noise-free and with uniform photoreceptor cell density such that the cells are centered on a uniform grid or lattice defined by vectors $\mathbf{v_1} = [v_{11}\ v_{12}]^T$ and $\mathbf{v_2} = [v_{21}\ v_{22}]^T$ where $\mathbf{v_k} \in R^2$ for $k = 1, 2$. Define matrix $\mathbf{V} = [\mathbf{v_1}\ \mathbf{v_2}]$. Define $\mathbf{t} = [t_1\ t_2]^T \in R^2$. Each cell is modeled as a 2D square integrable waveform or pulse of finite support, $g(\mathbf{t})$, of finite support that lies within a parallelogram $S_{\mathbf{V}}$ centered at $\mathbf{t} = [0\ 0]^T$ and sides defined by $\mathbf{v_1}$ and $\mathbf{v_2}$, as shown in Figure 4.2. Also $\mathbf{n} = [n_1\ n_2]^T \in Z^2$.

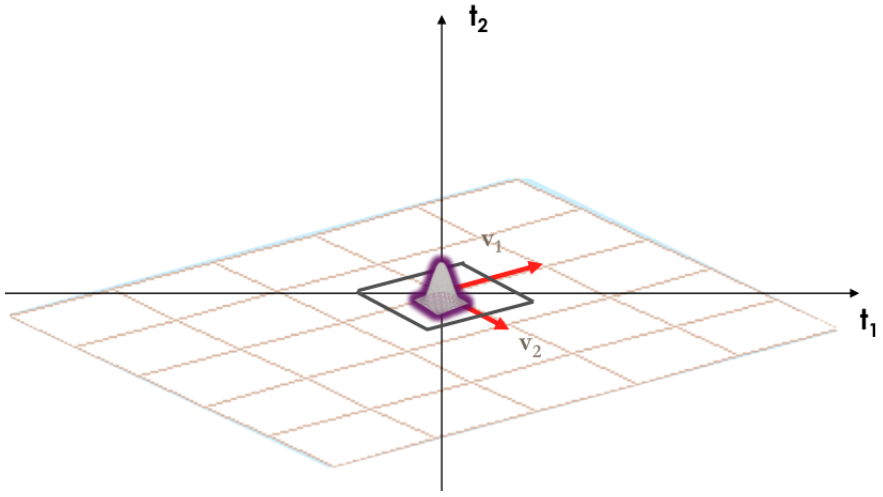

Figure 4.2. Uniform lattice with matrix defined by $\mathbf{V}$, showing cell pulse, $g(\mathbf{t})$.

The idealized infinite-extent continuous-space impulse train, show in Figure 4.3, is defined as

$$p_{\mathbf{V}}(\mathbf{t}) = \sum_{\mathbf{n}=Z^2} \delta(\mathbf{t} - \mathbf{V}\mathbf{n}). \tag{4.1}$$

The idealized infinite-extent pulse train, shown in Figure 4.4, over the lattice defined by $\mathbf{V}$ is given by

$$x_c(\mathbf{t}) = g(\mathbf{t}) * p_{\mathbf{V}}(\mathbf{t}) = \sum_{\mathbf{n}=Z^2} g(\mathbf{t} - \mathbf{V}\mathbf{n}). \tag{4.2}$$

Note that $x_c(\mathbf{t})$ and $p_{\mathbf{V}}(\mathbf{t})$ are both periodic with $x_c(\mathbf{t} + \mathbf{V}\mathbf{n}) = x_c(\mathbf{t})$ and $p_{\mathbf{V}}(\mathbf{t} + \mathbf{V}\mathbf{n}) = p_{\mathbf{V}}(\mathbf{t})$. Now $p_{\mathbf{V}}(\mathbf{t})$ can be expressed as a 2D Fourier series with harmonics defined by the reciprocal lattice $\overline{\mathbf{V}}$, (shown in Figure 4.5), with $\overline{\mathbf{V}}^T\mathbf{V} = 2\pi\mathbf{I}_2$ where $\mathbf{I}_2$ is the 2×2 identity matrix.

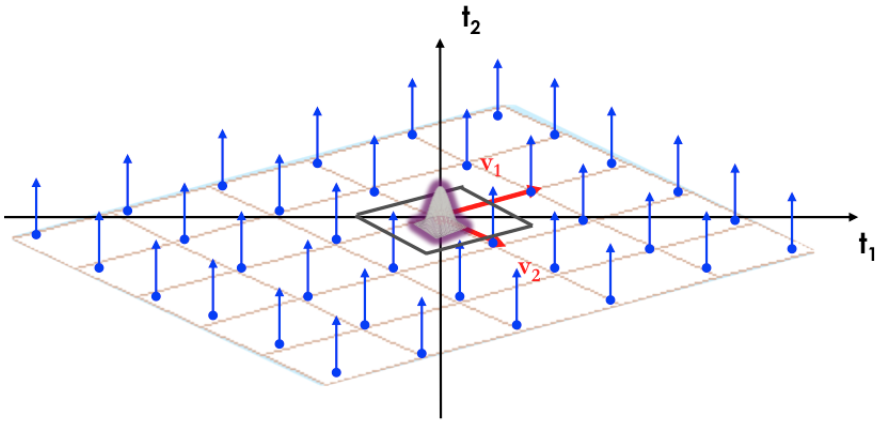

Figure 4.3. Impulse train defined by $p_{\mathbf{V}}(\mathbf{t})$.

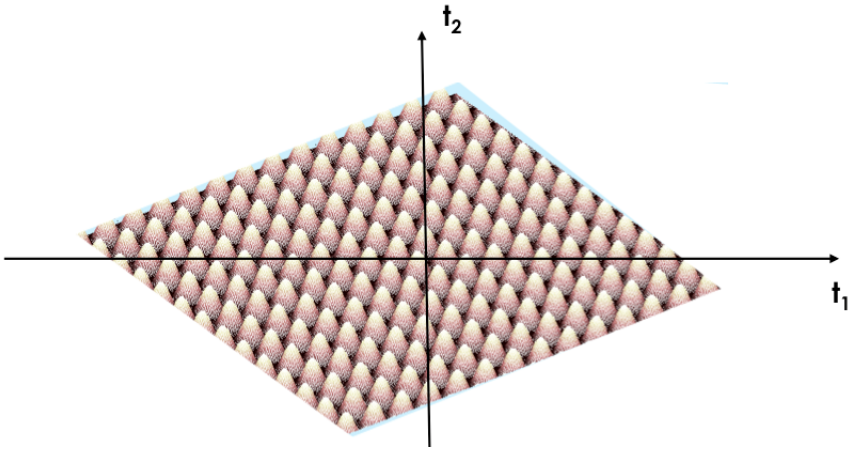

Figure 4.4. Pulse train defined by $x_c(\mathbf{t})$.

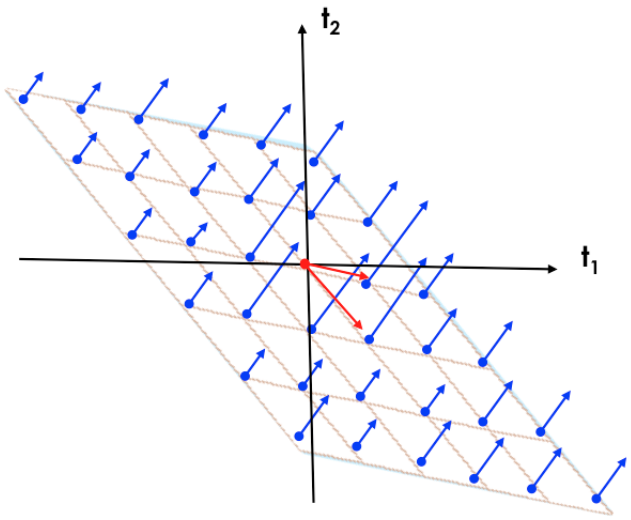

Figure 4.5. Reciprocal lattice, $\overline{\mathbf{V}}$ showing $P_{\mathbf{V}}(j\mathbf{\Omega})$.

The Fourier series expansion is given by

$$p_{\mathbf{V}}(\mathbf{t}) = \sum_{\mathbf{k}=Z^2} c_{\mathbf{k}} e^{j\mathbf{t}^T\overline{\mathbf{V}}\mathbf{k}}. \tag{4.3}$$

where

$$c_{\mathbf{k}} = \frac{1}{|\det \mathbf{V}|}\int\int_{\mathbf{t}\in S_{\mathbf{V}}} p_{\mathbf{V}}(\mathbf{t}) e^{-j\mathbf{t}^T\overline{\mathbf{V}}\mathbf{k}} d\mathbf{t}.$$

$$= \frac{1}{|\det \mathbf{V}|}\int\int_{\mathbf{t}\in S_{\mathbf{V}}} \delta(\mathbf{t}) e^{-j\mathbf{t}^T\overline{\mathbf{V}}\mathbf{k}} d\mathbf{t} = \frac{1}{|\det \mathbf{V}|}. \tag{4.4}$$

We will now determine the Fourier transform $X_c(j\mathbf{\Omega})$, $\mathbf{\Omega} = [\Omega_1\ \Omega_2]^T$, of the 2D signal $x_c(t_1, t_2)$. Noting that the following is a 2D Fourier transform pair

$$e^{j\mathbf{t}^T\overline{\mathbf{V}}\mathbf{k}} \leftarrow \mathcal{F} \rightarrow 4\pi^2\delta(\mathbf{\Omega} - \overline{\mathbf{V}}\mathbf{k}), \tag{4.5}$$

the Fourier transform $P_{\mathbf{V}}(j\mathbf{\Omega})$ of the signal $p_{\mathbf{V}}(\mathbf{t})$ is given by

$$P_{\overline{\mathbf{V}}}(j\mathbf{\Omega}) = \frac{4\pi^2}{|\det \mathbf{V}|} \sum_{\mathbf{k}\in Z^2} \delta(\mathbf{\Omega} - \overline{\mathbf{V}}\mathbf{k}). \tag{4.6}$$

Since $x_c(\mathbf{t}) = g(\mathbf{t}) * p_{\mathbf{V}}(\mathbf{t})$ it follows that

$$\begin{aligned} X_c(j\mathbf{\Omega}) &= G(j\mathbf{\Omega})P_{\overline{\mathbf{V}}}(j\mathbf{\Omega}) \\ &= \frac{4\pi^2}{|\det \mathbf{V}|} \sum_{\mathbf{k}\in Z^2} G(j\overline{\mathbf{V}}\mathbf{k})\delta(\mathbf{\Omega} - \overline{\mathbf{V}}\mathbf{k}). \end{aligned} \tag{4.7}$$

Since $g(\mathbf{t})$ can be modeled to decay smoothly as the Euclidean norm $||\mathbf{t}||$ increases, $G(j\mathbf{\Omega})$ decays rapidly as $||\mathbf{\Omega}||$ increases. Therefore due to the decay in the weights, $G(j\mathbf{V}\mathbf{k})$ of the impulses as $||\mathbf{k}||$ increases, only a few of the impulses corresponding to small values of $||\mathbf{k}||$ are significant, the energy in $X_c(j\mathbf{\Omega})$ is concentrated in impulses within a narrow annulus. Now suppose we observe the 2D signal with a spatial window $w_c(\mathbf{t})$ given by

$$w_c(\mathbf{t}) = \begin{cases} 1, & |t_1| \le \frac{T_1}{2}, |t_2| \le \frac{T_2}{2} \\ 0, & \text{otherwise.} \end{cases} \tag{4.8}$$

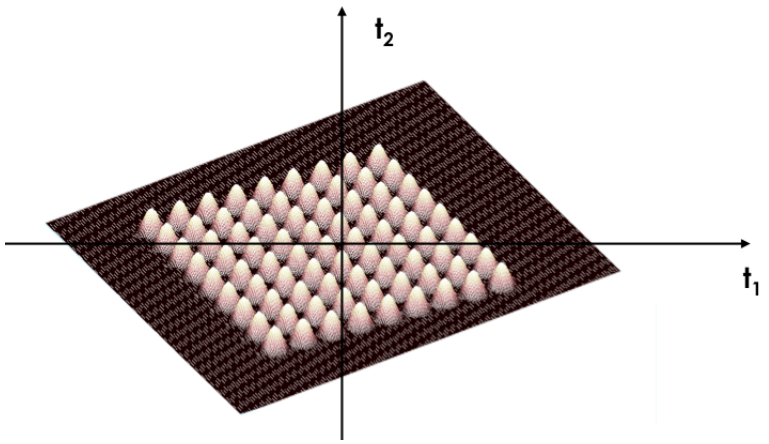

Figure 4.6. Windowed signal, $y_c(\mathbf{t})$.

The windowed signal $y_c(\mathbf{t}) = w_c(\mathbf{t})x_c(\mathbf{t})$, shown in Figure 4.6 has the following Fourier transform, shown in Figure 4.7

$$Y_c(j\mathbf{\Omega}) = \frac{1}{4\pi^2} X_c(j\mathbf{\Omega}) * W_c(j\mathbf{\Omega})$$
$$= \frac{1}{|\det \mathbf{V}|} \sum_{\mathbf{k}\in Z^2} G(j\overline{\mathbf{V}}\mathbf{k}) W_c(\mathbf{\Omega} - \overline{\mathbf{V}}\mathbf{k}). \tag{4.9}$$

where $W_c(j\mathbf{\Omega})$ is a 2D *sinc* function for the choice of the 2D uniform rectangular window $w(\mathbf{t})$. So $Y_c(j\mathbf{\Omega})$ consists of a sum of weighted shifted *sinc* functions, only some of which corresponding to small values of $||\mathbf{k}||$ contribute significantly to the energy of $y_c(\mathbf{t})$. The location

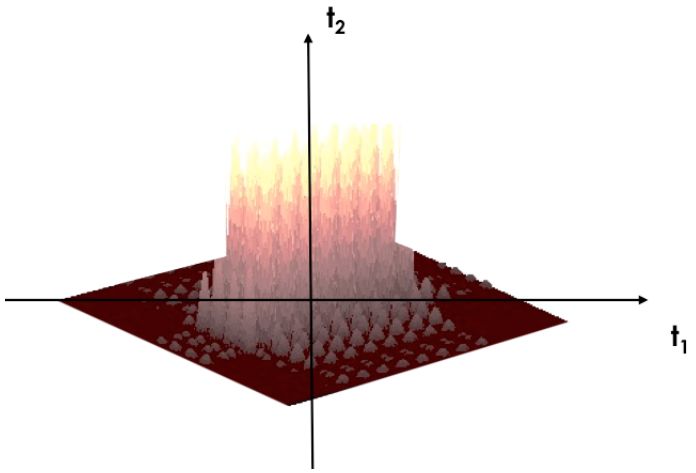

Figure 4.7. Fourier transform of windowed signal, $Y_c(j\mathbf{\Omega})$.

of the shifts are defined by the reciprocal lattice specified by $\overline{\mathbf{V}}$. If we rotate the lattice by an angle θ, as shown in Figure 4.8, we obtain a new lattice defined by

$$\mathbf{V}_\theta = \mathbf{R}_\theta \mathbf{V}, \mathbf{R}_\theta = \begin{bmatrix} \cos\theta & -\sin\theta \\ \sin\theta & \cos\theta \end{bmatrix}. \tag{4.10}$$

Since $\mathbf{R}_\theta^T \mathbf{R}_\theta = \mathbf{I}_2$, the reciprocal lattice after rotation is given by $\overline{\mathbf{V}}_\theta = \mathbf{R}_\theta \overline{\mathbf{V}}$ since it can be verified that $\overline{\mathbf{V}}_\theta^T \mathbf{V}_\theta = 2\pi \mathbf{I}_2$.

Now if $x_c^\theta(\mathbf{t}) = g(\mathbf{t}) * p_{\mathbf{V}}^\theta(\mathbf{t})$ then $y_c^\theta(\mathbf{t}) = w_c(\mathbf{t}) x_c^\theta(\mathbf{t})$ has a Fourier transform $Y_c^\theta(j\mathbf{\Omega})$ that is a rotated version of $Y_c(j\mathbf{\Omega})$. The above results point to the following characteristics of the Fourier transform $Y_c^\theta(j\mathbf{\Omega})$ of the windowed version of the idealized 2D train of pulses $g(\mathbf{t})$ located on the lattice defined by $\mathbf{V}_\theta$. $Y_c^\theta(j\mathbf{\Omega})$ consists of the sum of shifted Fourier transforms

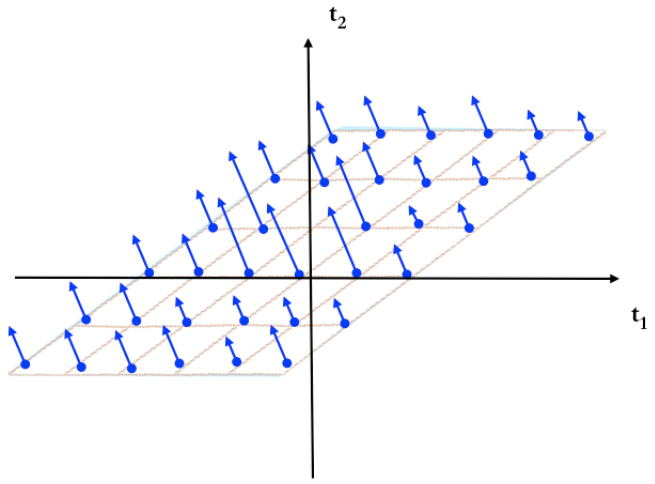

Figure 4.8. Rotated lattice, $\mathbf{V}_\theta$.

(sinc functions for the assumed rectangular windows) that are located on the reciprocal lattice $\overline{\mathbf{V}}_\theta$ with weights determined by $G(j\mathbf{\Omega})$ that decay rapidly with distance from the origin in the frequency domain. In the absence of prior information about θ, we note that the image energy in the frequency domain is largely contained within a circular band around the origin. If the image is not ideal and can be modeled with random variations in the shape, location, and amplitude of the pulses, then for the corresponding 2D random process it can be shown that the power spectral density will yield a spread in the energy in the frequency domain. However the energy will still be confined within a small circular frequency band, providing a theoretical explanation for the experimental observations in [7]. One notable feature about AO retinal images is that there is a significant slow variation of image intensity. If this is due to an additive contaminant, then high pass filtering with a narrow stop-band can eliminate the variation that is undesirable

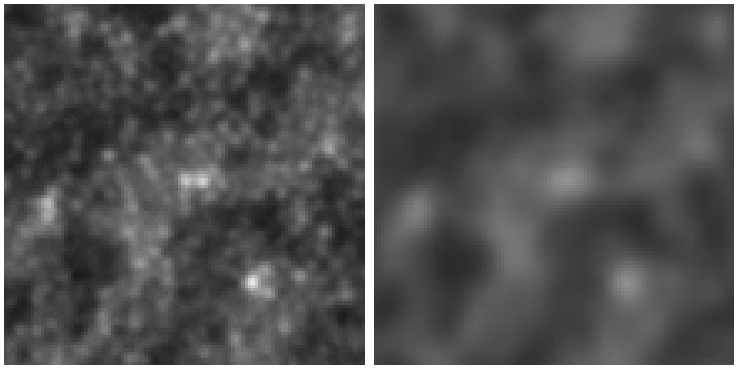

Figure 4.9. Left: AO retinal image showing photoreceptor cells. Right: Image on left blurred

for cell detection. On the other hand, if the contaminant is multiplicative then a suitable homomorphic operation can be used to suppress it. Our investigation shows that the variation can be modeled as an additive low-frequency contaminant. We note that in the brighter regions, the "valleys" between cells are less pronounced (Figure 4.9). This would not be the case if the contamination is multiplicative, as this would emphasize the intensity variation of the cellular structure. Moreover a multiplicative form would yield sideband modulation with small shifts around the reciprocal lattice locations but would show little energy in low frequencies except due to the direct current (DC) shift.

We will now briefly summarize the rationale for our approach. If the image is degraded with additive Gaussian noise, then with perfect knowledge of $g(\mathbf{t})$ a correlation type method can be used to detect the cells. However, in practice the pulses corresponding to the cell structure can vary, precluding the use of a fixed $g(\mathbf{t})$. The concentration of energy in a circular band determined by the low frequency components centered on the reciprocal lattice together with

the undesirable low frequency contaminant suggests the use of a circularly symmetric bandpass filter whose parameters are determined with a preliminary frequency-domain analysis. Once the AO retinal image is filtered we determine cell locations by searching for image maxima with constraints on cell separation based on the frequency domain analysis. Since there is variation in cell density with eccentricity from the fovea we use block-based processing, assuming quasi-periodicity of the image. Images of cone photoreceptor cells display an intensity peak at the center of the cell with a gradual decrease in intensity as the distance from the center of the cell increases. If we assume the optimum case in which the retinal image is noise-free and photoreceptor cell density is uniform such that the cells are distributed on a lattice-like structure, then we can use a number of template-matching schemes or cross-correlation detectors for spatial localization. In practice however, the optimum case cannot be realized for two reasons. First, photoreceptor cone density decreases with increasing retinal eccentricity [36]. Second, the pattern of photoreceptor cells, while following a tightly packed hexagonal cone mosaic, is variable across the retinal image. Hexagonal symmetry in the peripheral retina ceases to be present at higher eccentricities to help alleviate spatial aliasing effects [37, 88]. The DSFT of the image can provide a suitable solution for overcoming these problems associated with analyzing the image in the spatial domain.

sectionDiscrete-space image analysis

It should be noted that while our frequency analysis is performed on a continuous-space signal, the results can be done in an analogous fashion starting with a discretized space image and using the DSFT. As noted earlier, it is desirable to limit the information to what occurs

in the band and ignore the information which falls beyond the band. The circularly symmetric 2D filter obtained with a McClellan transformation is used to select the near optimal filter coefficients. The top row of Figure 4.10 shows (from left to right) the computer generated test image; the test-image with random noise added (mean = 3 and standard deviation = 10); and the noisy test image filtered with the L-CAF algorithm, respectively. The bottom row of Figure 4.10 shows the respective DSFT of each of the test images. The test image was then rotated by 270 degrees counterclockwise and the DSFT of the rotated image was computed, as shown in Figure 4.10 (bottom right). The visible bright peaks in both Figure 4.10 bottom left and bottom center are the *sinc* functions, which appear narrow due to the large size of "windowed" image, and we note the rotation of the reciprocal lattice (Figure 4.10, bottom right). Figure 4.10 (bottom center) shows the DSFT of the L-CAF filtered image with random noise. It can be seen that the DSFT in Figure 4.10 (bottom center) is nearly identical to the one in Figure 4.10 (bottom left) although due to the presence of noise, the sinc functions do not appear as bright as they do in the original. From Figure 4.10 (top right) we can see how filtering very effectively removes the high frequency noise and suppresses the low frequencies so that the foreground stands out clearly from the background.

In the DSFT of a human retinal image we would still expect to see the narrow *sinc* functions that are visible in an ideal image, however the variable periodic repetition of the cells causes the DSFT image to appear smeared. When done locally, analysis of the spectral density allows us to visualize energy bands and permits the cell spacing information to be obtained from regions

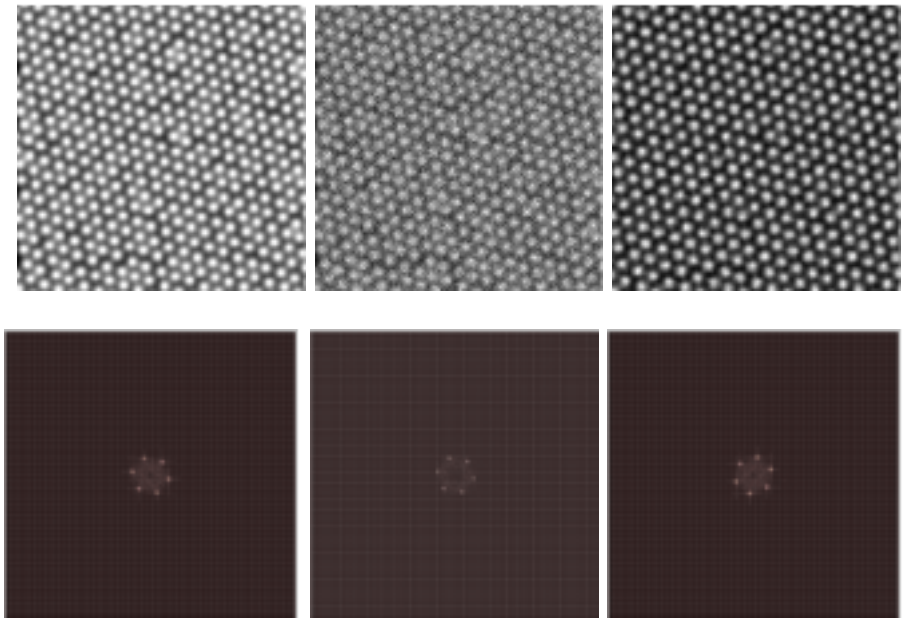

Figure 4.10. Top row, left to right shows the test image: original, with noise, after filtering. Bottom row shows the corresponding Fourier spectrums for each test image

of high energy concentration. By removing the high frequencies as well as the low frequencies which appear as intensity variations in the image, we can extract the cell frequency information.

4.3 Continuous-Space 2D Random Process Modeling

In the previous sections we analyzed the cone mosaic in the frequency domain using a deterministic modeling of the photoreceptor cell retinal image. In this section we will consider a random process modeling where the circular symmetry of the spectral content is better elucidated. We examine the spectral content of an AO retinal image by modeling it as a 2D random process or a random field instead of the deterministic model considered earlier.

Consider the AO image modeled as 2D random process expressed as:

$$Q = \{Q_{\mathbf{t}} : \mathbf{t} \in R^2\}. \tag{4.11}$$

where $Q_{\mathbf{t}}$ is a random variable for a fixed $\mathbf{t}$. The mean of the random process is given by

$$\mu_Q(\mathbf{t}) = E[Q_{\mathbf{t}}], \forall \mathbf{t} \in R^2. \tag{4.12}$$

The autocorrelation function of the random process is given by

$$R_Q(\mathbf{t}_1, \mathbf{t}_2) = E[Q_{\mathbf{t}_1} Q*_{\mathbf{t}_2}], \forall \mathbf{t}_1, \mathbf{t}_2 \in R^2. \tag{4.13}$$

We assume that $Q = \{Q_{\mathbf{t}} : \mathbf{t} \in R^2\}$ is a second-order process, that is $E[Q_{\mathbf{t}}^2] < \infty$. The random process is called wide-sense stationary if

1. the mean of the random process satisfies:

$$\mu_Q(t) = \mu_Q(\mathbf{t} + \mathbf{t}'), \forall \mathbf{t}, \mathbf{t}' \in R^2 \tag{4.14}$$

2. the autocorrelation function of the random process satisfies:

$$R_Q(\mathbf{t}_1, \mathbf{t}_2) = R_Q(\mathbf{t}_1 + \mathbf{t}', \mathbf{t}_2 + \mathbf{t}') = R_Q(\mathbf{t}_1 - \mathbf{t}_2, 0), \tag{4.15}$$

$\forall \mathbf{t}', \mathbf{t}_1, \mathbf{t}_2 \in \mathrm{R}^2$.

With an abuse of notation, we express:

$$R_Q(\mathbf{t}_1 - \mathbf{t}_2, 0) = R_Q(\mathbf{t}_1 - \mathbf{t}_2). \tag{4.16}$$

Alternately:

$$R_Q(\mathbf{t} + \boldsymbol{\tau}, \mathbf{t}) = R_Q(\boldsymbol{\tau}). \tag{4.17}$$

where $\boldsymbol{\tau} = [\tau_1 \ \tau_2]^T$.

For a wide-sense stationary random process $Q = \{Q_{\mathbf{t}} : \mathbf{t} \in R^2\}$ with autocorrelation function $R_Q(\tau)$ the power spectral density $S_Q(\Omega)$ is given by

$$S_Q(j\boldsymbol{\Omega}) = \int_{\mathbf{t} \in R^2} R_Q(\boldsymbol{\tau}) e^{-j\boldsymbol{\Omega}^T \boldsymbol{\tau}} d\boldsymbol{\tau}. \tag{4.18}$$

As before let R and Z denote the sets of real numbers and integers respectively. We consider a uniform photoreceptor cell density such that the cells are centered on a uniform grid or lattice defined by random rotation of vectors $\mathbf{v_1} = [v_{11} \ v_{12}]^T$ and $\mathbf{v_2} = [v_{21} \ v_{22}]^T$ where $\mathbf{v_k} \in R^2$ for $k = 1, 2$. In addition we consider a random shift by a random vector $\mathbf{U} = [U_1 \ U_2]^T$ that is uniform in the parallelogram $S_{\mathbf{V}}$ defined earlier. Now we model this randomly shifted pulse train as random process $Q = \{Q_{\mathbf{t}} : \mathbf{t} \in R^2\}$.

First we ignore the random shift and rotation and consider a deterministic rotation and zero shift as considered earlier. We note that the deterministic signal $x_c(\mathbf{t})$ in eqn. (4.2) is periodic

in $\mathbf{t}$. We can therefore express $x_c(\mathbf{t})$ as a 2D Fourier series. The Fourier series expansion is given by

$$\sum_{\mathbf{n}=Z^2} g(\mathbf{t}-\mathbf{V}\mathbf{n}) = \sum_{\mathbf{k}=Z^2} d_{\mathbf{k}} e^{j\mathbf{t}^T\overline{\mathbf{V}}\mathbf{k}}. \tag{4.19}$$

where

$$d_{\mathbf{k}} = \frac{1}{|\det \overline{\mathbf{V}}|}\int_{\mathbf{t}\in S_{\mathbf{V}}} g(\mathbf{t}) e^{-j\mathbf{t}^T\overline{\mathbf{V}}\mathbf{k}} d\mathbf{t}.$$

Now we define the random process $Q = \{Q_{\mathbf{t}} : \mathbf{t} \in R^2\}$ as a randomly shifted and rotated version of $x_c(\mathbf{t})$ as follows:

$$Q_{\mathbf{t}} = \sum_{\mathbf{n}=Z^2} g(\mathbf{t}-\mathbf{V}_{\boldsymbol{\Theta}}\mathbf{n}-\mathbf{U}). \tag{4.20}$$

where we rotate the original lattice by a random angle Θ that is uniform in $[0, 2\pi)$ to get a new lattice given by

$$\mathbf{V}_\Theta = \mathbf{R}_\Theta \mathbf{V}, \quad \mathbf{R}_\Theta = \begin{bmatrix} \cos\Theta & -\sin\Theta \\ \sin\Theta & \cos\Theta \end{bmatrix}. \tag{4.21}$$

Now using the Fourier series expansion, the random process can be expressed as:

$$Q_{\mathbf{t}} = \sum_{\mathbf{n}=Z^2} g(\mathbf{t}-\mathbf{V}_{\boldsymbol{\Theta}}\mathbf{n}-\mathbf{U}) = \sum_{\mathbf{k}=Z^2} d_{\mathbf{k}} e^{j(t-U)^T\overline{\mathbf{V}}_\Theta\mathbf{k}}. \tag{4.22}$$

It can be shown that the mean of the random process is a constant. We now examine the autocorrelation function. Now

$$R_Q(\mathbf{t}+\boldsymbol{\tau},\mathbf{t}) = E[Q_{\mathbf{t}+\boldsymbol{\tau}}Q^*_{\mathbf{t}}]. \tag{4.23}$$

Therefore

$$R_Q(\mathbf{t}+\boldsymbol{\tau},\mathbf{t}) = E[\sum_{\mathbf{k}\in Z^2}\sum_{\boldsymbol{\ell}\in Z^2} d_{\mathbf{k}}\, d^*_{\ell}\, e^{j(\mathbf{t}+\boldsymbol{\tau}-\mathbf{U})^T\overline{\mathbf{V}}_{\Theta}\mathbf{k}}\, e^{-j(\mathbf{t}-\mathbf{U})^T\overline{\mathbf{V}}_{\Theta}\boldsymbol{\ell}}]. \tag{4.24}$$

It follows that

$$R_Q(\mathbf{t}+\boldsymbol{\tau},\mathbf{t}) = \sum_{\mathbf{k}\in Z^2}\sum_{\boldsymbol{\ell}\in Z^2} d_{\mathbf{k}}\, d^*_{\boldsymbol{\ell}}\, E[e^{j(\mathbf{t}-\mathbf{U})^T\overline{\mathbf{V}}_{\Theta}(\mathbf{k}-\boldsymbol{\ell})}\, e^{-j\boldsymbol{\tau}^T{}_{\Theta}\mathbf{k}}]. \tag{4.25}$$

leading to

$$R_Q(\mathbf{t}+\boldsymbol{\tau},\mathbf{t}) = \sum_{\mathbf{k}\in Z^2} |d_{\mathbf{k}}|^2 E[e^{-j\boldsymbol{\tau}^T\overline{\mathbf{V}}_{\Theta}\mathbf{k}}] = R_Q(\boldsymbol{\tau}). \tag{4.26}$$

showing that the autocorrelation function is independent of $\mathbf{t}$. From Parseval's theorem and the fact that g is a square integrable it also follows that

$$E[|Q_{\mathbf{t}}|^2] = \sum_{\mathbf{k}\in Z^2} |d_{\mathbf{k}}|^2 < \infty. \tag{4.27}$$

establishing that the random process is second-order. It follows that the process is wide sense stationary. By examining the expression for the power spectral density $S_Q(j\mathbf{\Omega})$ we find that it is circularly symmetric agreeing with the conclusion of the deterministic analysis

4.4 Images

A computer-generated test image (351×351) that simulated the photoreceptor cell mosaic was created using Matlab software, following a methodology similar to the one outlined by Xue et al [5]. Simulated photoreceptor cells were generated using a *cos* function such that the cells were brightest in the center and the intensity gradually decreased outward (Figure 4.10, top left). Inter-cell spacing was 17 pixels. In order to introduce background variation, blur, and noise in the image, the test image was convolved with a point spread function and then Gaussian white noise (mean = 0 and variance = 0.0001) was added (Figure 4.10, top center). An AO retinal image was acquired as outlined previously [87].

4.5 Circularly symmetric band-pass filtering and image segmentation

Fourier analysis is done locally in the retinal image in block sizes of 50×50 since variability exists in the cell spacing across a single image. Overlapping blocks are used to avoid blocking artifacts at boundaries. The energy in concentric circular bands around the DC is calculated by using the sum of squares of the absolute value to determine the distribution of energy. For each block, the cut-off frequency parameters are obtained from analysis of the DSFT. The energy spectral density is obtained and used as input into a 1D Parks-McClellan impulse response prototype filter [1] which is converted into a 2D circularly symmetric filter. The stopbands remove high frequency noise as well as low frequency image variations. Once the

filter parameters have been determined for each sub-image, the sub-image is filtered. We choose a segmentation method which finds the regional maximas. This method works well as cells in the preprocessed image are brighter in their centers and have a gradual reduction in intensity moving from the center of the cell outwards, regardless of the variability of pulses corresponding to cells.

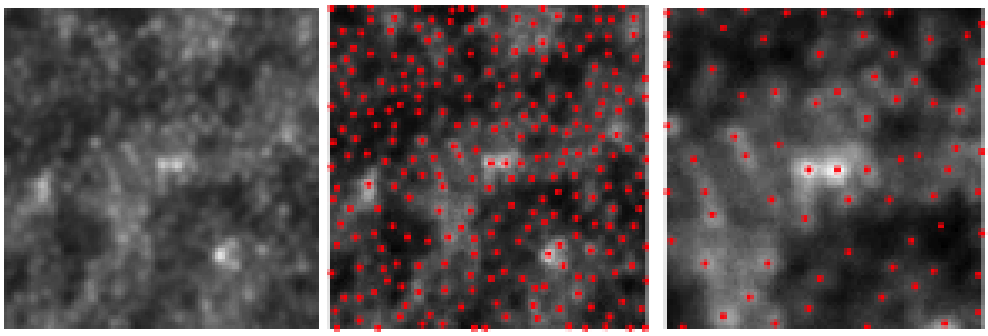

Figure 4.11. Left to right: sub-image cropped from original; estimation of cell location at scale = 1; estimation of cell location at scale=2

4.6 Results on test images and human retinal images

The proposed method was tested on a computer-generated test image and a human AO retinal image with variable simulated cell densities. The number of cells in the test image was known and was used as the gold standard. Figure 4.10 (top left) shows a computer-generated test image simulating photoreceptor cells arranged in a cone mosaic. The actual number of cells in the test image was 440. The number of cells counted by the L-CAF method was 450, yielding

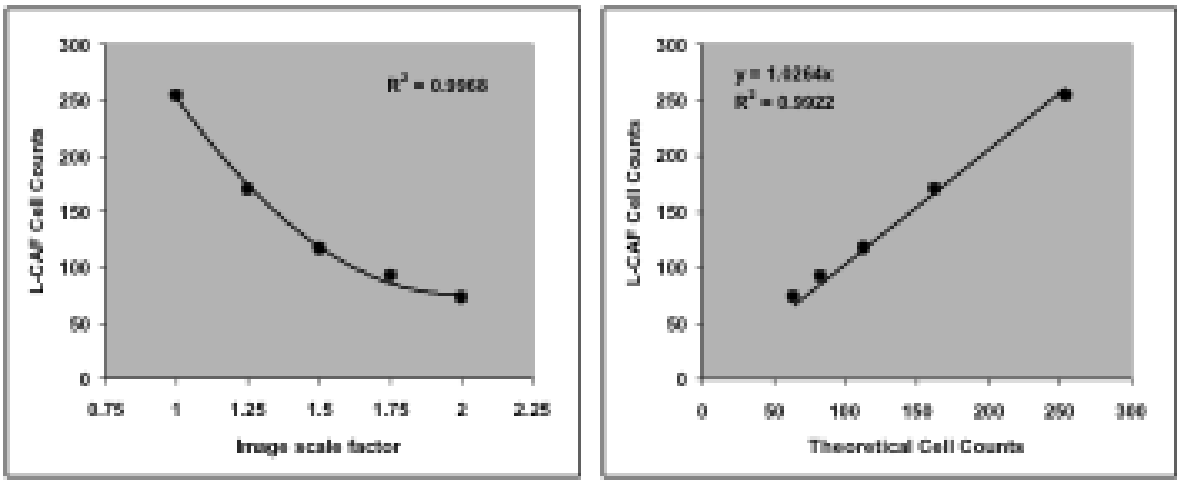

Figure 4.12. Left: Correlation between image scale factor and cell count. Right: Correlation between theoretical cell count and obtained cell count.

a percent difference of 2%. For the human retinal images, a 171×171 cropped portion of the original human AO retinal image is shown in Figure 4.11 (left). The center and right images of Figure 4.11 show the position of detected cells superimposed in the AO retinal images with scale factors of 1 and 2, respectively. The number of cells counted by L-CAF on the AO retinal image (Figure 4.11, left) was 254. Two observers manually counted 265 and 277 cells, yielding a mean manual count of 271. The percent difference in the cell count between manual and L-CAF was 6%. The number of cells detected by L-CAF in AO retinal images with variable scaling was determined. The relationship between the number of cells counted by L-CAF and image scale factor is shown in the left-hand-side figure of Figure 4.12. As expected, the data points fit a quadratic function with a correlation coefficient of 0.99. The number of cell counts expected theoretically based upon the scale factor (theoretical cell counts) was estimated as the number

of cells counted by L-CAF at scale 1 divided by the square of scale factors for all images. The relationship between L-CAF and theoretical cell counts is shown in the right figure of Figure 4.12. The best fit line to the data points had a slope of 1.03 and a correlation coefficient of 0.99, indicating excellent agreement between L-CAF and the theoretical cell counts.

4.7 Discussion and conclusion

We develop a frequency-based image analysis method for quantification of cell density and apply it to computer-generated test images and human retinal images. A circularly symmetric band-pass filter is designed using parameters that are determined from the local energy distribution within the discrete time Fourier transformed image. This allows the filter to enhance the image using localized information as opposed to approximating results by averaging over the entire image. Undesirable ripple effects and boundary transitions are avoided by using extra samples from neighboring boundary pixels. Comparison of automated cell counts with actual and manual counts on test and retinal images demonstrates the accuracy of the method. The accuracy is further established by showing a high correlation between automated cell counts and AO retinal image scale factors. The proposed method can be used to assess loss of photoreceptor cells and other biological cells due to disease.

CHAPTER 5

SEGMENTATION AND ANALYSIS OF PATHOLOGIES IN RETINAL IMAGES

It is important for clinicians to better understand the underlying causes of disease so that the appropriate treatment plan can be followed for those who are at risk for vision loss. This requires the detailed analysis of large volumes of retinal images. Hardware advances that can capture the diminutive details in biological tissues as well as the improvement in computational power in digital systems have provided the basis for researchers to apply pattern recognition and image analysis in medical and biological applications. This can pave the way for improvement in eye health care in general as it provides the potential to help better understand disease processes thereby facilitating diagnosis and treatment plans [89].

Numerous algorithms have been developed to analyze retinal images for the classification of normal and abnormal eyes. Image segmentation has been a significant topic in image processing for the last several decades and it is a very important problem in the field of image processing and computer vision. The objective of segmentation is to separate an object or objects of interest from each other as well as from their backgrounds in order to analyze the features of the object or objects using qualitative and quantitative measures. The application areas of image segmentation are numerous, ranging from pathology segmentation in medical images to the segmentation of geographical structures in satellite images [90–94]. The correct segmentation of structures, especially in medical images, is crucial for abnormality detection, progression,

and treatment [95]. The quality of medical images is generally challenged by noise introduced during the acquisition process; missing or broken boundaries; and complex biological structures. In such cases, the segmentation of structures can be facilitated by the introduction of prior information, such as an approximation of the shape, intensity, and other features of the tissue of interest, that could improve the performance of the segmentation algorithm. The level-set method is an effective method that can be used for image segmentation as it follows the evolution of interfaces, such as when regions break or merge together. Recently, level-set based approaches that integrate shape priors using different shape models have been proposed. These approaches either use specific shapes known *a priori* or the shape parameters are obtained from available training data [68, 70, 71, 75, 77, 78]. We explore both level-set approaches (with and without priors) by developing algorithms that can segment pathologies in fluorescein angiograms and en face images of patients with diabetic retinopathy (DR) and age-related macular degeneration (AMD).

5.1 Level-sets for image segmentation

The automated detection of lesions caused by retinal diseases such as DR and AMD is essential for early diagnosis and subsequent disease monitoring [96]. Additionally, analysis of retinal images of patients before and after treatment can provide insight into the efficacy of the treatment. It is of considerable importance to develop techniques that will aid in the uncovering of anatomic structures that will lead to the subsequent characterization of the normal or diseased states that may occur in the retina [97]. An increase in the sophistication of imaging and computing systems has made medical image acquisition and analysis more feasible

[98]. The use of active contour models for image segmentation has gained extensive popularity. The fundamental concept of active contours is to evolve an initial curve towards the boundaries of the object of interest. The curve is evolved iteratively using a combination of forces which are determined by the geometry of the changing curve as well as the local properties of the image. Image segmentation problems using active contours are usually based on minimizing functions such that curves close to the region boundaries are minimized and therefore have small values. Partial differential equations are usually employed to solve minimization of these functionals and hence the problem can tend to be computationally expensive. Level-sets are one example of an active contour [94]. Level-set methods have been used for tracking interfaces and for image segmentation. One of the main advantages of level-sets are that they are able to represent objects which have complex topologies and they are able to model the changes of these topologies, such as when two object merge or split in a natural way. In the field of image segmentation, level-set methods are classified into region-based models and edge-based models. Edge-based models use an edge detector which depends on the gradient of the image to stop the curve on the object boundaries. Region-based models assume intensity homogeneity and are not as sensitive to the location of initial contours as they do not use the image gradient for segmentation. The Chan-Vese model [2] is one of the classical region-based active contour models which utilizes level-sets [66, 67, 79, 94, 99]. A serious drawback of existing level-set algorithms is that the final result is highly dependent on the location of initialization as the level-set evolution depends on the forces computed from local image data. We study the segmentation of pathology in fluorescein angiograms of patients with retinal disease by

using the Chan-Vese model [2] with automatic determination of the initial contour. By finding sudden rises and declines in intensity, we can estimate the starting and stopping edges of the pathology and enclose the pathology within the initial contour. The result is faster convergence and improved accuracy in the segmentation.

5.1.1 Chan-Vese level set model [2]

The popular Chan-Vese level set model [2] proposes the following cost function which consists of four terms; the first and fourth terms are smoothing terms which cause the contour to be smooth and the second and third terms push the contour towards a balanced position [70]:

$$\begin{aligned} E(c_1, c_2, \phi) &= \mu L(\phi) + E_{out}(c_1, c_2, \phi) \\ &= \mu \int \delta(\phi) \mid \nabla\phi \mid dxdy + v \int H(\phi)dxdy \\ +(\int (I - c_1)^2 H(\phi)dxdy &+ \int (I - c_2)^2 (1 - H(\phi))dxdy). \end{aligned} \tag{5.1}$$

Here, $\mu \geq 0$ is a fixed parameter; ϕ is the level-set function, $L(\phi)$ is the length of the curve; c_1 and c_2 are the respective mean intensities inside and outside the contour and are solved as follows

$$\begin{aligned} c_1(\phi) &= \frac{\int\limits_{\Omega} I(x) \cdot H(\phi)dx}{\int\limits_{\Omega} H(\phi)dx} \\ c_2(\phi) &= \frac{\int\limits_{\Omega} I(x) \cdot (1 - H(\phi))dx}{\int\limits_{\Omega} (1 - H(\phi))dx}. \end{aligned} \tag{5.2}$$

Where $H(\phi)$ is the Heaviside function defined by

$$H(z) = \begin{cases} 1, if z \geq 0 \\ 0, if z < 0 \end{cases} \tag{5.3}$$

$H(\phi)$ and $\delta(\phi)$ are the one-dimensional Heaviside and Dirac delta function respectively and I is the original image to be segmented. $L(\phi)$ denotes the internal energy which controls the smoothness of the curve and $E(c_1, c_2, \phi)$ is the external energy which is driven by image features and forces the contour towards object boundaries. The Chan-Vese model [2] assumes intensity homogeneity and seeks to partition the image into regions of constant mean intensity. This often leads to poor segmentation results in complicated images. Additionally, the Chan-Vese model [2] is dependent on the placement of the initial contour, yielding different results for different initial locations of the contour [100].

5.2 Images

En face imaging of the retina is a novel approach to observe the ISOS layer. The images are generated by performing high density SDOCT imaging with 145 B-scans over a $15^\circ \times 15^\circ$ retinal area using a commercial instrument (Spectralis, Heidelberg Engineering) as previously described in [33]. En face images are flat layers taken at a set distance from the retinal pigment epithelium(RPE). As the anatomical layers are not flat, the methodology described in [33] was applied to generate en face images of 7 retinal layers that approximately coincided with the anatomical location of the layers of interest. The desired layers are automatically segmented and the data stored in consecutive rows of the en face image. The retinal layers in a healthy

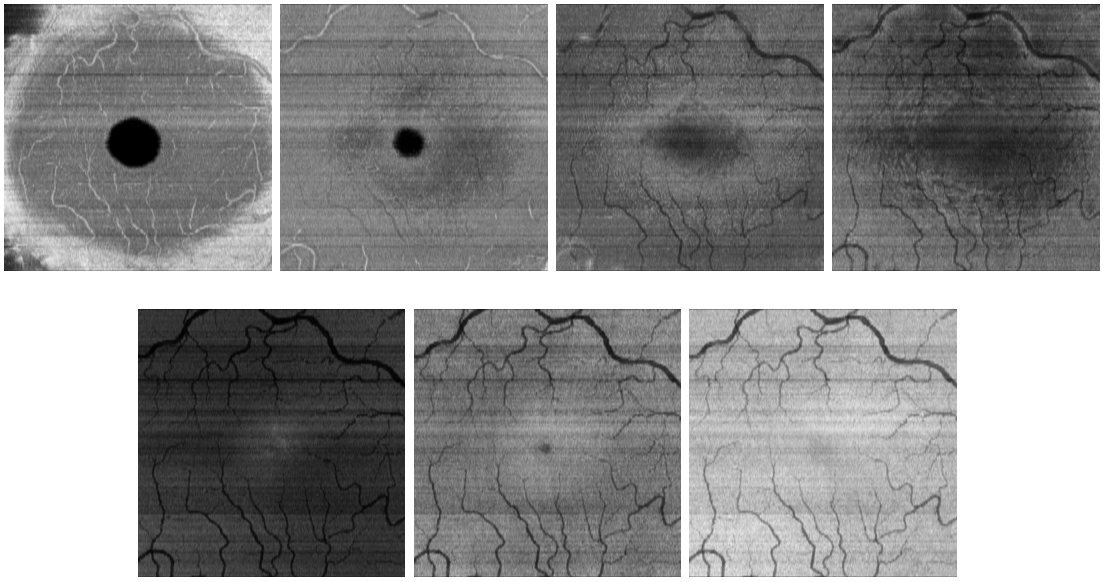

Figure 5.1. En face images for a subject with normal eyes. The layers are as follows: Top column left to right: NFL, IPL, INL, OPL. Bottom column, left to right: ONL, ISOS, and RPE.

human as shown in Figure 5.1 eye appear in the following order: nerve fiber layer (NFL), inner plexiform layer (IPL), inner nuclear layer (INL), outer plexiform layer (OPL), outer nuclear layer (ONL), inner segment/outer segment (ISOS) layer, and the retinal pigment epithelium (RPE) layer.

5.3 Proposed methodology

The initialization of the level-set zero contour can greatly affect the outcome of the segmentation result. In the case of the classical Chan-Vese model [2], random placement of the initial contour can cause it to become trapped in a local minimum. In such a case the contour may not be able to extend to other contours. The approach we have used here is one of analysis

in the spatial domain. Using *a priori* knowledge about the characteristics of the lesions, we attempt to estimate the locations of the lesions thereby discarding all other irrelevant information. In this way the size of the feature space is greatly reduced. In our work, we propose using the intensity distribution of the lesions in the images to aid in the detection process. Fluorescein angiograms are used for clinical assessment of subjects with retinal diseases and provide visualization of pathologies which appear brighter than the surrounding normal areas. The distribution of intensities in the background as well as in the foreground is relatively homogeneous. We exploit this to project image intensity profiles along two non-parallel directions. In particular, we choose the projection profiles in the vertical and the horizontal directions to estimate lesion boundaries. The projection profile is a summation of the intensities along each row and each column and yields a row and column vector. The vectors contain large entries when there is a sudden rise in intensity and small entries when there is a sudden drop in intensity. As the image backgrounds are mostly uniform, the appearance of a lesion will show up very clearly as either a sudden large peak or valley in the case when it is a light lesion or a dark lesion respectively. The onset or leading edge of a peak or valley demarcates the start of the boundary of the lesion. The offset or the lagging edge of the peak or valley specifies the end of the boundary of the lesion. By determining the location of these peaks we can estimate the approximate size and location of the lesion in the image. The detected lesion can then be bounded by the initial contour thus reducing the time and number of iterations for convergence as the initial contour can expect to be in proximity to the lesion boundaries. We can also automatically adapt parameters varied to detect either large objects or small objects.

The images were not preprocessed with any filters. As the original size of the image is very large (2048×2076), we cropped an initial part of the image which contained the pathology as well as a large portion of the background. The size of the cropped image varied from 300×300 pixels to 500×500 pixels. We have compared our method to the classical Chan-Vese method in which the initial contour can be placed anywhere in the image [2]. Our results show that the segmentation is effective in separating the lesion from its background. The reduced number of iterations for the proposed method indicates that the speed of convergence is improved.

5.4 Results

The proposed method was applied to 3 fluorescein angiogram images that were cropped to better display pathological lesions. We note that the method can be applied to any size image. Figure 5.2 shows the results of image segmentation by our method and the Chan-Vese method [2]. It can be seen that the position of the initial contour does indeed affect the outcome of the segmentation. As the initial contour is well-placed near the detected pathology, the number of iterations for the given images was as low as 25. With our method, the number of iterations (between 25 and 193) was considerably lower than the number of iterations (between 300 and 700) needed using the Chan-Vese method [2]. Furthermore, the areas of pathology were better segmented by our method, with a better exclusion of areas adjacent to the lesion (left-most and right-most figures of Figure 5.2). Segmentation of the background rather than the foreground occurs when the contour becomes trapped in a region of local minima. The accuracy of our method can be further improved by applying our segmentation method to images that have been pre-processed to remove the blood vessels. Our image segmentation

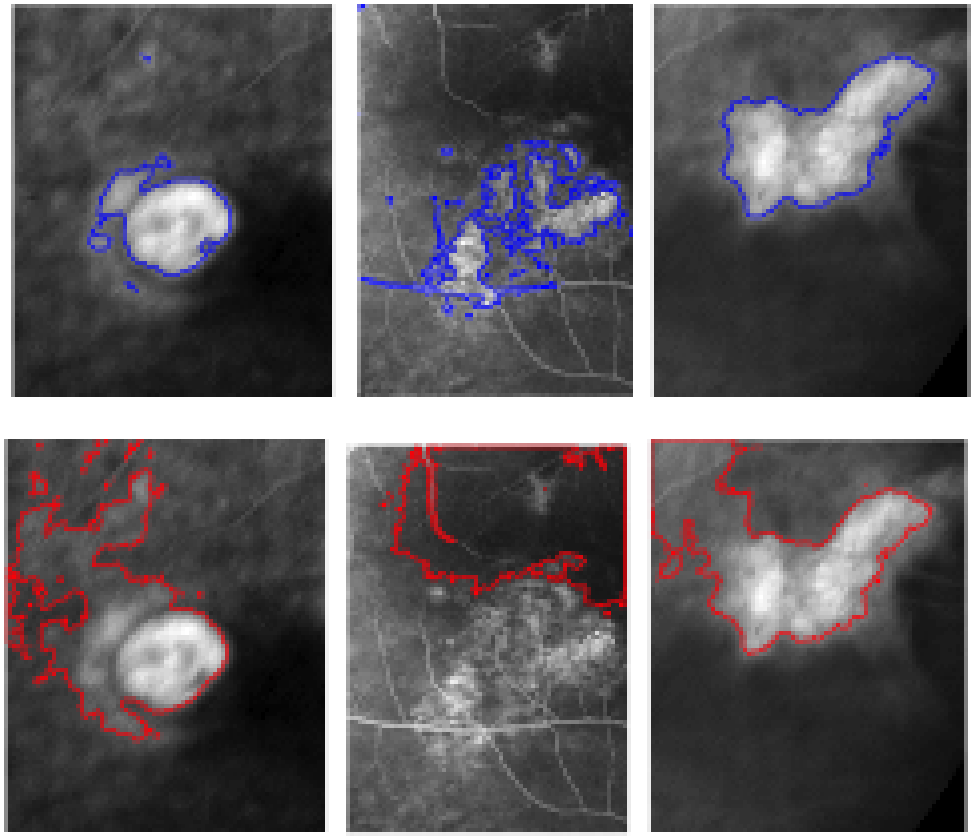

Figure 5.2. Segmentation results of our method (top row) versus classical Chan-Vese method [2] (bottom row).

method can be applied to monitor changes in pathologies over time due to disease progression and/or therapeutic intervention. A variety of quantitative features such as the mean intensity and area of the lesions can be extracted for detecting changes that may be potentially important for clinical management of patients.

5.5 Fourier descriptor based level-set segmentation for en face retinal images

Upon analysis of the single inner-segment/outer-segment (ISOS) junction layer, we found it necessary to analyze en face images of the the remaining retinal layers in order to observe the morphological changes the disease takes as it traverses through the layers. It is of interest to determine whether pathologies in the inner retina can cause optical effects, such as shadowing, on layers in the outer retina, making it appear as though the integrity of the outer retinal layers has been compromised. By including multiple layers in our study, we are able to provide insight as to how abnormalities in the upper layer of the retina are represented in the ISOS layer. Of specific interest is the relationship between pathologies in the inner plexiform layer (IPL) and the ISOS layer in patients with diabetic retinopathy.

Diabetic retinopathy (DR) is a progressive disease in which weakened blood vessels cause the leakage of blood into the retina, leading to drastic visual impairment in the elderly. The detection and segmentation of pathologies in retinal images with DR are therefore important in providing a better understanding of disease processes and their temporal evolution, thereby facilitating diagnosis and treatment plans. Understanding the origins of the pathology can enable clinicians to determine whether the damage caused by disease is optical or neural in nature. In the case of optical pathologies, the source of the pathology lies in a layer above the ISOS layer and gives rise to optical effects on the ISOS junction such that it appears to have disrupted photoreceptor integrity. Treatment of these pathologies restores the high reflectivity of the ISOS layer. Neural pathologies on the other hand occur directly on the ISOS layer and indicate irreversible photoreceptor cell death. In this study, we address the problem of

determining the nature of the pathology by segmenting the en face images in a layer-by-layer fashion for seven layers of the retina.

We propose a level-set segmentation model that utilizes the Fourier coefficients of a polygonal curve obtained from actual pathologies visible in the en face retinal images to represent shape priors which guide the curve evolution process. The work we are proposing has a flavor that is similar to the work proposed by Charmi et al [86], with several major differences. Charmi et al [86] use Fourier descriptors for shape alignment to represent objects for shape recognition. In our work however we use the Fourier coefficients of a polygonal curve obtained from actual pathologies visible in the en face retinal images to represent shape priors which guide the curve evolution process. A sample pathology image is computed from a number of actual pathology images by averaging the Fourier transforms of the images. A polygonal curve is obtained from this averaged image and is used as the target shape during the segmentation process. We also use a subset of the low-order coefficients of the Fourier descriptors which works two-fold. Firstly, it reduces the amount of computation required as the full set of coefficients are not being used and secondly it automatically introduces some degree of smoothness as the lower order coefficients contain basic structural information and the higher order coefficients contain high frequency information. The novelty of Charmi's method [86] method lies on the definition of a Fourier-based alignment energy function based on curvature to measure the shape similarity between a target curve and an evolving curve. The contribution of our work therefore provides two aspects of novelty. Firstly, to our knowledge, no other group has attempted to differentiate between optical and neural pathologies in en face layers of the retina. Secondly, we use a level-

set method with evolving level-set function that adapts itself to the layer on which it is being applied. We focus our study on the description of shape priors using Fourier descriptors to simulate pathologies occurring in the human retina. The shape signatures are derived using the centroid distance function. We obtain and observe the segmentation of pathologies visible in en face images generated for seven layers of the retina and attempt to analyze the progression or recession of disease as the pathologies grow or shrink across the layers. We compare our results with the well-known distance regularized method developed by Li et al [9] to emphasize the difference in segmentation results and convergence time with and without shaper priors. Results obtained allow us to observe the form the disease takes across layers and allows us to speculate about the presence of an optical or neural pathology.

5.6 Details of Fourier-descriptor based method

Our model consists of three basic steps. The first step in the segmentation and analysis of en face images is the removal of noisy artifacts which have been acquired during the acquisition process. The next step is to define shape descriptors to be embedded in the level set formulation. Once the shape descriptors have been defined, they are included in the level set equation to segment objects of similar shape. During each iteration, a cost function is calculated to determine the degree of similarity between the target shape and the shape being segmented. Finally, we apply morphological post-processing to remove small, unwanted artifacts and spurious pixels.

5.6.1 Preprocessing

The generated images suffer from many artifacts introduced during the acquisition process. As the layers are segmented from B-scans and then stored in consecutive rows in the en face

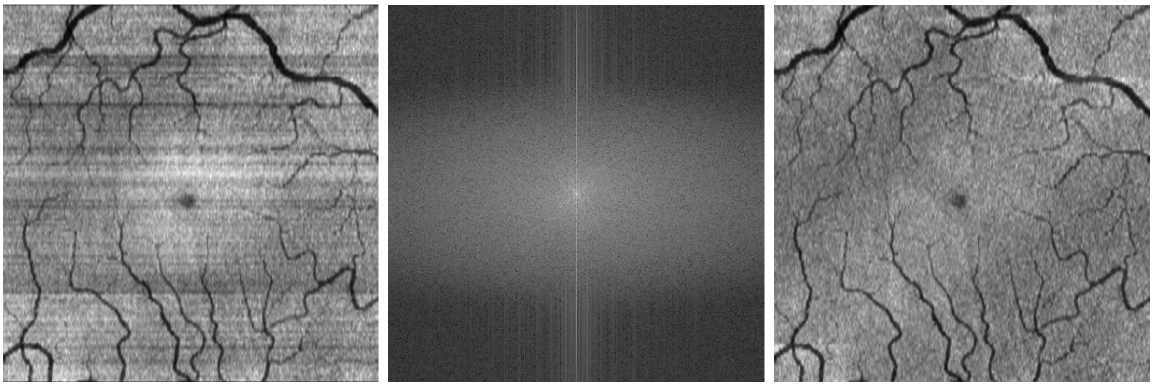

Figure 5.3. ISOS en face image of a healthy subject. Left: Before preprocessing Center: Fourier transform of original image Right: After preprocessing, horizontal lines removed.

image, dark horizontal lines can be seen all across the image. These artifacts can be better removed in the frequency domain. The vertical lines visible in the Fourier transformed image of Figure 5.3 correspond to the horizontal lines in the spatial domain image. By removing these lines in the Fourier domain we can obtain an image which appears much cleaner whilst retaining necessary spatial information.

5.7 Theory of polygonal curve Fourier descriptors

Shape is one of the low level features used in many image processing and computer vision applications. The use of shape priors facilitates the segmentation process if one knows an estimated outline of the object of interest. Fourier descriptors provide a frequency based description of the boundary of 2D objects in images. In our model, we define polygonal curve Fourier descriptors (FD) to be used as contours for the expected shape of the pathology [101]. Shape features can be well represented by FD, which can be easily derived and compactly

characterized. We will now delve into the theoretical details of shape priors defined by Fourier descriptors.

5.7.1 Background on Fourier descriptors

Suppose we are given a simple closed continuous curve γ, which is clockwise oriented and has the parametric representation $(x(l), y(l)) = Z(l)$, and $0 \leq l \leq L$ where L is arc length. We can denote the angular direction of γ at point l by a function $\theta(l)$ and let $\delta_0 = \theta(0)$ be the absolute angular direction at the starting point $Z(0)$. The cumulative angular frequency $\phi(l)$ is defined as the net amount of angular bend between the starting point and the point l. Therefore, $\phi(0) = 0$ and $\theta(l) = \phi(l) + \delta_0$, except for a possible multiple of 2π. It should be noted that $\phi(L) = -2\pi$ and as a result does not contain any shape information. The domain $[0, L]$ of $\phi(l)$ contains size information and can be normalized to the interval $[0, 2\pi]$, which is standard for periodic functions. Hence a normalized variant, $\phi^*(t)$, can be defined with domain $[0, 2\pi]$ and such that $\phi^*(0) = \phi^*(2\pi) = 0$. Therefore we now have

$$\phi^*(t) = \phi(\frac{Lt}{2\pi}) + t. \tag{5.4}$$

This simply implies that all closed curves can be mapped to the class of periodic functions with domain $[0, 2\pi]$, such that all curves with identical shape go into the same class of ϕ^*. Two

curves are said to be identical if they differ only in translation, scale, and rotation. If ϕ^* is expanded as a Fourier series, then

$$\phi^*(t) = \mu_0 + \sum_{k=1}^{\infty}(a_k \cos kt + b_k \sin kt). \tag{5.5}$$

In polar form, the expansion is given by

$$\phi^*(t) = \mu_0 + \sum_{k=1}^{\infty} A_k \cos(kt - \alpha_k). \tag{5.6}$$

where (A_k, α_k) are the polar coordinates of (a_k, b_k) and are the Fourier descriptors for the curve γ and are known as the k^{th} harmonic amplitude and phase angle, respectively. Now if we consider that γ is a discrete polygonal curve, we can obtain the Fourier coefficients $\{a_k, b_k\}$ for the curve. Assuming that the curve γ has m vertices, $V_0, ...V_{m-1}$, and that the edge, (V_{i-1}, V_i) has length Δl_i. The change in angular direction at vertex V_i is $\Delta\phi_i$ and $L = \sum_{t-1}^{m} \Delta l_1$. It can be verified that $\phi(l) = \sum_{i-1}^{k} \Delta\phi_i$ and $\phi(l) = 0$ for $0 \leq l \leq l_1$. By expanding ϕ^* we get

$$\phi^*(t) = \mu_0 + \sum_{n=1}^{\infty}(a_n \cos(nt) + b_n \sin(nt)), \tag{5.7}$$

where

$$\mu_0 = \frac{1}{2\pi}\int_0^{2\pi} \phi^*(t)dt \tag{5.8}$$

and

$$a_n = \frac{1}{\pi}\int_0^{2\pi} \phi^*(t)\cos(nt)dt, \qquad (5.9)$$
$$b_n = \frac{1}{\pi}\int_0^{2\pi} \phi^*(t)\sin(nt)dt.$$

Remembering that, $\phi^*(t) = \phi(\frac{Lt}{2\pi}) + t$ and making the change of variable $\gamma = \frac{Lt}{2\pi}$ we get:

$$a_n = \frac{2}{L}\int_0^{L} (\phi(\lambda) + \frac{2\pi\lambda}{L})cos(\frac{2\pi n\lambda}{L})d\lambda,$$
$$b_n = \frac{2}{L}\int_0^{L} (\phi(\lambda) + \frac{2\pi\lambda}{L})sin(\frac{2\pi n\lambda}{L})d\lambda. \qquad (5.10)$$

Recalling that $\phi(l)$ is a step function in tangent space represented by edge lengths and vertex bends, the following can be obtained:

$$a_n = \frac{-1}{n\pi}\sum_{k=1}^{m} \Delta\phi_k sin\frac{2\pi n l_k}{L}$$

$$b_n = \frac{-1}{n\pi}\sum_{k=1}^{m} \Delta\phi_k cos\frac{2\pi n l_k}{L}, \qquad (5.11)$$

where $l_k = \sum_{i=1}^{k} \Delta l_i$ The final forms of expression for a_n and b_n are attractive due to their similarity and due to the fact that because $\Delta\phi_k$ represents the bend in the curve's direction at the k^{th} polygonal vertex where l_k is the arc length from the starting vertex to the k^{th} vertex. In addition, it can be seen that the Fourier coefficients (a_n, b_n) contain no information regarding position or orientation of the curve. There are many useful relationships which link

the algebraic properties of the Fourier descriptors of a curve to the geometric properties of the shape bounded by the curve. In addition, a principle reason for the use of Fourier descriptors is the invariance of harmonic amplitudes under translations, rotations, changes in size, and shifts in the starting point.

5.7.2 Implementation of Fourier descriptors for shape prior modeling

In this section we will discuss the implementation details of obtaining the Fourier descriptors for a polygonal curve. Suppose the discrete boundary of an object S, whose boundary is defined by a closed curve C is plotted on the XY plane. If we traverse the boundary of the object by starting at an arbitrary point (x_0, y_0), the coordinate pairs that will be encountered as we are tracing the boundary path are $(x_1, y_1), (x_2, y_2), ..., (x_{N-1}, y_{N-1})$. We can express these coordinate pairs as $x(k) = x_k$ and $y(k) = y_k$. The *shape signature* of the boundary itself can therefore be represented as the sequence of coordinates $s(k) = [x(k), y(k)]$, for $k = 0, 1, 2, ..., N-1$. An obvious advantage of such a representation is that it reduces a 2D problem to a 1D problem. The discrete Fourier transform (DFT) of $s(k)$ is

$$a(u) = \frac{1}{N} \sum_{k=0}^{N-1} s(k) e^{(\frac{-j2\pi uk}{N})}, \tag{5.12}$$

for $u = 0, 1, 2, ..., N-1$. The complex coefficients of $a(u)$ are called the Fourier descriptors of the boundary. The inverse Fourier transform of $a(u)$ restores $s(k)$, i.e.,

$$s(k) = \sum_{u=0}^{N-1} a(u) e^{(\frac{j2\pi uk}{N})}, \tag{5.13}$$

for $k = 0, 1, 2, ..., N-1$. We use the centroid distance function in order to obtain the coefficients of the shape signature, as it has been shown that shape representation using the centroid function is significantly better than using other techniques, such as complex coordinates and curvature signature [102]. The centroid distance function is given by the distance of the boundary points from the centroid (x_c, y_c) of the shape:

$$r(t) = ([x(t) - x_c]^2 + [y(t) - y_c]^2)^{\frac{1}{2}}, t = 0, 1, ..., N-1$$

$$x_c = \frac{1}{N} \sum_{t=0}^{N-1} x(t)$$

$$y_c = \frac{1}{N} \sum_{t=0}^{N-1} y(t). \tag{5.14}$$

The 1D Fourier transform is then applied to $r(t)$ to obtain the Fourier transformed coefficients. The FD method uses a series of circles with different sizes and frequencies to build a 2D plot of a boundary, where each descriptor coefficient is the frequency representation of a circle in the 2D XY plane. An advantage of using FD's for boundary representation is that the FD's are rotation, scale, and translation invariant. Translation has no effect on the descriptors except at the position where $k = 0$, which has the impulse function $\delta(k)$. The inverse DFT of this descriptor is equivalent to the centroid of the object. Translation invariance is easily achieved by setting $k(0) = 0$, and translating the origin of the coordinate system to the center of mass of the pattern [103].

Rotation invariance can be achieved by ignoring the phase information of $a(u_0)$ and using only the absolute value or magnitude of $|a(u_0)|$ at each descriptor. Scale invariance is achieved by dividing $|a(u_0)|$ by the DC component. In order to measure the similarity between a target shape T and a query Q, the Euclidean distance between the Fourier descriptor representations of the two shapes is measured [104] . The derived coefficients represent the approximate shape of the pathology and are utilized as the shape prior to guide curve evolution. In order to extract the FD of the desired shape prior, the 1D Fourier transform must be applied to the centroid distance function, $r(t)$ as follows:

$$a_n = \frac{1}{N}\sum_{t=0}^{N-1} r(t)e^{\frac{-j2\pi nt}{N}} n = 0, 1, ..., N-1. \tag{5.15}$$

All the Fourier transformed coefficients are standardized by the first Fourier transformed coefficient a_0. The phase information is ignored and the coefficient magnitudes are retained. In order to denote the Fourier transformed coefficients that have been normalized and whose phase information is ignored we calculate $b_n = |\frac{a_n}{a_0}|$ where b_n is invariant to rotation, translation, scaling, and change of starting point [94]. A comparison of the descriptors of different objects provides a measurement of their similarity. The pathologies observed tend to take on circular or elliptical shapes with non-smooth boundaries. For our work, we obtain the target pathology shape by averaging over several pathology shapes in the frequency domain The 1D Fourier descriptors are then obtained from the 2D target shape and are used to compare the FD's of the test object which is being segmented.

In order to overcome some of the limitations of existing models, we propose a shape-based model which uses image features as part of the energy functional in order to drive the contour towards features possessing a desired characteristic. For the first image in our seven layer sequence we embed the FD of the target shape prior as the initial contour into the level-set equation. The final level set function of a given layer is used as the initial mask for each subsequent image in the sequence. In this way the function evolves across layers and this overcomes the problems of initial contour placement, as the pathologies in each layer tend to be localized. Shape energy E_{shape} given in Equation 5.16 encodes the shape information of the object represented by the shape prior and is incorporated into the region energy to guide curve evolution. A cost function is included which minimizes the difference between the descriptors of the test image and updated ϕ image. Therefore, we define our level set model as:

$$E_{img} = E_{shape} + E_{region} + E_{cost} \tag{5.16}$$

or more specifically:

$$\begin{aligned} E_{img}(\phi, c_1, c_2) = -\frac{1}{\pi}\frac{\varepsilon}{\varepsilon^2 + \phi^2} \cdot \mu \cdot (\frac{\nabla\phi}{\mid \nabla\phi \mid}) \\ + \int H(\widetilde{\mathbf{S}})dxdy + \lambda_1 \int (u_0 - c_1)^2 H(\widetilde{\mathbf{S}})dxdy \\ +\lambda_2 \int (u_0 - c_2)^2 (1 - H(\widetilde{\mathbf{S}}))dxdy + (\mid\mid \mid\widetilde{\mathbf{S}}_\mathbf{1}\mid - \mid\widetilde{\mathbf{S}}_\mathbf{2}\mid \mid\mid)^2, \end{aligned} \tag{5.17}$$

where c_1 and c_2 are the respective mean intensities inside and outside the contour, $\frac{1}{\pi}\frac{\varepsilon}{\varepsilon^2+\phi^2}$ is the "expanded" Dirac delta function, $\widetilde{\mathbf{S}}$ is the contour as defined by the Fourier descriptor of

the pathology, and $H(\widetilde{\mathbf{S}})$ is the Heaviside function applied to $\widetilde{\mathbf{S}}$. $(||\ |\widetilde{\mathbf{S}}_{\mathbf{1}}| - |\widetilde{\mathbf{S}}_{\mathbf{2}}|\ ||)^2$ is the cost function used to determine the degree of similarity between the target curve and exciting curve. The curve energy controls the elasticity and rigidity of the contour whereas the external energy attracts the contour towards object boundaries.

5.8 Results

We applied our method to en face images of 7 layers of the retina. Figure 5.4 show the pathologies as detected by our algorithm. The removal of the horizontal lines in the frequency domain aids in the segmentation process and allows for a much cleaner representation of irregularities in the image. Both light and dark irregularly shaped pathologies can be detected, regardless of size, shape, and orientation. The results shown in Figure 5.4 show segmentation of predominantly bright regions in the IPL layer which represent hard exudates and dark regions in the ISOS layer. It can be observed how the pathology sizes and shapes are transformed across layers. The centroids and areas of the pathologies in the IPL and ISOS layers are estimated in order to determine the extent of co-localization of pathologies present in these two layers. In the en face image of the IPL layer, three prominent objects are detected and these objects are reflected in the ISOS layer. Figure 5.5 shows the respective centroids marked for the IPL (blue dots) and the ISOS (yellow dots) en face images. Shown in Table I are the estimated areas and centroids of the detected pathologies in the IPL and ISOS en face images. We refer to the three detected pathologies as the left(L), center (C), and right (R) pathologies in Table I. The proximity of the centroids of the pathologies across the IPL and ISOS images suggests high co-localization and indicates an optical pathology, in which the prominent irregularities

in the IPL image are being reflected possibly as shadows in the ISOS layer. The difference in areas of pathologies may be due to a "smearing" of the shadows of the pathologies as viewed through multiple layers. We also compare our results with results generated from the distance-regularized level-set evolution method by Li et al [9] in order to emphasize the complications which may arise when using a manually defined contour as opposed to embedding shape priors into the contour. In the left-side figure of Figure 5.6, the contour encloses two objects as one rather than splitting to detect three larger pathologies and several smaller ones. Similarly for the right-side figure in Figure 5.6, the results shown in the ISOS layer depict a single pathology being segmented rather than the multiple pathologies which are clearly visible.

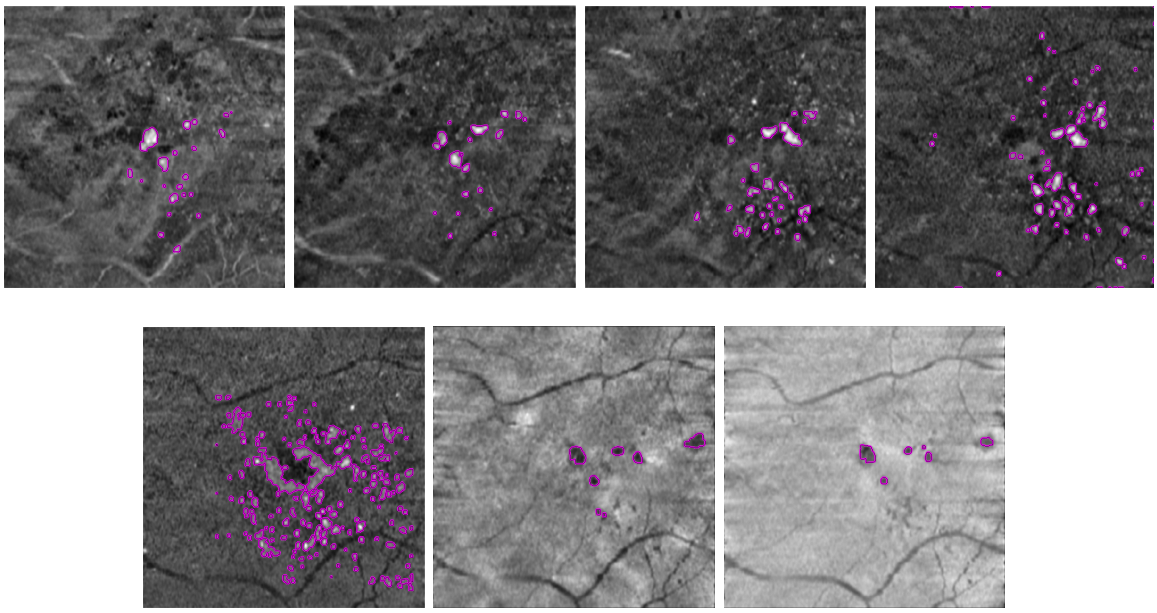

Figure 5.4. Pathologies segmented in en face images of 7 layers. Top row left to right: NFL, IPL, INL, OPL. Bottom row left to right: ONL, ISOS, and RPE.

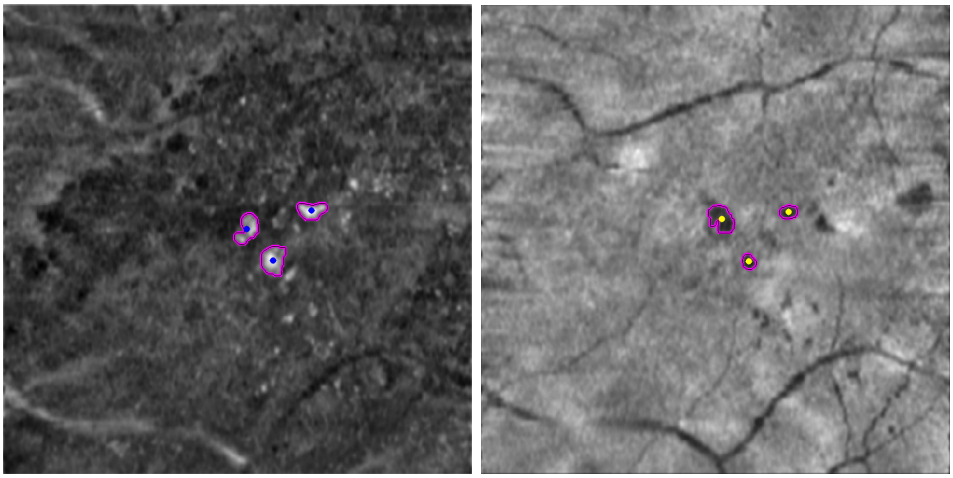

Figure 5.5. Centroids of pathologies marked on the IPL and ISOS layers of Patient 1.

Image	Area (L)	Area (C)	Area (R)	Centroid (L)	Centroid (C)	Centroid (R)
IPL	1241	1548	1081	[400, 367]	[443, 418]	[505, 337]
ISOS	1431	477	546	[395, 352]	[439, 421]	[504, 340]

TABLE I. PATHOLOGY AREAS AND CENTROIDS ESTIMATED FOR IPL AND ISOS LAYERS SHOWN IN Figure 5.5

5.9 Conclusion and discussion

Diabetic retinopathy is a disease which must be monitored closely in order to determine the pathological changes which are taking shape in the underlying layers of the retina. We develop an improved level-set method with automated initial contour specification. The method takes into account the relative background and foreground uniformity to detect abrupt changes in

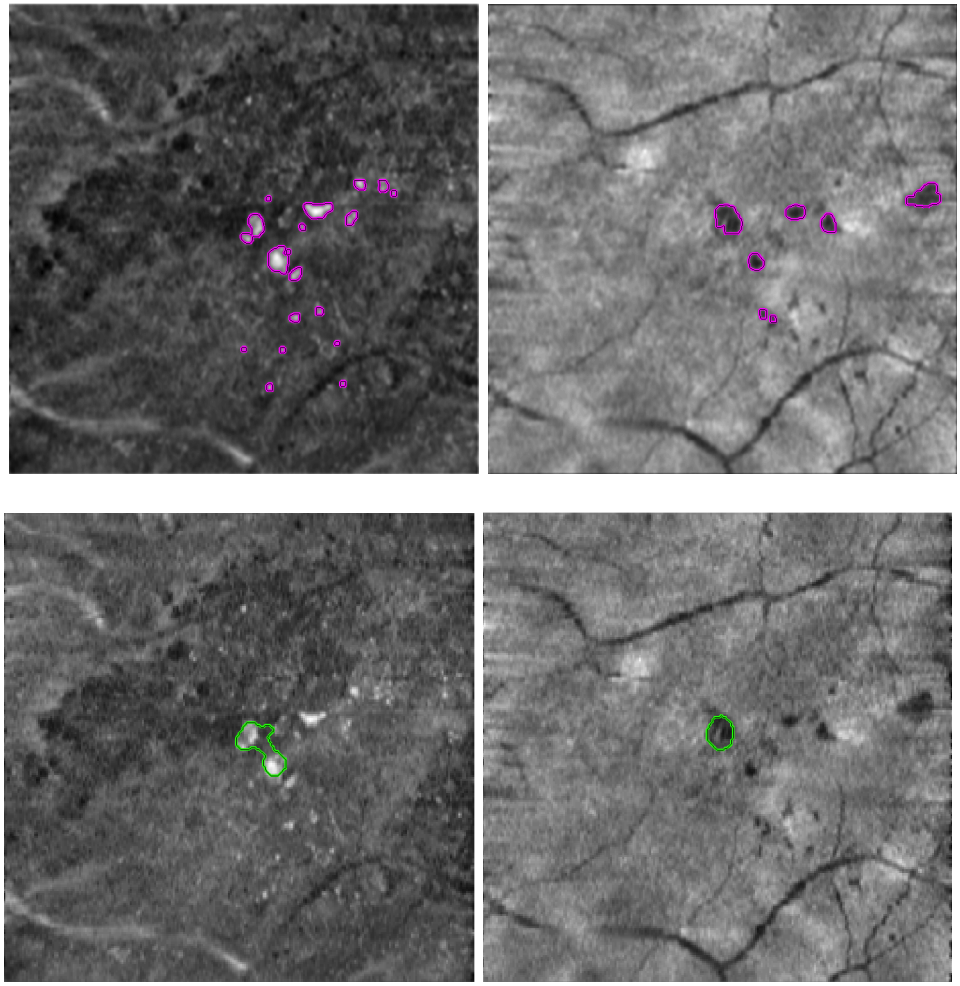

Figure 5.6. Comparison between our method (top row) and distance-regularized level-set evolution method (bottom row) [9] on the IPL and ISOS layer respectively.

intensity. By taking projection profiles horizontally and vertically and by analyzing the sudden increase or decrease of intensity, the location and size of the lesions can be estimated with improved accuracy. Once the lesion is approximately localized, the initial contour can be drawn around the lesions thus facilitating the segmentation process and increasing its speed. We also propose a novel level-set method which incorporates shape priors and metrics derived from those priors to propagate the curve towards boundaries of objects of interest. The shape priors are defined once using Fourier descriptors taken from existing pathologies in the en face images and these priors are embedded as the initial contour. This initial contour then evolves across the subsequent layers. The parameters of the level-set equation are replaced with parameters which can more appropriately handle intensity variations in within objects. After segmentation, the centroids and areas of pathologies in the IPL and ISOS layers are measured to determine whether the pathologies visible in the ISOS layer are optical or neural in nature. For our current data, we conclude that the pathologies visible in the ISOS layer are optical in nature due to the high degree of co-localization of pathologies between the two layers. Application of this technique can allow clinicians to observe the morphological changes brought about by disease and can also provide insight into the integrity of the ISOS layer. Results provided show that our method segments pathologies across the layers and can quantitatively assess the degree of change over time and with treatment.

CHAPTER 6

FEATURES AND METRICS FOR MONITORING THE TREATMENT OF NEOVASCULAR AGE-RELATED MACULAR DEGENERATION

Age-related macular degeneration (AMD) is the leading cause of vision loss in the elderly. A common clinical manifestation of neovascular AMD is accumulation of subretinal fluid (SRF) caused by leakage from choroidal neovascularization (CNV). Currently available therapy to reduce CNV leakage is the administration of anti-vascular endothelial growth factor (VEGF) agents, which has resulted in significantly less morbidity and improvement of visual acuity [105, 106]. Spectral domain optical coherence tomography (SDOCT) is used to help guide management of neovascular AMD patients by providing a cross sectional view of the retinal depth, visualization of SRF, and quantitative measurement of central subfield thickness (CST). However, evaluation of changes in SRF is subjective and requires review of multiple SDOCT B-scans obtained at different time points. Recently, automated techniques based on OCT B-scans or volume data have been developed to identify and measure intra-retinal and sub-retinal fluid [107–111]. However, to our knowledge, quantitative evaluation of changes in SRF with treatment has not been reported. Due to recent improvements in OCT technology that allow rapid acquisition of multiple B-scans and dense raster scanning, en face OCT imaging has emerged as a new imaging modality for visualization of retinal structure [16, 33, 112–120]. Owing to the high depth resolution of SDOCT B-scans, en face OCT images have high contrast for visualization of retinal pathologies. In addition, en face OCT images are compatible

with images obtained with traditional imaging modalities such as fundus digital imaging and fluorescein angiography. The purpose of this study is to demonstrate an en face imaging method based on SDOCT for quantitative measurement of changes in SRF area in subjects undergoing treatment for neovascular AMD.

6.1 Image Acquisition

SDOCT imaging was performed in one or both eyes of 5 subjects (2 male, 3 female) diagnosed with neovascular AMD at clinical visits. The ages of subjects ranged from 68 to 85 years, with a mean age of 78 $\pm$ 7 years. The subjects were examined clinically and visual acuity (VA) was measured. Standard density SDOCT imaging (Spectralis, Heidelberg, Germany), consisting of 19 raster B-scans, was performed as part of the clinical examination. High density SDOCT imaging with 145 B-scans over a 4.4 mm x 4.4 mm retinal area was performed and infrared (IR) scanning laser ophthalmoscope (SLO) fundus images were acquired. Total retinal thickness maps were generated from the high density SDOCT volume using the instruments software and the CST was recorded. Description of the generation of the en face images is reported in [33].

6.2 En face OCT image segmentation

To quantitatively measure and compare SRF areas between visits, en face OCT images are processed in 3 steps. In the first step, image equalization is performed to account for image background intensity differences between visits. A rectangular region of interest (ROI) encompassing regions of SRF is manually defined and the image background intensity mean is calculated by averaging intensity values of pixels outside the ROI. The difference in the background intensity means at the visits is calculated. Then, each pixel value of the entire

en face OCT image which has the lower background intensity mean is adjusted by adding a value equal to half of the calculated difference. Similarly, for the en face OCT image which has the higher background intensity mean, each pixel value is adjusted by subtracting a value equal to half of the calculated difference. In the second step, image segmentation is performed to automatically identify and demarcate regions of SRF. The ROIs from each visit are first smoothed using a 2D averaging filtering and then binarized using an identical intensity threshold determined by Otsus method to assign pixels in SRF regions to a value of one. A condition on size is then applied to eliminate small, non-connected regions and small holes within segmented regions in the binary images. In the third step, the geometrical areas of the SRF regions are determined by counting pixels within the regions. In addition, the boundaries of these regions are determined using the Moore-Neighbor tracing algorithm and are displayed for visual verification of the automated segmentation results. Area ratios are calculated by dividing the second visit area values by the first visit area values. Area ratios that are greater or less than 1 denoted an increase or decrease in the area of SRF, respectively.

6.3 Results

Examples of IR SLO images, HD SDOCT B-scans, en face OCT images, and retinal thickness maps obtained at 2 visits (8 months apart) in the right eye of a 30 year old visually normal male are shown in Figure 6.1. On the HD SDOCT B-scans, a foveal depression corresponding to normal anatomy is visualized. The appearance of en face OCT images obtained at the 2 visits is similar. Both images display shadows of the overlying retinal vasculature and have uniform

intensities. From retinal thickness maps, the CST measurements are 270 and 269 microns at visit 1 and 2, respectively and visual acuity at both visits is 20/20.

Examples of IR SLO images, HD SDOCT B-scans, en face OCT images, and retinal thickness maps obtained at 2 visits (5 months apart) in the left eye of a 68 year old male with a history of neovascular AMD and SRF are shown in Figure 6.2. Intravitreal injections are administered according to clinical protocol between en face OCT imaging. The HD SDOCT B-scans reveal SRF, visualized as a sub-foveal region with minimal light reflectance. On en face OCT images, irregularly shaped dark regions are observed corresponding to SRF. The boundaries of these regions as identified by image segmentation are outlined (Figure 6.2). The area ratio of the dark regions is 0.44, indicating a reduction in the SRF area. From the retinal thickness maps, CST is 377 and 280 microns at visit 1 and 2, respectively. Visual acuity is 20/30 and 20/25 at visits 1 and 2, respectively.

On en face outer retinal images, pigment epithelium detachment (PED) appears as bright regions, while subretinal fluid (SRF) is observed as dark regions. The area and intensity of these regions are quantitatively measured on en face outer retinal images and compared in the same subject. A decrease in area or an increase in intensity of dark regions on en face outer retinal images corresponds with a decrease in retinal thickness and improved vision. The investigated methods have the potential to provide a more accurate and detailed view of changes in pathologies due to disease progression and treatment.

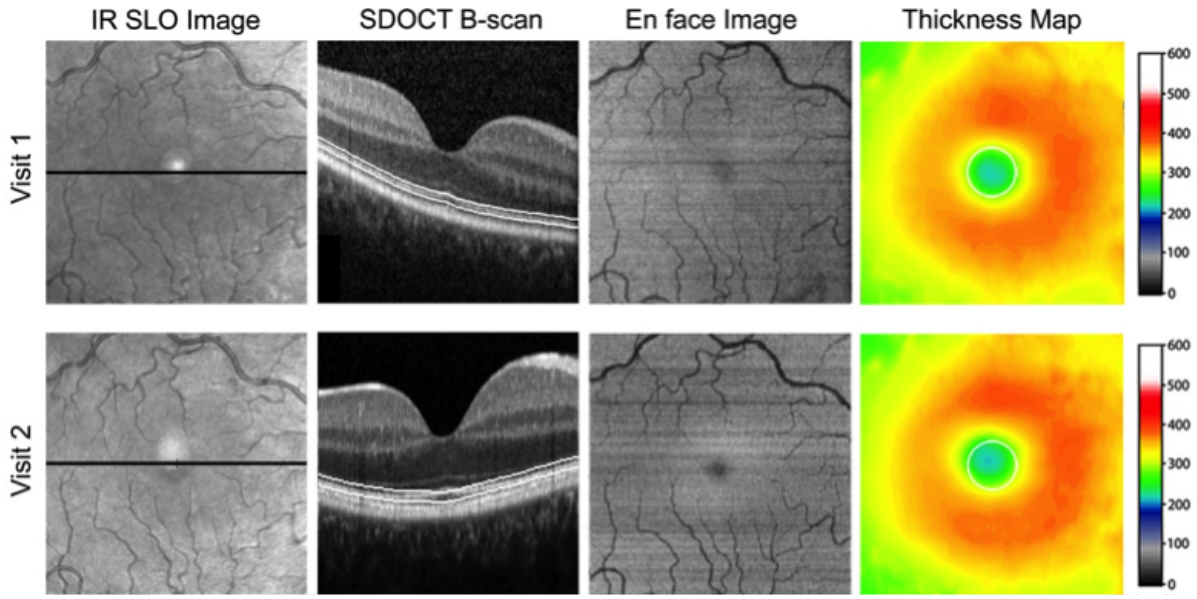

Figure 6.1. Examples of IR SLO images, high density (HD) SDOCT B-scans, en face OCT images, and retinal thickness maps obtained at 2 visits from the right eye of a 30 year old normal healthy male. The location of the HD SDOCT B-scans is shown with black horizontal lines on IR SLO images.

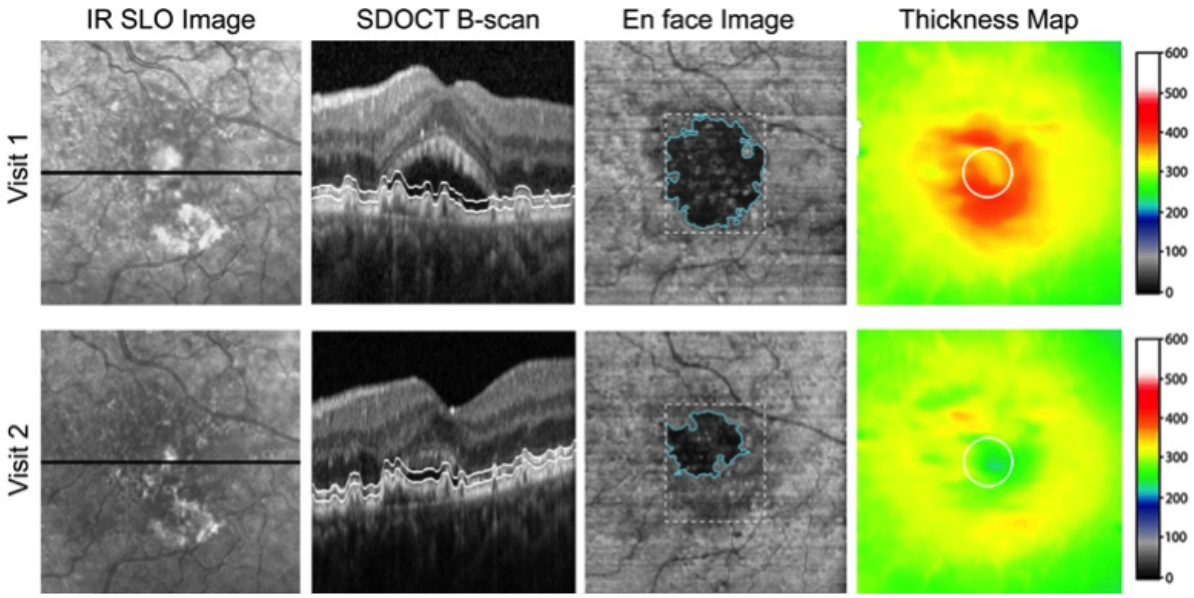

Figure 6.2. . Examples of IR SLO images, high density (HD) SDOCT B-scans, en face OCT images, and retinal thickness maps obtained at 2 visits from the left eye of a 68 year old male with neovascular AMD. On en face OCT images, the region of interest and the area of reduced intensity are outlined with dotted white and solid cyan lines, respectively. On en face OCT images, irregularly shaped dark areas were visualized due to the presence of subretinal fluid (SRF).

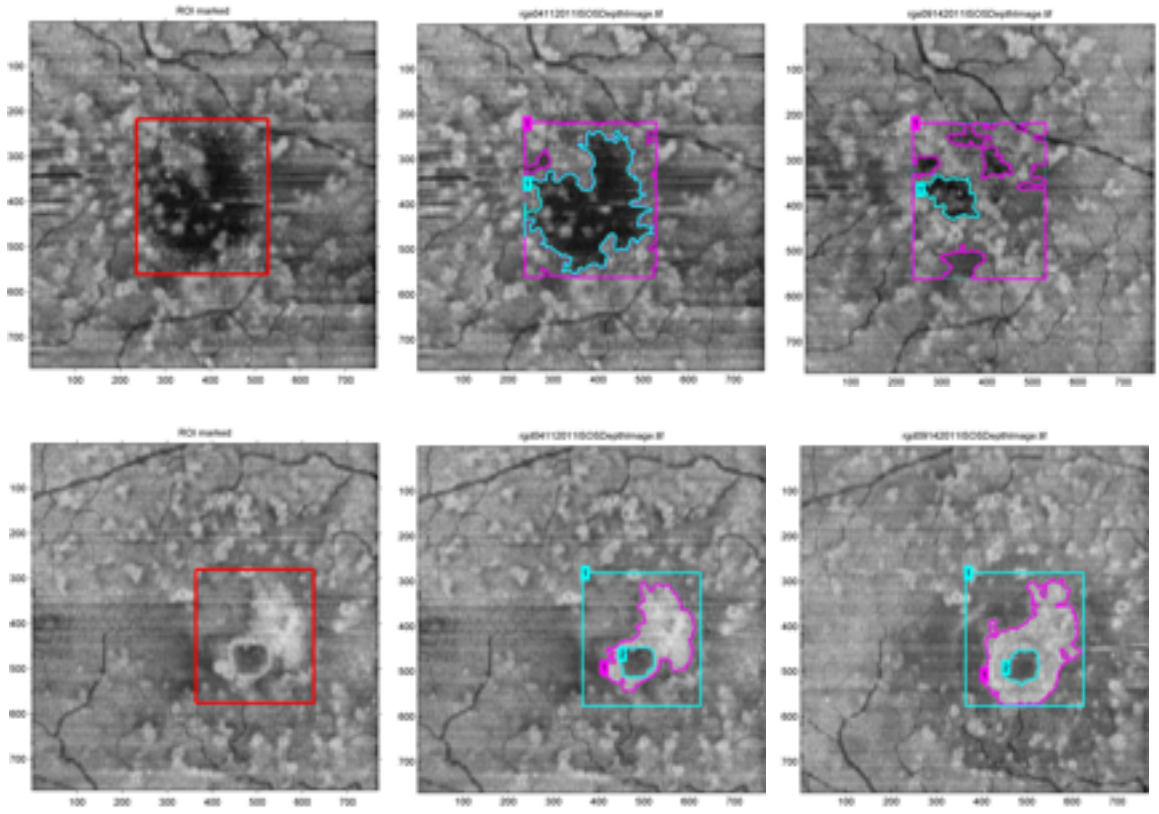

Figure 6.3. Top row: Segmentation on first visit. Bottom row: Segmentation on second visit. Pink refers to light ROI. Blue corresponds to dark ROI

CHAPTER 7

CONCLUSION AND DISCUSSIONS

Due to the advancement of retinal imaging systems, small focal changes in the retina can be detected and measured more accurately. These discoveries can aid in resolving unexplained visual symptoms or visual loss. There is a high association between the disturbance of the photoreceptor inner and outer segment and a diminishing of visual acuity [26]. In a healthy retina, the cones are densely packed and are resolved and produce a regular cone mosaic. If however the cones experience structural changes due to the presence of disease, they may become less reflective. These changes show up as dark spaces in the AO images and also as indistinct OS/RPE layers in the OCT images [88].

Automated methods for the analysis of retinal images is important due to its potential for screening and diagnosis of diseases that affect human vision. Drawbacks of existing methods are due to the complicated nachallenges presented by low quality images. These challenges often require human intervention, thus making most algorithms semi-automatic. The need for automated methods that can seamlessly process large amounts of data in a timely manner is necessary. For the problem of photoreceptor cell integrity estimation, we introduce a method that overcomes the shortcomings of existing methods by using content-adaptive filtering (CAF). In this method, image frequency content is initially analyzed using intensity profiles in the spatial domain to design a customized filter with a pass-band to emphasize cell structures suitable for subsequent processing. The McClellan transform [1] is used to design the circularly

symmetric bandpass filter since retinal cells have no preferred orientation. The automated filter design eliminates the need for manual determination of cell structure parameters, such as cell spacing. Following the preprocessing step, cell density estimation is performed on the binarized filtered image by finding regional points of high intensity. Photoreceptor cell estimates using this automated procedure are found to be comparable to manual estimates (gold standard). The new method when applied to test images and retinal images and shows over- all improved performance when compared with previously reported methods requiring user-supplied input.

A potential drawback of measuring photoreceptor density in the spatial domain is that the intensity profiles can be greatly affected by the presence of noise. Peaks in the profile which may be representative of noise may be incorrectly identified as cells. In order to overcome this possible limitation, we analyze the cone mosaic in the frequency domain. We describe an image model using a windowed 2D lattice of pulses representing the cells and characterize the frequency content as decaying frequency domain pulses on the reciprocal lattice. Based on this, we propose a novel method for detection of cone photoreceptor cells by analyzing the discrete-space Fourier transform of AO retinal images. This method uses a small-extent, block-based, 2D Discrete Fourier transform (DFT) to determine cell frequency content in order to obtain the parameters of an adaptive circularly symmetric band-pass filter that is applied to the image. The filter extracts the underlying cellular structure and removes high-frequency noise as well as very low frequency contamination manifested as slow intensity variations in the image. We test the robustness of our method by applying it to images corrupted by noise as well as to images which have been artificially manipulated so that cell structure appears different.

Subsequent detection yields an automated cell estimate that compares well with actual and manual estimates on test and retinal images and demonstrates the accuracy of the method.

Several studies have shown high correlation between the integrity of ISOS layer and photoreceptor cells. Retinal degeneration due to disease ultimately results in the death of the photoreceptors and leads to the death of the inner and outer segment layers in the retina. It is therefore desirable to develop automated segmentation techniques to identify lesions in retinal images in order to reduce the inter-observer variability as well as the manual segmentation effort and time. We investigate the segmentation of pathologies in fluorescein angiograms and en face retinal images in patients with age-related macular degeneration and diabetic retinopathy by building upon the level-set method based on the classical Chan-Vese model. Image acquisition is performed during different patient visits to emphasize the changes in pathology over time as a result of treatment. We explore an improved method for pathology segmentation in retinal images which automatically isolates the pathology without the need to specify the location of an initial contour. This is accomplished by exploiting a priori knowledge of the shape and intensity distribution allowing the use of projection profiles to detect the presence of pathologies that are characterized by intensity differences with surrounding areas in retinal images. The method provides improved reliability in the segmentation which may fail in classical algorithms with a random choice of the initial contour. Results indicate that the improvement is attained with a reduced number of iterations thereby increasing the speed of convergence as the initial contour encloses the region of interest on the first iteration. The results of this study indicated a strong relationship between the integrity of the ISOS junction layer and visual acuity. Pathologic

regions observed in the ISOS en face image indicate areas of cell death, which appear as dark patches in AO retinal images. We extend our research by including in our analysis the en face images of seven layers of the retina. A wealth of information is available upon examining the layers in conjunction with one another and by observing how the pathologies flow from one layer to the next. Analysis of the ISOS layer individually is insufficient to conclude the origins of the disease and the extent to which the disease has progressed. By including multiple layers in our study, we are able to provide insight as to how abnormalities in the upper layer of the retina are represented in the ISOS layer. The level-set approach is used for a preliminary analysis and this approach proves useful when segmenting pathologies across multiple layers. We develop a level-set model that uses Fourier descriptor based shape priors to specify a target shape. The final level-set function obtained for a given image is used as the initial level-set function for the image in the next sequential layer. In this way, the segmentation flows across the images and the problem of specifying an initial contour is seamlessly handled as pathologies tend to be grouped in the same location and the result of segmenting one layer is used as the initial contour to the next layer. Use of Fourier descriptors allows for the definition of target shapes which are invariant to rotation, scale, and translation. Metrics such as the area of the pathologies and their centroids are obtained and used to determine whether the pathologies visible on the ISOS layer are neural or optical in nature. Neural pathologies occur directly on the ISOS layer and indicate irreversible photoreceptor disruption. Areas of loss of ISOS integrity visible on the ISOS en face image would appear as black patches on the corresponding AO image, indicating regions of photoreceptor cell death. In the case of optical pathologies, abnormalities appear

on the inner plexiform layer (IPL) and cause optical effects, such as shadowing on the ISOS layer. Given the proper treatment, these abnormalities in the IPL layer can be removed, thus restoring the high reflectivity and integrity of the ISOS layer.

7.1 Future Work

Studies have shown that a loss of the photoreceptor mosaic in the AO images are comparable with the area of the ISOS disturbance in OCT images. Therefore, by understanding how disease affects the layers of the retina, correlations can be constructed between the integrity of the ISOS layer and photoreceptor density. We have taken the first step towards identifying the origins of disease in order to appropriately offer effective treatment plans. The use of our methods on a single patient are inadequate to offer conclusive results. For future work, it would be of great interest to apply our methods to a minimum of twenty patients in order to observe trends which may be appearing. As the en face images are constructed from multiple B-scans, it would also be of interest to incorporate the data from B-scans so as to provide a form of cross-correlation between the two forms of images in areas where abnormalities are present. Level-set methods and analysis of image data in the frequency domain have been effective means of reaching our goals. Other methods such as wavelet decomposition and image manifolds can also be looked into

Bibliography

[1] L.R.Rabiner, J.H.McClellan, and T.W.Parks: Fir digital filter design techniques using weighted chebyshev approximation. Proceedings of the IEEE, 1975.

[2] Chan, T. and L.A.Vese: Active contours without edges. IEEE Transactions On Image Processing, 10, 2001.

[3] Pediatric Retina. Springer Berlin Heidelberg, 2011.

[4] Mujat, M., Ferguson, R. D., Iftimia, N., and Hammer, D. X.: High resolution multimodal clinical ophthalmic imaging system. Optics Express. Optical Society of America, 2010.

[5] Xue, B. and Choi, S. S.: Photoreceptor counting and montaging of en-face retinal images from an adaptive optics fundus camera. JOSA, 2007.

[6] Chui, T. Y. P., Song, H., and Burns, S. A.: Individual variations in human cone photoreceptor packing density: Variations with refractive error. Investigative Ophthalmology Visual Science, pages 4679–4687, 2008.

[7] Liang, J. Z., Williams, D. R., and Miller, D. T.: Supernormal vision and high-resolution retinal imaging through adaptive optics. Journal of the Optical Society of America a-Optics Image Science and Vision, pages 2884–2892, 1997.

[8] Yellott, J. I.: Spectral analysis of spatial sampling by photoreceptors: Topological aliasing. Vision Research, 22, 1982.

[9] Li, C., Xu, C., Gui, C., and Fox, M. D.: Distance regularized level set evolution and its application to image segmentation. IEEE Transactions On Image Processing, pages 195–215, 2010.

[10] Maheshwary, A. S., Oster, S. F., Yuson, R. M., Cheng, L., Mojana, F., and Freeman, W. R.: The association between percent disruption of the photoreceptor inner segmentouter segment junction and visual acuity in diabetic macular edema. American Journal of Ophthalmology, pages 63–67, 2010.

[11] S, O., M, H., A, S., A, T., K, Y., Y, O., Y, Y., H, M., S, O., T, I., and N, Y.: High-resolution imaging of resolved central serous chorioretinopathy using adaptive optics scanning laser ophthalmoscopy. Ophthalmology, 2010.

[12] KE, T., K, R., SM, S., AS, L., BJ, L., W, T., TC, P., A, R., and JL, D.: Longitudinal study of cone photoreceptors during retinal degeneration and in response to ciliary neurotrophic factor treatment. Investigative Ophthalmology and Visual Science, 2011.

[13] JI, W., M, C., J, C., A, R., and DR, W.: High-resolution retinal imaging of cone-rod dystrophy. Ophthalmology, 113:1014–1019, 2006.

[14] SS, C., N, D., JL, H., SM, J., JL, K., SS, O., and JS, W.: In vivo imaging of the photoreceptor mosaic in retinal dystrophies and correlations with visual function. Investigative Ophthalmology and Visual Science, 2006.

[15] JL, D., Y, Z., J, G., C, N., M, O., KE, B., A, S., and A, R.: High-resolution imaging with adaptive optics in patients with inherited retinal degeneration. Investigative Ophthalmology and Visual Science, 2007.

[16] Gorczynska, I., Srinivasan, V. J., Vuong, L. N., Chen, R. W. S., Liu, J. J., Reichel, E., Wojtkowski, M., Schuman, J. S., Duker, J. S., and Fujimoto, J. G.: Projection oct fundus imaging for visualizing outer retinal pathology in non-exudative age-related macular degeneration. Br J Ophthalmology, pages 603–609, 2009.

[17] de Jong, P. T.: Age-related macular degeneration. New England Journal of Medicine, 2006.

[18] Li, K. Y. and Roorda, A.: Automated identification of cone photoreceptors in adaptive optics retinal images. JOSA, 2007.

[19] T.Y.P. Chui, H.X. Song, S. A. B.: Adaptive optics imaging of human cone photoreceptor distribution. JOSA, 2008.

[20] Bao, H., Rao, C., Zhang, Y., Dai, Y., Rao, X., and Fan, Y.: Hybrid filtering and enhancement of high-resolution adaptive-optics retinal images. Optics Letters, 2009.

[21] Li, K., Tiruveedhula, P., and Roorda, A.: Intersubject variability of foveal cone photoreceptor density in relation to eye length. 2010.

[22] Loquin, K., Bloch, I., Nakashima, K., Rossant, F., and Paques, M.: Photoreceptor detection in in-vivo adaptive optics images of the retina: Towards a simple interactive tool for the physicians. IEEE, 2011.

[23] Mohammad, F., Ansari, R., Wanek, J. M., , and Shahidi, M.: Photoreceptor cell counting in adaptive optics retinal images using content-adaptive filtering. Medical Imaging. SPIE, 2010.

[24] Mohammad, F., Ansari, R., Wanek, J. M., , and Shahidi, M.: Frequency-based local content adaptive filtering algorithm for automated photoreceptor cell density quantification. ICIP. IEEE, 2012.

[25] Mohammad, F., Ansari, R., , and Shahidi, M.: A level-set method for pathology segmentation in fluorescein angiograms and en face retinal images of patients with age-related macular degeneration. Medical Imaging. SPIE, 2013.

[26] Kitaguchi, Y., Fujikado, T., Bessho, K., Sakaguchi, H., Gomi, F., Yamaguchi, T., Nakazawa, N., Mihashi, T., and Tano, Y.: Adaptive optics fundus camera to examine localized changes in the photoreceptor layer of the fovea. American Academy of Ophthalmology, 2008.

[27] Roorda, A., Romero-Borja, F., Donnelly, W. J., Queener, H., Hebert, T. J., and Campbell, M. C. W.: Adaptive optics scanning laser ophthalmoscopy. pages 405–412. Optics Express, 2002.

[28] eds. D. Purves, G. Augustine, and D. Fitzpatrick Neuroscience. Sinauer Associates, second edition, 2001.

[29] C, C., K, S., R, K., and A, H.: Human photoreceptor mosaic topography. Journal of Comparative Neurology, page 497523, 1990.

[30] Pircher, M., Zawadzki, R. J., Evans, J. W., Werner, J. S., and Hitzenberger, C. K.: Simultaneous imaging of human cone mosaic with adaptive optics enhanced scanning laser ophthalmoscopy and high-speed transversal scanning optical coherence tomography. volume 33 of Optics Letters. Optical Society of America, 2008.

[31] Gelas, A., Mosaliganti, K., Gouaillard, A., Souhait, L., Noche, R., Obholzer, N., and Megason, S. G.: Variational level-set with gaussian shape model for cell segmentation. ICIP and IEEE, 2009.

[32] Neill-Biba, M. O., Sivaprasad, S., Rodriguez-Carmona, M., Wolf, J. E., and Barbur, J. L.: Loss of chromatic sensitivity in amd and diabetes: a comparative study. Ophthalmic and Physiological Optics, pages 705–716, 2010.

[33] Wanek, J., Zelkha, R., Lim, J. I., and Shahidi, M.: Feasibility of a method for en face imaging of photoreceptor cell integrity. American Journal of Ophthalmology, pages 807–814, 2011.

[34] Xu, J., Ishikawa, H., Wollstein, G., and Schuman, J.: 3d optical coherence tomography super pixel with machine classifier analysis for glaucoma detection. EMBS. IEEE, 2011.

[35] Schuman, J. S.: Spectral domain optical coherence tomography for glaucoma, (an aos thesis). Transactions of American Ophthalmological Society, 106, 2008.

[36] Ishikawa, H., Bilonick, R., Wollstein, G., Xu, J., Kagemann, L., and Schuman, J.: Macular inner-retinal layer thickness super pixel analysis for glaucoma using spectral domain optical coherence tomography (sd-oct). 2009.

[37] W, D., H, S., B, H., TH, K., M, S., A, U., C, S., O, F., M, W., JG, F., and AF, F.: Enhanced visualization of macular pathology with the use of ultrahighresolution optical coherence tomography. Archives of Ophthalmology, pages 695–706, 2003.

[38] M, G., B, H., C, S., H, S., PK, A., and W, D.: Histologic correlation of pig retina radial stratification with ultrahigh-resolution optical coherence tomography. Investigative OphthalmologyVisual Science , pages 1696–1703, 2003.

[39] RA, C., D, C., M, S., JA, C., JC, C., Jr, M. L., MC, M., and PK, K.: Optical coherence tomography 3: automatic delineation of the outer neural retinal boundary and its influence on retinal thickness measurements. Investigative OphthalmologyVisual Science , page 23992406, 2004.

[40] Cherezova, T.: Measurement and correction of human eye aberrations. Lasers and Electro-Optics. IEEE, 2003.

[41] Zawadzki, R. J., Jones, S. M., Olivier, S. S., Zhao, M. T., Bower, B. A., Izatt, J. A., Choi, S., Laut, S., and Werner, J. S.: Adaptive-optics optical coherence tomography for high resolution and high-speed 3d retinal in vivo imaging. Optics Express, page 85328546. Optical Society of America, 2005.

[42] Gray, D. C., Merigan, W., Wolfing, J. I., Gee, B. P., Porter, J., Dubra, A., Twietmeyer, T. H., Ahmad, K., Tumbar, R., Reinholz, F., and Williams, D. R.: In vivo fluorescence imaging of primate retinal ganglion cells and retinal pigment epithelial cells. Optics Express, page 71447158. Optical Society of America, 2006.

[43] Zhang, Y. H., Poonja, S., and Roorda, A.: Mems-based adaptive optics scanning laser ophthalmoscopy. Optics Letters, page 12681270. Optical Society of America, 2006.

[44] Gargasson, J. F. L., Glanc, M., and Lena, P.: Retinal imaging with adaptive optics. Optics Letters, page 11311138, 2001.

[45] Roorda, A.: Adaptive optics ophthalmoscopy. Journal of Refractive Surgery, pages 279–289, 2000.

[46] Roorda, A. and Williams, D. R.: The arrangement of the three cone classes in the living human eye. Nature, page 520522, 1999.

[47] Fernndez, E., Hermann, B., Povaay, B., Unterhuber, A., Sattmann, H., Hofer, B., Ahnelt, P., and Drexler, W.: Ultrahigh resolution optical coherence tomography and pancorrection for cellular imaging of the living human retina. Optics Express, page 12681270. Optical Society of America, 2008.

[48] Ruixue, L., Dayu, L., Mingliang, X., Ningning, K., Yue, Q., Xianliang, Z., and Li, X.: Laser beacon adaptive optics ophthalmoscope for retinal multilayer imaging. ISBB. IEEE, 2011.

[49] Niu, S., Shen, J., Liang, C., Zhou, L., and Li, B.: Research on human retinal cell image restoration. CISP. IEEE, 2010.

[50] Ling, N., Zhang, Y., Rao, X., Wang, C., Hu, Y., and Jiang, W.: High resolution mosaic image of capillaries in human retina by adaptive optics. volume 3, pages 225–226. Chinese Optics Letters, 2005.

[51] Williams, D. R.: Adaptive optics for the human eye. 2003.

[52] Carroll, J., Neitz, M., Hofer, H., Neitz, J., and Williams, D. R.: Functional photoreceptor loss revealed with adaptive optics: An alternate cause of color blindness. PNAS, 2004.

[53] Karnowski, T. P., Aykac, D., Giancardo, L., Li, Y., Nichols, T., Tobin, K., and Chaum, E.: Automatic detection of retina disease: Robustness to image quality and localization of anatomy structure. EMBS. IEEE, 2011.

[54] Sankaranand, U. R., Srinivasc, T., and Gurumurthy, K.: Mems based vision correction using adaptive optics. TENCON, 2006.

[55] Niu, S., Shen, J., Liang, C., and Li, B.: Human eye aberration measurement and correction based on micro adaptive optics system. Biomedical Engineering and Informatics. IEEE, 2009.

[56] Chen, D. C., Jones, S. M., Silva, D. A., and Olivier, S. S.: High-resolution adaptive optics scanning laser ophthalmoscope with dual deformable mirrors. JOSA, 24:1305–1312, 2007.

[57] S. A. Burns, R. Tumbar, A. E. E.: Large-field-of-view, modular, stabilized, adaptive-optics-based scanning laser ophthalmoscope. JOSA, 24, 2007.

[58] VJ, S., BK, M., M, W., RA, B., I, G., R, C., JS, D., JS, S., and JG, F.: Characterization of outer retinal morphology with high-speed, ultrahigh-resolution optical coherence tomography. Investigative OphthalmologyVisual Science , pages 1571–1579, 2008.

[59] Puliaffito, C. A., Hee, M. R., Lin, C. P., Reichel, E., Schuman, J. S., Duker, J. S., Izatt, J. A., Swanson, E. A., and Fujimoto, J. G.: Imaging of macular diseases with optical coherence tomography. Ophthalmology, pages 217–229, 1995.

[60] Drexler, W., Findl, O., Menapace, R., Kruger, A., Wedrich, A., Rainer, G., Baumgartner, A., Hitzenberger, C. K., and Fercher, A. F.: Dual beam optical coherence tomography: Signal identification for ophthalmologic diagnosis. J. Biomed. Opt., pages 55–65, 1998.

[61] Lattanzio, R., Brancato, R., Pierro, R., Bandello, F., Iaccher, B., Fiore, T., and Maestranzi, G.: Macular thickness measured by optical coherence tomography (oct) in diabetic patients. Eur. J. Ophthalmol., pages 482–487, 2002.

[62] Jonnal, R., Kocaoglu, O., Wang, Q., Lee, S., and Miller, D.: Phase-sensitive imaging of the outer retina using optical coherence tomography and adaptive optics. Biomedical Optics Express. Optical Society of America, 2011.

[63] Wolff, B., Matet, A., Vasseur, V., Sahel, J.-A., and Mauget-Fasse, M.: En face oct imaging for the diagnosis of outer retinal tubulations in age-related macular degeneration. Journal of Ophthalmology, 2012, 2012.

[64] Yazdanpanah, A., Hamarneh, G., Smith, B., and Sarunic, M.: Segmentation of intra-retinal layers from optical coherence tomography images using an active contour approach. IEEE Transactions on Medical Imaging, 30, 2011.

[65] Cremers, D., Rousson, M., and Deriche, R.: A review of statistical approaches to level set segmentation: Integrating color, texture, motion and shape. International Journal of Computer Vision, pages 195–215, 2007.

[66] Liu, Y. and Yu, Y.: Interactive image segmentation based on level sets of probabilities. IEEE Transactions On Visualization And Computer Graphics, 18, 2012.

[67] Qunaieer, F., Tizhoosh, H., and Rahnamayan, S.: Multi-resolution level set image segmentation using wavelets. ICIP. IEEE, 2011.

[68] Chan, T. and Zhu, W.: Level set based shape prior segmentation. volume 2 of Computer Vision and Pattern Recognition, pages 1164 – 1170. IEEE, 2005.

[69] Huang, C.-L.: Shape based level set method for image segmentation. 9th International Conference on Hybrid Intelligent Systems. IEEE, 2009.

[70] Liu, X., Lange, D. L., Haider, M. A., der Kwast, T. H. V., Evans, A. J., Wernick, M. N., and Yetik, I. S.: Unsupervised segmentation of the prostate using mr images based on level set with a shape prior. Engineering in Medicine and Biology, pages 3613–3616. IEEE, 2009.

[71] Chen, S. and Radke, R.: Level-set segmentation with both shape and intensity priors. International Conference on Computer Vision. IEEE, 2009.

[72] Yingjie, Z. and Liling, G.: Automatic generation of initial contours on image segmentation. Industrial Electronics and Applications, pages 837–842. IEEE, 2008.

[73] Yang, Y., Huang, S., Lin, P., and Rao, N.: Medical image segmentation based on level set combining with region information. 4th International Conference on Natural Computation. IEEE, 2008.

[74] Fundana, K., Overgaard, N. C., and Heyden, A.: Deformable shape priors in chan vese segmentation of image sequences. International Conference on Image Processing. IEEE, 2007.

[75] Cremers, D., Sochen, N., and C.Schnorr: Towards recognition-based variational segmentation using shape priors and dynamic labeling. volume 2695 of 4th International Conference on Scale Space Theories in Computer Vision, pages 388–400. Springer, 2003.

[76] Mumford, D. and Shah, J.: Optimal approximation by piecewise smooth functions and associated variational problems. Commun. Pure Applied Math, pages 577–685, 1989.

[77] Liu, G., Sun, X., Fu, K., and Wang, H.: Aircraft recognition in high-resolution satellite images using coarse to fine shape prior. volume 10 of Geoscience and remote sensing letters. IEEE, 2013.

[78] Cheng, K., Gu, L., and Xu, J.: A novel shape prior based level set method for liver segmentation from mr images. Proceedings of 5th International Conference on Information Technology and Application in Biomedicine. IEEE, 2008.

[79] Zhao, J., Shao, F., Xu, Y., Zhang, X., and Huang, W.: An improved chan-vese model without reinitialization for medical image segmentation. CISP. IEEE, 2010.

[80] Wei, Y., Xu, X., Jia, T., and Zhao, D.: An optimal level sets method for lung nodules detection in ct images. ISDA. IEEE, 2006.

[81] Yan, S., Yuan, J., and Hou, C.: Segmentation of medical ultrasound images based on level set method with edge representing mask. ICACTE. IEEE, 2010.

[82] Pan, Y., Birdwell, J., and Djouadi, S.: Efficient implementation of the chan-vese models without solving pdes. Multimedia Signal Processing. IEEE, 2006.

[83] Yang, Z., Kong, Y., and Fu, Y.: Decomposed contour prior for shape recognition. International Conference on Pattern Recognition. IEEE, 2012.

[84] Prisacariu, V. A. and Reid, I.: Nonlinear shape manifolds as shape priors in level set segmentation and tracking. CVPR, pages 2185–2192. IEEE, 2011.

[85] Charmi, M. A., Derrode, S., and Ghorbel, F.: Using fourier-based shape alignment to add geometric prior to snakes. ICASSP. IEEE, 2009.

[86] Charmi, M. A., Mezghich, M. A., MHiria, S., Derrode, S., and Ghorbel, F.: Geometric shape prior to region-based active contours using fourier-based shape alignment. Imaging Systems and Techniques, pages 478–481. IEEE, 2010.

[87] Wanek, J., Mori, M., and Shahidi, M.: Effect of aberrations and scatter on image resolution assessed by adaptive optics retinal section imaging. JOSA, pages 1296–1304, 2007.

[88] Choi, S. S., Zawadzki, R. J., Keltner, J. L., and Werner, J.: Changes in cellular structures revealed by ultra-high resolution retinal imaging in optic neuropathies. Investigative OphthalmologyVisual Science , 49, 2008.

[89] Jelinek, H. and Cree, M.: Automated detection of retinal pathology. CRC Press, 2009.

[90] Ebrahimdoost, Y., Dehmeshki, J., Ellis, T., Firoozbakht, M., Youannic, A., and Qanadli, S.: Medical image segmentation using active contours and a level set model: Application to pulmonary embolism (pe) segmentation. ICDS. IEEE, 2010.

[91] Reddy, G., Ramudu, K., Srinivas, A., and Rao, R. R.: Region based segmentation of satellite and medical imagery with level set evolution. RAICS. IEEE, 2011.

[92] L. Shuai-jie, S. Jin-ping, T. X.-c.: An algorithm of texture image segmentation by piecewise constant level set method based on image decomposition. World Congress on Computer Science and Information Engineering. IEEE, 2009.

[93] Li, F., Liu, R., and Shen, C.: Feature extraction and soft segmentation of texture images. IASP. IEEE, 2010.

[94] Zhang, Y., Matuszewski, B., L.K.Shark, and Moore, C.: Medical image segmentation using new hybrid level-set method. MEDIVIS. IEEE, 2008.

[95] Belaid, A., Boukerroui, D., Maingourd, Y., and Lerallut, J.: Phase-based level set segmentation of ultrasound images. IEEE Transactions On Information Technology In Biomedicine, 15, 2011.

[96] S. R. Russell, M. D. A.: Optimal filter framework for automated, instantaneous detection of lesions in retinal images. IEEE Transactions On Medical Imaging, 30, 2011.

[97] Tobin, K., Chaum, E., Govindasamy, P., and Karnowski, T.: Detection of anatomic structures in human retinal imagery. IEEE Transactions On Medical Imaging, 26, 2007.

[98] Ravindraiah, R., Shaik, F., Prasad, M., and Sreenivasulu, E.: Qualitative and quantitative analysis of segmentation of human retinal images. ICCCET. IEEE, 2011.

[99] Li, C., Huang, R., Ding, Z., J.C.Gatenby, and D.N.Metaxas: A level set method for image segmentation in the presence of intensity inhomogeneities with application to mri. IEEE Transactions On Image Processing, 20, 2011.

[100] Yuan, Y. and He, C.: Variational level-set methods for image segmentation based on both l^2 and sobolev gradients. Nonlinear Analysis: Real World Applications, pages 959–966, 2012.

[101] Zahn, C. T. and Roskies, R. Z.: Fourier descriptors for plane closed curves. IEEE Transactions on Computers, 1972.

[102] Zhang, D. and Lu, G.: A comparative study on shape retrieval using fourier descriptors with different shape signatures. Journal of Visual Communication and Image Representation, pages 41–60, 2003.

[103] van Rensburg, F. J., Treurnicht, J., and Fourie, C.: The use of fourier descriptors for object recognition in robotic assembly. 2009.

[104] Zhang, D. and Lu, G.: A comparative study of fourier descriptors for shape representation and retrieval. ACCV:The 5th Asian Conference on Computer Vision. IEEE, 2002.

[105] Brown, D., Kaiser, P. K., Michels, M., Soubrane, G., Heier, J., Kim, R. Y., Sy, J. P., and Schneider, S.: Ranibizumab versus verteporfin for neovascular age-related macular degeneration. New England Journal of Medicine, pages 1432–1444, 2006.

[106] Rosenfeld, P., Brown, D., Heier, J., Boyer, D., Kaiser, P., Chung, C., and Kim, R. Y.: Ranibizumab for neovascular age-related macular degeneration. New England Journal of Medicine, pages 1419–1431, 2006.

[107] Chen, X. J., Niemeijer, M., Zhang, L., Lee, K., Abramoff, M. D., and Sonka, M.: Three-dimensional segmentation of fluid-associated abnormalities in retinal oct: Probability constrained graph-search-graph-cut. Transactions on Medical Imaging, pages 1521–1531, 2012.

[108] Fernandez, D. C.: Delineating fluid-filled region boundaries in optical coherence tomography images of the retina. Transactions on Medical Imaging, pages 929–945, 2005.

[109] Wilkins, G. R., Houghton, O. M., and Oldenburg, A. L.: Automated segmentation of intraretinal cystoid fluid in optical coherence tomography. Transactions on Biomedical Engineering, pages 1109–1114, 2012.

[110] Zheng, Y. L., Sahni, J., Campa, C., Stangos, A. N., Raj, A., and Harding, S. P.: Computerized assessment of intraretinal and subretinal fluid regions in spectral-domain optical coherence tomography images of the retina. American Journal of Ophthalmology, pages 277–286, 2013.

[111] Quellec, G., Lee, K., Dolejsi, M., Garvin, M. K., Abramoff, M. D., and Sonka, M.: Three-dimensional analysis of retinal layer texture: identification of fluid-filled regions in sd-oct of the macula. Transactions on Medical Imaging, pages 1321–1330, 2010.

[112] Kaluzny, J. J., Wojtkowski, M., Sikorski, B. L., Szkulmowski, M., Szkulmowska, A., Bajraszewski, T., Fujimoto, J. G., Duker, J. S., Schuman, J. S., and Kowalczyk, A.: Analysis of the outer retina reconstructed by high-resolution, three-dimensional spectral domain optical coherence tomography. Ophthalmic Surg Lasers Imaging, pages 102–108, 2009.

[113] Pircher, M., Gotzinger, E., and Hitzenberger, C. K.: Dynamic focus in optical coherence tomography for retinal imaging. Biomedical Optics, 2006.

[114] Podoleanu, A. G., Dobre, G. M., Cucu, R. G., Rosen, R., Garcia, P., Nieto, J., Will, D., Gentile, R., Muldoon, T., Walsh, J., Yannuzzi, L. A., Fisher, Y., Orlock, D., Weitz, R., Rogers, J. A., Dunne, S., and Boxer, A.: Combined multiplanar optical coherence tomography and confocal scanning ophthalmoscopy. Biomedical Optics, pages 86–93, 2004.

[115] Wojtkowski, M., Sikorski, B., Gorczynska, I., Gora, M., Szkulmowski, M., Bukowska, D., Kaluzny, J., Fujimoto, J., and Kowalczyk, A.: Comparison of reflectivity maps and outer retinal topography in retinal disease by 3-d fourier domain optical coherence tomography. Optics Express, pages 4189–4207. Optical Society of America, 2009.

[116] Jiao, S., Wu, C., Knighton, R. W., Gregori, G., and Puliafito, C. A.: Registration of high-density cross sectional images to the fundus image in spectral-domain ophthalmic optical coherence tomography. Optics Express, 2006.

[117] Hitzenberger, C., Trost, P., Lo, P. W., and Zhou, Q.: Three-dimensional imaging of the human retina by high-speed optical coherence tomography. Optics Express, 2003.

[118] Alkabes, M., Salinas, C., Vitale, L., Bures-Jelstrup, A., Nucci, P., and Mateo, C.: En face optical coherence tomography of inner retinal defects after internal limiting membrane peeling for idiopathic macular hole. Invest Ophth Vis Sc, 2011.

[119] Coscas, F., Coscas, G., Querques, G., Massamba, N., Querques, L., Bandello, F., and Souied, E. H.: En face enhanced depth imaging optical coherence tomography of fibrovascular pigment epithelium detachment. Invest Ophth Vis Sc, 2012.

[120] Rispoli, M., Rouic, J. F. L., Lesnoni, G., Colecchio, L., Catalano, S., and Lumbroso, B.: Retinal surface en face optical coherence tomography: a new imaging approach in epiretinal membrane surgery. Retina, 2012.

[121] Airouche, M., Bentabet, L., and Zelmat, M.: Image segmentation using active contour model and level set method applied to detect oil spills. Proceedings of the World Congress on Engineering. WCE, 2009.

[122] Akram, M. U., Tariq, A., Anjum, M. A., and Javed, M. Y.: Automated detection of exudates in colored retinal images for diagnosis of diabetic retinopathy. Applied Optics, pages 4858–4866, 2012.

[123] G, L., E, S., PM, G., WH, S., and RB, R.: Inner segment-outer segment junctional layer integrity and corresponding retinal sensitivity in dry and wet forms of age-related macular degeneration. Retina, pages 364–370, 2011.

[124] K., S., S, S., and PK, K.: Photoreceptor status after antivascular endothelial growth factor therapy in exudative age-related macular degeneration. Br J Ophthalmol, pages 622–626, 2009.

[125] J, O., WE, S., HW, F., G, J. G., and B, L.: Photoreceptor inner/outer segment defect imaging by spectral domain oct and visual prognosis after macular hole surgery. Investigative OphthalmologyVisual Science , pages 1651–1658, 2010.

[126] Wang, L.: A level set model without initial contour. Workshop on Applications of Computer Vision. IEEE, 2009.

[127] Mujat, M., Ferguson, R. D., Iftimia, N., and Hammer, D. X.: Compact adaptive optics line scanning ophthalmoscope. Optics Express. Optical Society of America, 2009.

[128] Srinivasan, V., Adler, D. C., Chen, Y., Gorczynska, I., Huber, R., Duker, J. S., Schuman, J. S., and Fujimoto, J.: Ultrahigh-speed optical coherence tomography for three-dimensional and en face imaging of the retina and optic nerve head. Investigative OphthalmologyVisual Science , 49, 2008.

[129] Werner, J., Keltner, J., Zawadzki, R., and Choi, S.: Outer retinal abnormalities associated with inner retinal pathology in nonglaucomatous and glaucomatous optic neuropathies. Eye, Scientific Journal of Royal College of Ophthalmologists, pages 279–289, 2011.

[130] Barnes, T. B., Thompson, C. A., Sawvel, R. M., Silva, D. A., Wilks, S. C., Olivie, S. S., and Werner, J. S.: A high-resolution adaptive optics system for vision science. Investigative Ophthalmology Visual Science, 2002.

[131] Zawadzki, R. J., Choi, S. S., Fuller, A. R., Evans, J. W., Hamann, B., and Werner, J. S.: Cellular resolution volumetric in vivo retinal imaging with adaptive optics-optical coherence tomography. pages 4084–4094. Optics Express, 2009.

[132] Hammer, D. X., Ferguson, R. D., Bigelow, C. E., Iftimia, N. V., Ustun, T. E., and Burns, S. A.: Adaptive optics scanning laser ophthalmoscope for stabilized retinal imaging. pages 3354–3367. Optics Express, 2006.

[133] Rha, J., Jonnal, R. S., Thorn, K. E., Qu, J. L., Zhang, Y., and Miller, D. T.: Adaptive optics flood-illumination camera for high speed retinal imaging. pages 4552–4569. Optics Express, 2006.

[134] Zhang, Y., Cense, B., Rha, J., Jonnal, R. S., Gao, W., Zawadzki, R. J., Werner, J. S., Jones, S., Olivier, S., and Miller, D. T.: High-speed volumetric imaging of cone photoreceptors with adaptive optics spectral-domain optical coherence tomography. pages 4380–4394. Optics Express, 2006.

[135] Hofer, H., Chen, L., Yoon, G. Y., Singer, B., Yamauchi, Y., and Williams, D. R.: Improvement in retinal image quality with dynamic correction of the eye's aberrations. pages 631–643. Optics Express, 2001.

[136] Jonnal, R. S., Rha, J., Zhang, Y., Cense, B., Gao, W. H., and Miller, D. T.: In vivo functional imaging of human cone photoreceptors. pages 16141–16160. Optics Express, 2007.

[137] Yaqoob, Z., Wu, J., and Yang, C.: Sdoct: A better oct imaging strategy. Molecular Imaging. ICIP and IEEE, 2009.

[138] Nair, U., Ganekal, S., M.Soman, and Nair, K.: Correlation of spectral domain optical coherence tomography findings in acute central serous chorioretinopathy with visual acuity. pages 1949–1954. Clinical Ophthalmology Dove Medical Press, 2012.

[139] Oster, S., Mojana, F., Brar, ., R.M.S.Yuson, Cheng, L., and Freeman, W.: Idisruption of the photoreceptor isos layer on sdoct is a predictor of poor visual acuity in patients with epiretinal membranes. Journal of Retinal and Vitreous Diseases, 30, 2010.

[140] Syc, S., Saidha, S., Newsome, S. D., Ratchford, J., Levy, M., Ford, E., Crainiceanu, C. M., Durbin, M., andS.A. Meyer, J. O., and andP.A. Calabresi, E. M. F.: Oct segmentation reveals ganglion cell layer pathology after optic neuritis. Brain and A Journal of Neurology, pages 595–610, 2011.

[141] Inoue, M., Morita, S., Watanabe, Y., Kaneko, T., S.Yamane, Kobayashi, S., A.Arakawa, and K.Kadonosono: Isos junction assessed by sdoct in patients with idiopthic epiretinal membrane. American Journal of Ophthalmology, 2010.

[142] Hayashi, H., Yamashiro, K., Tsujikawa, A., Ota, M., Otani, A., and N.Yoshimura: Association between foveal photoreceptor integrity and visual outcome in neovascular amd. American Journal of Ophthalmology, 2009.

[143] Ambati, J. and Fowler, B.: Mechanisms of amd. Neuron, 75, 2012.

[144] andT.M.Aslam andT. MacGillivray andI.J.Deary, N., andR.H.Eikelboom andK. Yogesan, B., and I.J.Constable: Retinal image analysis: Concepts applications and potential. Progress in Retinal and Eye Research, 25, 2006.

[145] C.Agurto, Barriga, S., Murray, V., Murillo, S., Zamora, G., Bauman, W., Pattichis, M., and and, P. S.: Toward comprehensive detection of sight threatening retinal disease using a multi scale am fm methodology. 2011.

[146] Karthikeyan, R. and Alli, R. P.: Retinal image analysis for abnormality detection: an overview. Journal of Computer Science, pages 436–442, 2012.

[147] Jelinek, H. and Cree, M.: Automated segmentation of retinal blood vessels and identification of proliferative diabetic retinopathy. JOSA, 2007.

[148] Osareh, A., Shadgar, B., and Markham, R.: A computational-intelligence-based approach for detection of exudates in diabetic retinopathy images. Transactions on Information Technology in Biomedicine, 2009.

LIST OF PUBLICATIONS RELEVANT TO THIS RESEARCH

1. Mohammad, F., Ansari, R., Wanek, J., Shahidi, M.: Fourier Descriptor Based Level-Set Segmentation for En Face Retinal Images. (Under submission).
2. Mohammad, F., Ansari, R., Wanek, J., Shahidi, M.: Feasibility of Level-set Analysis of En face Retinal in Diabetic Retinopathy. (Under submission)
3. Mohammad, F., Ansari, R., Wanek, J., Shahidi, M.: Frequency-Based Local Content Adaptive Filtering Algorithm For Automated Photoreceptor Cell Density Quantification. (Under submission)
4. Wanek, J. Mohammad, F., Mori, M., Lim, J.I., Zelkha, R., Shahidi, M.: Shack-Hartmann Image Quality and Adaptive Optics Performance in Diabetes, ARVO Fort Lauderdale, Florida. 2009
5. Mohammad, F., Ansari, R., Wanek, J., Shahidi, M.: Photoreceptor cell counting in adaptive optics retinal images using content adaptive filtering, SPIE Medical Imaging Vol 7626, February 2010
6. Mohammad, F., Wanek, J.,Ansari, R., Shahidi, M.: Performance of an adaptive content filtering method for photoreceptor cell counting, ARVO Annual Meeting, Fort Lauderdale, Florida, 2010
7. Mohammad, F., Ansari, R., Wanek, J., Shahidi, M: Frequency-based local content adaptive filtering algorithm for automated photoreceptor cell density quantification, ICIP, IEEE, Orlando Florida, 2012

8. Mohammad, F., Ansari, R., Shahidi, M: Pathology Segmentation in Fluorescein Angiograms of Retinal Disease using a Level Sets Method, SPIE, Medical Imaging, Volume 8676, 2013

VITA

NAME: Fatimah Mohammad

EDUCATION:
PhD., Electrical and Computer Engineering, University of Illinois at Chicago, August 2013
M.S., Computer Science, International Islamic University, Islamabad, Pakistan, May 2006
B.S., Computer Science, International Islamic University, Islamabad, Pakistan, May 2004

EXPERIENCE:
Research Assistant , Dept of Ophthalmology, UIC, May 2008-May 2012

WORKSHOPS AND CONFERENCES:
ICIP Conference, Orlando Florida, October 2012
SPIE Medical Imaging Conference, San Diego, February 2010
ARVO Annual Meeting, Florida, 2010
International Conference on Electrical Engineering IEEE, Lahore Pakistan 2007
MATLAB workshop, Fatima Jinnah University, Islamabad Pakistan, 2007
Image processing workshop, SZABIST University, Pakistan, 2005

MEMBERSHIPS:
Member of Golden Key International Honor Society UIC Chapter since 2008
IEEE Student member

PUBLICATIONS:

1. Wanek, J. Mohammad, F., Mori, M., Lim, J.I., Zelkha, R., Shahidi, M.: Shack-Hartmann Image Quality and Adaptive Optics Performance in Diabetes, ARVO Fort Lauderdale, Florida. 2009
2. Mohammad, F., Ansari, R., Wanek, J., Shahidi, M.: Photoreceptor cell counting in adaptive optics retinal images using content adaptive filtering, SPIE Medical Imaging Vol 7626, February 2010
3. Mohammad, F., Wanek, J.,Ansari, R., Shahidi, M.: Performance of an adaptive content filtering method for photoreceptor cell counting, ARVO Annual Meeting, Fort Lauderdale, Florida, 2010
4. Mohammad, F., Ansari, R., Wanek, J., Shahidi, M: Frequency-based local content adaptive filtering algorithm for automated photoreceptor cell density quantification, ICIP, IEEE, Orlando Florida, 2012

5. Mohammad, F., Ansari, R., Shahidi, M: Pathology Segmentation in Fluorescein Angiograms of Retinal Disease using a Level Sets Method, SPIE, Medical Imaging, Volume 8676, 2013
6. Mohammad, F., Husain, S.A.,: Zone Based Hand Gesture Recognition System, CIITSE, Turkey, 2007
7. Mohammad, F., Husain, S.A.,:Character Recognition Using Mathematical Morphology, ICEE, IEEE, Pakistan, 2007
8. Mohammad, F., Munir, A.,:Image Compression via Dithering for Enhanced Images, ICEE, IEEE, Pakistan, 2007